STRUCTURE AND ELECTRICAL PROPERTIES OF ELECTRON-BEAM EVAPORATED ZIRCONIA THIN FILMS

A Dissertation

Presented to

The Faculty of the Division of Graduate Studies

BY

Paul Ben Onaji

In Partial Fulfillment

of the Requirements for the Degree of

Doctor of Philosophy

in the School of Ceramic Engineering

Georgia Institute of Technology

September, 1982

STRUCTURE AND ELECTRICAL PROPERTIES

OF ZIRCONIA THIN FILMS

Approved:

J. K. Cochran, Chairman

J. L. Pentecost

D. N. Hill

Date Approved by Chairman 8-30-82

ACKNOWLEDGMENT

First, I wish to express my deep gratitude to my advisor, Dr. J. K. Cochran, who continuously provided advice and guidance througout the tenure of this work.

Thanks are due to Dr. J. L. Pentecost and Dr. D. N. Hill, members of my reading committee, for reading the manuscript of this thesis and giving helpful suggestions for improving it. The efforts of Dr. J. F. Benzel and Dr. R. F. Feeney in reading the thesis and participating in my defense committee are also appreciated.

Thomas Mackrovitch will be remembered, not only for constructing several of the equipment, for which he was always prompt and enthusiastic, but also for his kindness and friendliness.

I wish to thank James Cagle of the Engineering Experiment Station for producing the pole figures of some of the films.

Finally, I am grateful to my wife, Idenyi, and my daughter, Ada, whose continuous love, understanding, and cooperation were vital to the success of this work. Thanks are also due to my parents for their continued support and encouragement throughout the years.

I would like to thank all faculty and staff at the School of Ceramic Engineering for their help in various ways throughout the course of this work. My family and I appreciate the help given by Dr. J. L. Pentecost during our initial settlement in Atlanta and the memories of "Thanksgiving Days" at the Benzels' is still fresh in our minds.

TABLE OF CONTENTS

ACKNOWLEDGEMENT iii

LIST OF TABLES vi

LIST OF ILLUSTRATIONS vii

SUMMARY xi

Chapter

I. INTRODUCTION 1

II. SURVEY OF THE LITERATURE 4

2.1 Thin Film Deposition Methods
2.1.1 Vacuum Evaporation
2.1.2 Electron-Beam Evaporation
2.2 Electrical Properties
2.2.1 Ac Conduction
2.2.1.1 Definitions
2.2.1.2 Measurement of Permittivities
2.2.1.3 Polarization
2.2.1.4 Impedance Spectroscopy
2.2.2 Dc Conduction
2.2.2.1 Field Assisted Thermal Emission
2.2.2.2 Ohmic Conduction Processes
2.2.3 Conduction in ZrO_2 Thin Films
2.2.3.1 Ac Conduction
2.2.3.2 Dc Conduction
2.2.3.3 Effects of Electrodes and Flaws
2.2.3.4 Experimental Ac and Dc Values

III. EXPERIMENTAL PROCEDURE 65

3.1 Evaporant Preparation
3.1.1 Slip Cast Evaporant
3.1.2 Dry Pressing
3.1.3 Skull Melting
3.2 Thin Film Deposition
3.2.1 Thin Film Deposition Facility
3.2.2 Thin Film Deposition Procedure
3.2.2.1 Deposition of Mo-ZrO_2-Mo
3.2.2.2 Preparation of YSZ Films
3.3 Crystal and Physical Structure
3.4 Measurement of Electrical Properties
3.4.1 Vacuum System for Electrical Measurements
3.4.2 Ac Measurements

3.4.3 Dc Measurements
3.4.4 Impedance Spectroscopy

IV. RESULTS AND DISCUSSION 90

4.1 ZrO_2 Films
4.1.1 Crystal and Physical Characteristics
4.1.2 Ac Properties
4.1.3 Dc Properties
4.1.3.1 Temperature Dependence
4.1.3.2 I-V Characteristics
4.1.3.3 Change Storage
4.1.4 Impedance Spectroscopy
4.2 Y_2O_3- ZrO_2 Film
4.2.1 Crystal Structure
4.2.2 Dc Conduction
4.2.3 Impedence Spectroscopy

V. CONCLUSIONS 148

VI. RECOMMENDATIONS 152

Appendix

A. SYMBOLIC NOMENCLATURE AND PHYSICAL CONSTANTS 154

B. THIN FILM DEPOSITION PROGRAM 159

C. FORTRAN PROGRAM ACPROP 160

D. FORTRAN PROGRAM DC4 168

E. FORTRAN PROGRAM ADMIT 172

BIBLIOGRAPHY 173

VITA 178

LIST OF TABLES

Table	TITLE	Page
1.	Bridge Detectors and Their Frequency Ranges	29
2.	Experimental Values for Ac Conduction in ZrO_2 Films	63
3.	Experimental Values for Dc Conduction in ZrO_2 Films	64
4.	Thin Film Deposition Conditions	77
5.	Values of x for ε' and $\varepsilon'' \propto f^x$ Relation for Evaporated ZrO_2 Films Deposited at Varying Temperatures	109
6.	Dc Conduction Activation Energy for Evaporated Mo-ZrO_2 - Mo Samples Deposited at Varying Temperatures	123
A-1	Physical Constants	154
A-2	Symbolic Nomenclature	155
B-1	Thin Film Deposition Programs	159

LIST OF ILLUSTRATIONS

Figure	Title	Page
1.	Schematic Diagram Showing the Ecaporation Process	11
2.	Dependence of Grain Size on Deposition Temperature	14
3.	A Typical Example of (a) Work-Accelerated E-Gun (Pendant Drop), (b) Self-Accelerated (Electrostatically Focussed) Gun and (c) Bent-Electron Gun with Water Cooled Evaporant	16
4.	A Schematic of a Vacuum Capacitor	18
5.	The Parallel Model of a Real Dielectric	19
6.	Current and Voltage of a Real Dielctric	21
7.	*Frequency Ranges of Dielectric Measurement Techniques*	24
8.	Stray Capacitances of an Unshielded Two-Terminal Capacitor . .	26
9.	Examples of a Two-Terminal Capacitor	28
10.	Frequency Dependance of the Several Contributions to Polarization (Schematic)	32
11.	Cole-Cole Plot for (a) Single, (b) Spread of Relaxation Times .	33
12.	Loss vs Frequency Showing the Effect of the Various Ac Conduction Processes	35
13.	Admittance Plots for Some Simple R-C Circuits	36
14.	Schematic Admittance Plots (a), and the Equivalent Circuit (b)	38
15.	Diagram of the Various Conduction Processes in a Thin Film Dielectric at High Fields	41
16.	Schematic Representation of Energy Levels of Oxygen Vacancies in ZrO_2	42
17.	One Carrier SCLC-Voltage Characteristics for an Insulator with a Single Trap Level	48

Figure		Page
18.	Energy Band Diagram Showing Electron Hop	49
19.	Ionic Conduction by Oxygen Ions in an Electrolyte	50
20.	Arrhenius Plot of Conductivity of a Typical Insulator (Schematic)	52
21.	Thin Film Deposition Facility	68
22.	Photograph of the Substrate Holder Assembly Prior to Deposition, Showing: (a) the substrate, (b) the Mask Plate, (c) the Thermocouple, (d) the Heater Block	70
23.	Schematic Diagram of E-Beam Evaporation System	71
24.	Thin Film Samples (a) Photograph (b) Sketch Showing the Designation of Individual Capacitors	76
25.	Sketch of Oxide Layers in Multilayer Deposition, Showing Thickness in Å	78
26.	Photograph of the Electrical Test Apparatus Showing (a) Spring Loaded Top-Electrode Probe, (b) Copper Furnace, (c) Bottom Electrode	82
27.	Copper Furnace for Electrical Measurements (Schematic)	83
28.	Circuit for Dc Measurements	85
29.	Circuit for Admittance Measurements (a) for High Impedance (b) for Low Impedance	88
30.	X-ray Diffraction Patterns in the {111} Region for Evaporated ZrO_2 Thin Film, Deposited at (a) 200°C, (b) 450°C, (c) 600°C. Also Shown is the Pattern for Powder ZrO_2 Source Material (d)	91
31.	X-ray Pattern in the {400} Region for ZrO_2 Films Deposited at Varying Temperatures	93
32.	Ratio of X-ray Intensities of Evaporated ZrO_2 Thin Film Sample to the ZrO_2 powder intensities for the $(11\bar{1})$ and (111) Reflections, as a Function of the Deposition Temperature	94
33.	$(11\bar{1})$ Pole Figure for ZrO_2 Thin Film, Sample Z4, Deposited at 420°C, Showing a $(11\bar{1})$ Fiber Axis	96
34.	$(11\bar{1})$ Pole Figure of ZrO_2 Thin Film, Sample Z16, Deposited at 510°C Showing a $(11\bar{1})$ Fiber Axis	97

Figure Page

35. Crystallite Size of Evaporated ZrO_2 Thin Films for the $(11\bar{1})$ and (111) Orientations as a Function of Deposition Temperature 98

36. Scanning Electron Micrograph of the Fracture Surgace of ZrO_2 Thin Film, Sample Z4, Deposited at 420°C 99

37. Imaginary Permittivity of Evaporated Mo-ZrO_2-Mo Sample Deposited at 450°C as a Function of Temperature and Frequency for Two Successive Days 101

38. Imaginary Permittivity of Evaporated Mo-ZrO_2-Mo Sample Deposited at 350°C, as a Function of Temperature and Frequency for Three Successive Days 102

39. Real Permittivity of Evaporated Mo-ZrO_2-Mo Sample, Deposited at 450°C as a Function of Temperature and Frequency 105

40. Imaginary Permittivity of Evaporated Mo-ZrO_2-Mo Samples, Deposited at Varying Temperatures, as a Function of Reciprocal Temperature 107

41. Real and Imaginary Dielectric Constants of Evaporated Mo-ZrO_2-o Sample, Deposited at 450°C, as a Function of Frequency at 25°C and 325°C 108

42. Dielectric Conductivity of Evaporated Mo-ZrO_2-Mo Sample, Deposited at 450°C as a Function of Frequency at 25°C and 325°C . 111

43. Activation Energy and Y Values for Evaporated Mo-ZrO_2-Mo Samples as a Function of Deposition Temperatures for the Different Dispersion Regions 112

44. Product σ_d*T for Evaporated Mo-ZrO_2-Mo Sample, Deposited at 450°C as a Function of Reciprocal Temperature 114

45. Dielectric Conductivity of Evaporated Mo-ZrO_2-Mo Sample Deposited at 450°C as a Function of Reciprocal Temperature . . . 115

46. Dielectric Conductivity of Zirconia Thin Films Prepared By Various Methods as a Function of Reciprocal Temperature. The Conductivity Values of Dawson et. al. were Measured at 1592 Hz; All Others were Measured at 1000 Hz. E-B = Electron-Beam, Sp = Sputtered, and CSZ = Calcia-Stabilized-Zirconia 116

47. Cole-Cole Plot for Evaporated Mo-ZrO_2-Mo Sample, Deposited at 450°C 120

48. Dc Conductivity of Evaporated Mo-ZrO_2-Mo Sample, Deposited at 450°C, as a Function of Reciprocal Temperature for 25 and 50 V and Positive and Negative Polarities 122

Figure Page

49. Dc Conductivity, Dot Positive at 50V, of Evaporated Mo-ZrO_2-Mo Samples, Deposited at 300°C (Z14), 450°C (Z15) and 480°C (Z8) as a Function of Reciprocal Temperature 124

50. Room Temperature I-V Characteristics for Evaporated Mo-ZrO_2-Mo Sample, Deposited at 450°C (Z15) and 300°C (Z14) 128

51. Charge Storage for Evaporated $MoZrO_2$-Mo Sample, Deposited at 450°C as a Function of Voltage for Three Temperatures and Positive and Negative Polarities 131

52. Charge Storage for Evaporated Mo-ZrO_2-Mo Sample, Deposited at 300°C as a Function of Voltage for Three Temperatures, and Positive and Negative Polarities 132

53. Admittance Plots for Evaporated Mo-ZrO_2-Mo Sample, Deposited at 450°C for Varying Temperatures 134

54. Admittance Plots for Evaporated Mo-ZrO_2-Mo Sample, Deposited at 300°C for Varying Temperatures 135

55. Component Capacitor - Resistor Effects of the Admittance Plot of Mo-ZrO_2-Mo Sample, Vapor Deposited at 300°C (Schematic) . . 136

56. XRD Patterns in the {111} Region for Y_2O_3-ZrO_2 Multilayer Film with Pt/Rh Electrodes (a) as Deposited, (b) Aged at 1200°C . . 138

57. XRD Patterns in the {400} Region for Y_2O_3-ZrO_2 Multilayer Film (a) with Pt/Rh Electrodes, Aged at 1200°C, and with Mo Electrodes (b) as Deposited, (c) Aged at 1200°C 139

58. XRD Patterns in the {111} Region for Y_2O_3-ZrO_2 Multilayer Film with Mo Electrodes (a) as Deposited, (b) Aged at 1200°C 141

59. Dc Conductivity of Au/Pd-Y_2O_3, ZrO_2-Pt/Rh Films as a Function of Reciprocal Temperature 143

60. I-V Characteristics of Au/Pd-Y_2O_3, ZrO_2-Pt/Rh Films at Room Temperature 144

61. Admittance Plots for Pt/Rh=Y_2O_3, ZrO_2-Pt/Rh Film, as Deposited for Varying Temperatures 146

62. Admittance Plots for Au/Pd-Y_2O_3, ZrO_2-Pt/Rh Film for Varying Temperatures 147

SUMMARY

In the past 25 years, there has been much interest in dielectric films of $Zr0_2$ for several applications such as an alternative insulator material in microelectronics, resistance switching and an oxygen anion conductor. Only recently have thin film anion conductors, especially the cubic $Zr0_2$ form, been investigated. However, these films will probably find future uses such as solid electrolytes for thermodynamic and kinetic purposes, for purification and preparation of gases, and in oxygen monitoring suysterns.

Zirconia films have been prepared by a variety of methods but electron-beam (E-beam) evaporation has had limited characterization. The objective of this investigation was to study the structure and electrical properties of E-beam evaporated Mo-$Zr0_2$-Ho capacitors as a function of deposition temperature. In addition, Y_2O_3 stabilized $Zr0_2$ films were prepared by a new method, E-beam multilayer deposition, and characterized in terms of structure and electrical properties.

Zirconia films deposited on molybdenum electrodes were polycrystalline. The raonoclinic phase was the major phase detected in the films deposited at temperatures between 300°C and 600°C. At lower deposition temperatures (190^o -200^o C), however, the cubic phase was the major crystalline phase formed. The average crystallite size increased from 118 A to 484 A for the (111) and 175 A to 265 A for the (111) crystallites as deposition temperature increased from 200°C to 600°C.

Ac conduction in Mo-$Zr0_2$-Ho structures at fields < 0.05 MV/cm

was dominated by electron hop with a frequency independent loss behavior between 25°C and 150°C. Between 150°C and 325°C, a o_d « f^{Y} dependence was observed where y depended on measurement and deposition temperatures. The remanance of interfacial polarization is suggested as an additional mechanism in this temperature range and for frequencies of 60-10^5 Hz. The admittance plots of the samples showed a single semicircle with a small semicircle depression that was ascribed to bulk conduction.

Both ohmic and space-charge-limited-currents (SCLC) dc conduction were obtained for the Mo-$Zr0_2$-Ho samples. The charge storage in these films increased linearly with voltage and depended on measurement and deposition temperatures, but was probably polarity independent.

$Y2O_3$ stabilized $Zr0_2$ films could be formed by multilayer deposition followed by heat treatment at 1200°C for at least seven hours. Heat treated Au/Pd-Y_20_3,$Zr0_2$ Pt/Rd capacitors exhibited a SCLC behavior at a field of 0.03 MV/cm and room temperature. The admittance plot of this sample had a large semicircle depression of about 45°.

CHAPTER I

INTRODUCTION

Zirconia (ZrO_2) is a highly refractory oxide, melting at 2700° C, which occurs in three crystalline forms: monoclinc, tetragonal and cubic. The monoclinic structure is stable below 1000°C but the transformation to tetragonal above 1000°C has a destructive volume contraction which has inhibited the use of pure ZrO_2 for high temperature applications. In the pure state, the cubic ZrO_2 form is obtained only at temperatures above 2300°C. However, it can be produced at lower temperatures by the addition of small amounts of CaO, Y_2O_3 or other suitable divalent or trivalent oxides of cubic symmetry such as the rare earth oxides, Sc_2O_3, Yb_2O_3, and Gd_2O_3. The cubic ZrO_2 produced in this way is referred to as stabilized ZrO_2 because it is stable at normal temperatures and does not undergo any transformation until its melting point.

Despite the relatively recent discovery of ZrO_2 in the mineral Baddeleyite in 1892, ZrO_2 now finds wide application because of its varied desirable properties. Because of its extreme inertness and refractoriness, it is applied as a refractory, especially in glass tanks. Transformation toughened ZrO_2 has a high fracture toughness and abrasion resistance and so is used, for example, as extrusion dies. The cubic oxide is used for gem stones, opacifiers in glazes due to a high refractive index and as heating elements because of semiconductive

electrical properties at elevated temperatures.

Furthermore, ZrO_2 finds an important use as an oxygen-ion conducting solid electrolyte because of a near unity oxygen-ion transference number at high temperatures. ZrO_2 solid electrolytes have been used in the construction of galvanic cells for measuring thermodynamic and kinetic properties of oxygen-bearing systems with high accuracies. This has resulted in oxygen sensors for gas mixtures such as flue gases and automobile air-fuel mixtures, liquid metals such as molten steel, and in high temperature fuel cells. In solid electrolyte applications, the ZrO_2 has been applied in bulk form requiring tedious methods [1] to prepare the electrolytes and high temperatures to realise the desired high conductivities ($>10^{-2}$mhos/cm) with the attendant difficulties of dealing with such high temperatures. However, if the ZrO_2 could be applied as thin films, the films would have much higher conduction at similar temperatures, enabling their use at reduced operating temperatures. Such films could be easily fabricated by the well established thin film technology. This is one reason for interest in ZrO_2 films, especially the cubic form, in recent times. Interest in ZrO_2 films also arises from their possible use as insulators. In microelectronics, insulator films are used for passivation and as insulators with Al_2O_3 and SiO_2 films being the most widely used. However, for certain applications, the extreme refractoriness, inertness, and crystallinity of ZrO_2 may be an advantage. Interest has also been shown in the switching behavior of ZrO_2 films.

These and other interests in the electrical applications of ZrO_2 thin films have resulted in an extensive published work on the

electrical properties of the films. Anodized [2-6] and oxidized [7,8] films are the most widely studied. However, in recent times, sputtering [9,10], chemical vapor deposition (CVD) [11,12], and electron-beam (E-beam) evaporation [13-15] are receiving much interest. Even the cubic stabilized ZrO_2 form has been prepared by sputtering [9,10], co-evaporation with the electron gun [16] and by ion-beam implantation of E-beam evaporated ZrO_2 films [15].

As attractive as the E-beam method is for the deposition of high melting oxides or mixtures of oxides on a relatively cool substrate, the reproducibility and stability of the electrical properties of the oxides so prepared were reported by Chan et al [2] as poor and probably discouraged much interest in the method. However, the availability of a rate controlled E-beam evaporator and the wide potential of ZrO_2 for electronic applications, provided the motivation for reinvestigating ZrO_2 films. The objective of this investigation was to study the electrical and sructural properties of E-beam evaporated Mo-ZrO_2-Mo capacitors as a function of deposition temperature. The final measurements of electrical properties were made after conditions for their reproducibility and stability had been established. Attempts were made to deduce conduction mechanisms and to obtain the optimal conditions for the preparation of such films. In addition, Y_2O_3 stabilized ZrO_2 (YSZ) films were prepared by a new method, E-beam multilayer deposition, and some of the structural and electrical properties of these stabilized films were characterized.

CHAPTER II

SURVEY OF LITERATURE

Below is a discussion of the background materials needed for comprehending subsequent chapters and a review of the published experimental results. The background material discussed includes thin film deposition methods (with emphasis on the evaporation method) and thin film electrical properties, both ac and dc, in insulators in general. Finally, published experimental results on ZrO_2 thin films are presented.

2.1 Thin Film Deposition Methods

The deposition of thin films of metals, alloys or compounds is a well established technololgy. The films produced are of wide application, including coatings for mirrors and optical lenses, corrosion-barriers, wear-resistant layers, antireflection coatings for solar cells, and on microelectronics. The latter is by far the most important area of application of these films. Here, metal films serve as conductors and resistors and dielectrics find diverse uses such as insulating films, capacitive dielectric layers and passivating layers. The intense interest and activity in this technology has produced several methods for the deposition of the films. The choice of the deposition method for a given application is determined by the properties of the film desired, the cost of, or production rate

available from the process, temperature limitations of the substrate, and uniformity or consistency of the process and/or its compatibility with preceeding and subsequent processing steps. In this section, methods used for producing dielectric films alone or dielectric and metal films are presented with the main focus being on evaporation, especially E-beam evaporation.

However, before discussing evaporation, other deposition processes will be summarized. Amick [17] provided a review of the methods for depositing thin dielectric films on semiconductor devices, including a comparison of the alternatives in terms of source materials, deposition rates, nature of deposits, sources of impurities, types of films formed and typical electronic applications. The most common deposition methods may be divided into two main groups:

1. Atmospheric pressure techniques
    1. Thermal oxidation and steam corrosion
    2. Anodization
    3. Chemical vapor deposition (CVD)
2. Low pressure techniques
    1. Evaporation
    2. Sputtering
    3. Plasma deposition
    4. Plasma (ionized gas) oxidation or anodization
    5. Low pressure CVD

Sputtering and evaporation are physical vapor deposition (PVD) methods whereas all the other methods are chemical methods which are discussed in some detail by Campbell [18].

Thermal oxidation and steam corrosion are some of the oldest techniques, involving the exposure of a metal to environments containing oxygen (thermal oxidation) or water (steam corrosion) at moderate to high temperatures. A typical example is the formation of SiO_2 on Si wafers. The most common use of such SiO_2 is as channel dielectrics in metal oxide-semmiconductor (MOS) devices. These techniques provide very high quality pin-hole free oxide layers on Si [17].

Anodization is an electrolytic process whereby bulk metal or evaporated thin metal films form the anode of an electrolytic cell. The electrolyte used depends on the type of metal to be anodized. The oxide film at the anode grows by the migration of oxygen ions of the electrolyte through the oxide film to the oxide-metal interface where the reaction occurs, or the migration of the metal ions in the opposite direction, with the reaction occuring at the outer surface of the oxide film. The thickness of the oxide film formed depends on the applied voltage. Two uses of this method are the manufacture of electrolytic capacitors and providing protective coatings on aluminum metallization in silicon devices.

Chemical vapor deposition is the most versatile and widely used technique for forming dielectric films on silicon devices. In this process, a gas mixture containing the desired source elements is passed over a heated substrate surface where chemical reactions take place heterogeneously. Homogeneous nucleation and growth in the gas phase is minimized by the temperature and flow conditions chosen for the particular reaction. Most kinds of dielectric films can be prepared by this method, including transparent conductive layers such as tin oxide.

The method is flexible, rapid (1000 Å/min or more) and film uniformity and reproducibility are good, but the substrates have to be heated to permit the desired reactions. Film quality is poor compared to thermal films.

In sputtering, atoms or molecules are physically ejected from the surface of a target material by the bombardment of ions, usually of an inert gas such as Ar. The ejected material coats the surface of the substrate. In the simplest case, cathode sputtering, the bombarding ions are produced in a glow discharge between a cathode and an anode where the cathode is the target and the substrate is placed on the anode. The glow discharge may be self sustained (cold cathode used) or may be supported by thermionic emission of electrons from a hot cathode. In sputtering in general, the target may be different from the cathode and various kinds of biasing may be used. Variations of the basic method described above, are common. For example, in the so called ion beam deposition method, bombarding ions are produced elswhere in an ion gun and diffused into the sputtering chamber, where they are accelerated towards the target surface. If dc power is applied to the electodes, dc sputtering ocurrs and the cathode must be a conductor. However, dielectrics may be prepared by reactive dc sputtering in which a gas phase is introduced to react with a metal film as it is deposited. dc sputtering cannot be used to produce dielectric films directly because, if a dielectric is used as the target, the cations arriving at the surface accumulate, producing a space charge which stops the arrival of more sputtering cations. The solution to this charge up problem was provided by rf sputtering, where radio frequency (rf) power is used

instead of dc power. A charge in one half cycle of the rf signal is neutralized by the opposite polarity of the next half cycle, allowing a steady discharge to be maintained.

The sputtering method is widely applied with a good description of the applications given by Maissel [19]. Its advantages over other methods includes the ability to coat non flat surfaces such as tubes and rods, the deposition of multicomponent films such as alloys and compounds, good adhesion and uniform thickness of the films. There are also disadvantages, however, such as contamination of the films, difficulty in controlling the large number of process parameters, requirements for source materials to be available in certain forms such as sheets and rods, the necessity of cooling the substrates, and low deposition rates attainable (2000 Å/min).

Plasma deposition involves an electrical discharge through the vapor of a volatile source material at low pressure. The same kinds of vapor sources are employed as for CVD (eg. SiH_4), but the decomposition to form the films is principally by the action of the glow discharge, assisted in some cases by substrate heating. The glow discharge is maintained by rf power.

Plasma anodization is similar to the basic anodization process except that the electrolyte is an oxygen plasma (ionized gas) rather than a liquid electrolyte. A metal or semiconductor sample fixed to a sample holder is placed in the negative glow of an oxygen plasma, and positive bias with respect to the anode is applied. Oxide films of high purity at relatively low temperatures, in some cases even below 100 °C can be obtained by this method. Jarzebski [20] gives a description of

the process.

2.1.1 Vacuum Evaporation

The deposition of thin metal films in a vacuum by Joule heating of platinum wires was discovered by Nahrwold [21] in 1887 but the commercial exploitation of this process was delayed by development of vacuum equipment. During the last 37 years, vacuum evaporation has found wide commercial application and, besides Joule heating, other methods of heating the evaporant such as rf heating, electron, and laser beam heating have been used. Campbell [22] showed that evaporation is of the widest applicability in comparison to the other thin film deposition methods used in microelectonics. Evaporation is widely used for preparing conductors, resistors, insulators, capacitors and superconductors and can be used for preparing active devices and magnetic materials. In comparison, the CVD method that is second in applicability is widely used for preparing only active devices. One of the attractive features of evaporation is the high rates obtainable (1-1000 Å/sec). These rates are comparable with that of CVD but the maximum is two orders of magnitude greater than attainable in sputtering. Also attractive, is the fact that the substrate can be at a relatively low temperature. The E-beam evaporation method presents additional advantages: It is suited for deposition of refractory metals and dielectrics because high temperatures can be obtained with electron beams, and the evaporant is self-containing during the melting. This eliminates the serious problem of reaction, alloying or contamination of the evaporant and its support, the vapor source. The evaporation method is discussed by Glang [23], who covers topics such as kinetics and

thermodynamics of the process, the mechanisms of evaporation, construction and uses of vapor sources and the evaporation of compounds, alloys, and mixtures. Therefore, in this section, evaporation will be discussed in a summary form.

The evaporation process is carried out in a vacuum of usually less than 10^{-5} torr. At such low pressures, the mean free path of atoms or molecules (vapor species) evaporating from the evaporant is usually larger than the distance between the walls of the vacuum chamber and so the particles form a vapor beam of a certain solid angle, Figure 1. If a substrate, which is usually heated, is placed perpendicular to the beam at a distance from the source, the vapors condense on it to form the thin film. To produce sufficient vapor flux, the evaporant is usually heated to a temperature at which its vapor pressure is between 0.1 and 0.01 torr. The evaporant at these temperatures may be liquid or solid.

The rate of evaporation is given by the Hertz-Knudsen equation:

$$\frac{dN_e}{A_e dt} = \alpha_v (2\pi m k\ T)^{-\frac{1}{2}} (p^* - p)\ , \qquad (1)$$

where $dN_e/A_e dt$ is the rate of evaporation per unit area, α_v is defined as the ratio of the rate of evaporation in vacuo to the theoretically possible rate, m is the mass of the molecule, k is the Bolzmann constant, T is the absolute temperature, p^* is the equilibrium vapor pressure, and p is the hydrostatic gas pressure on the surface of the evaporant. Therefore, for a given evaporant, the temperature and gas pressure control the evaporation rate. Usually, the pressure is fixed which leaves temperature as the only parameter for controlling the

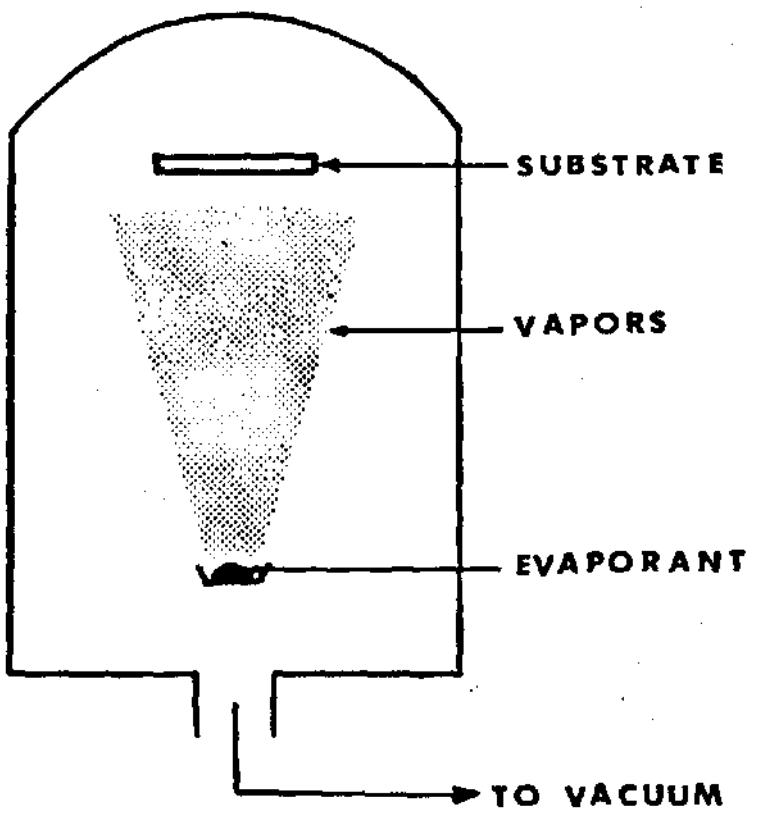


Fig. 1. Schematic Diagram Showing the Evaporation Process.

evaporation rate.

The residual gas pressure, besides affecting the rate of evaporation, can be important for other reasons. For some uses, the residual gases can be a serious source of contamination, reacting with the evaporant or deposit. In other applications such as reactive evaporation, relatively high levels of residual gases are used to

enhance reaction with the vapors on the substrate. This method is widely used to form dielectric films from metals and for preparing films from compound dielectric sources that have a tendency to decompose. The latter method is used in the preparation of Al_2O_3, SiO_2, ZrO_2 and many oxide films using oxygen as the reactant gas. Nitrides may be prepared with a nitrogen reactant gas etc. The gas pressure during reactive sputtering is usually about 10^{-4} torr, at which pressure the mean free path of the vapor species is about 50 cm; hence the probability of the reactant gas and vapor species colliding to react and form the dielectrics in the gas phase is low. Reaction is limited to the gas and the vapor species adsorbed on the substrate surface and reaction rates are dependent on the vapor evaporation rate and reactant gas partial pressures. The type of substrate and reactant gas vapors as well as the substrate temperatures, all affect the adsorption, desorption, and reaction steps and hence the overall rate of reaction.

The growth of the films on the substrates has been described by Neugebauer [24]. Vapors adsorbed on the substrate surface grow into the continuous films by a sequence of processes which may be summarized as follows: First, the adsorbed monomers grow into nuclei which form clusters. The clusters touch and coalesce into a new island occupying an area smaller than the sum of the original two, thus exposing fresh substrate surface on which monomers can adsorb and produce secondary nucleation. Finally, large islands grow together leaving channels or holes of exposed substrate which are later filled by secondary nucleation to give a continuous film. During the various growth processes, the mobility of the vapor molecules will be important in

determining the final structure obtained. If the mobility is low, films may be highly disordered as growth and coalescence will be inhibited. Such films will be amorphous or highly disordered polycrystalline. On the other hand, relatively high mobilities will enhance crystalline characteristics and order in the films. The mobility of the vapor particles on the substrate depends mainly on the evaporant material and the substrate temperature.

Defects, including grain boundaries, are incorporated in the films during growth. The quantity of defects depends on the surface mobility of the vapor molecules. Low surface mobility leads to small grain sizes in crystalline materials and hence larger grain boundary material. The converse is the case for high surface mobility vapor molecules; larger grains are formed. The grain sizes are found in practice to depend on substrate temperature, film thickness and to a lesser extent on the deposition rate. The dependence is characterized by a saturation of the sizes at some value of the deposition variables [25], Figure 2.

At high surface mobilities, preferred orientations of the crystallites formed relative the film growth direction are possible. Such preferred orientation will arise because certain crystalline orientations are thermodynamically favorable and the molecules have sufficient mobility to move into these preferred orientations.

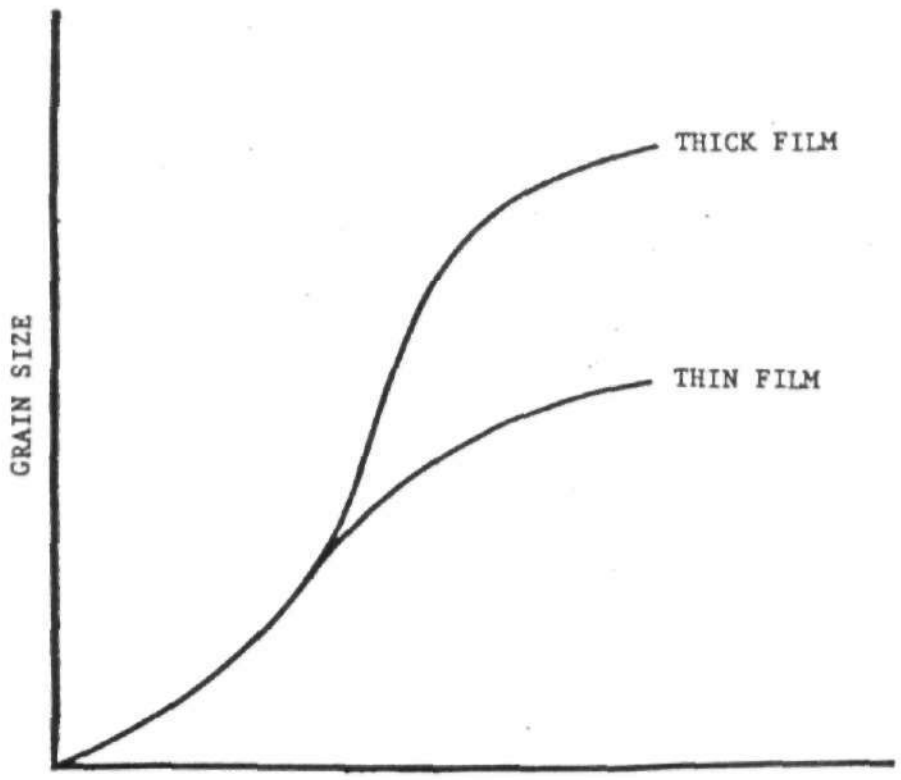


Fig. 2. Dependence of Grain Size On Deposition Temperature.

2.1.2 E-beam Evaporation

It is always preferrable to use Joule heating in evaporation where it is feasible, but the problems of contamination by the source and the difficulty of attaining extremely high temperatures dictates that the E-beam evaporation method be used for the refractory metals and dielectrics. In E-beam evaporation, an electron bombardment device, the electron gun, provides electrons which are accelerated through fields of typically 5-10 KV, toward the evaporant surface. On bombarding the

evaporant surface, most of the kinetic energy of the electrons is converted into heat, which provides the energy required for evaporation. Temeratures of up to 3000 °C can be attained. Of the various types of electron guns, all of them employ a hot tungsten cathode as the electron emitter but differ in the way the electrons are accelerated to the evaporant. They may be classified into three groups: (1) Work accelerated electron guns in which the accelerating voltage is maintained between a wire loop cathode and the evaporant (the work). (2) Self-accelerated electron guns which consist of a small tungsten helix or hair pin filament cathode and an anode between the cathode and the work. The space between the anode and work is field-free. Electrostatic or magnetic focusing may be incorporated in this gun. (3) Bent electron guns are similar to the self-accelerated guns except that the electron beam is bent in the former by magnetic fields so as to remove the restriction in the latter that the source and gun have to be in a straight line with the substrate displaced from this line. Examples of the different kinds of electron guns are in Figure 3.

There are several ways to support the evaporant material during E-beam evaporation but the water cooled copper hearth is usually preferred. Even though the evaporant is in contact with the support, interaction is negligible because a skull of solid evaporant is maintained at the interface which separates the melt from the support. Other suitable support as used for resistance heating evaporation could also be used, except for dielectric evaporants where the support has to be conductive to prevent charging of the evaporant.

By using the electron beam for melting the evaporant, several

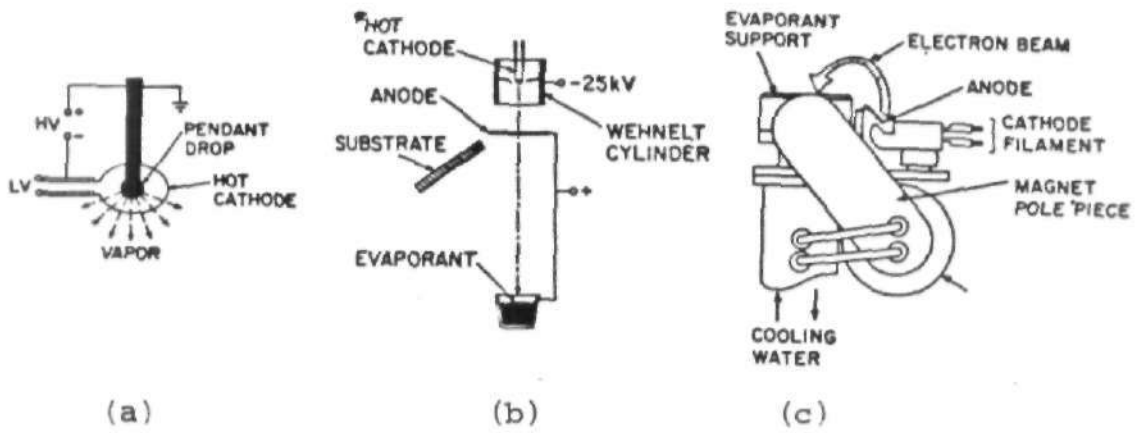


Fig. 3. A Typical Example of (a) Work-Accelerated E-gun (Pendant Drop), (b) Self-Accelerated (Electrostatically Focussed) Gun and (c) Bent-Electron Gun With Water Cooled Evaporant.

effects may occur that are peculiar to the process. Stray electrons from the gun can charge substrates to the full gun potential [26]. Ions of the evaporant can be created by surface ionization at filaments or by passage of the evaporant through an electron beam [27], and these ions can be accelerated towards the substrates at very high energy, resulting in more trapped charge in deposited films as well as non-uniform film thickness due to sputtering [28]. Substrate bias voltages and biased grids in front of substrates have been used to minimize these charge effects.

2.2 Electrical Properties

Electrical characteristics of thin films can be similar to, but very often are different from, that of the bulk material. Such differences can arise for several reasons. For instance, thin films have much larger surface to volume ratios than the bulk material, and so surface phenomena such as adsorption, surface roughness, and flaws can have a more profound effect on the thin films. The application of small voltages to thin films, produces large fields which can introduce conduction mechanisms different from those observed in the bulk material at similar voltages. Films may be so thin that tunnelling processes, which are absent in bulk materials, operate. Consequently, discussion in this section will focus on thin film behavior. Because the conduction in ZrO_2 and other insulating films is generally similar, the background material that is presented on ac and dc properties will be based on general characteristics of insulating films. Finally, a review of published experimental results on the electrical properties of ZrO_2 thin films is presented.

2.2.1 Ac Conduction

In this section, the basic definitions of the ac properties and techniques for measuring permittivities and polarization mechanisms are presented, in that order. Finally, a brief description of impedance spectroscopy is given.

2.2.1.1 Definitions

For two parallel metal plates of surface area A, separated in vacuum by a distance t, as depicted in Figure 4, the capacitance of the unit is given by

$$C_v = \frac{\varepsilon_o A_C}{t} , \qquad (2)$$

where C_v is the vacuum capacitance and ε_o is the permittivity of real space.

Now, if a dielectric is inserted in the space between the metal plates, its capacitance C, is given by

$$C = \varepsilon\varepsilon_o \frac{A}{t} , \qquad (3)$$

hence

$$\varepsilon = \frac{C}{C_v} , \qquad (4)$$

where ε is the dielectric constant of the material. In literature, ε is also referred to as relative permittivity ε_r, but the subscript r is often omitted. The symbol K* is also commonly used for ε but the latter

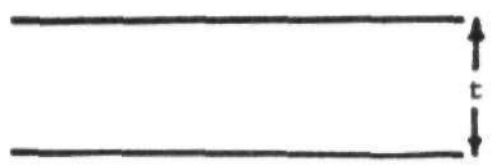


Fig. 4. A Schematic of A Vaucum Capacitor

will be used throughout this thesis.

It is often convenient to assume a physical model of the dielectric behavior. The simplest model is that of an ideal capacitor and a resistor in parallel or series. The following discussion will use only the parallel model but equivalent results for the series model can be found in several books [28,29]. The model is depicted in Figure 5. The impedance Z for this model is given by

$$Z = \frac{Z_C \, Z_R}{Z_C + Z_R} , \tag{5}$$

where, Z_C and Z_R are capacitor and resistor impedances respectively. For a sinusoidal wave,

$$Z_R = R_p , \tag{6}$$

and

$$Z = 1/j\omega \, C_p , \tag{7}$$

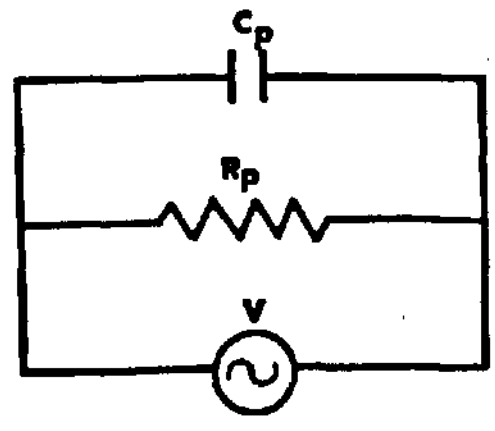


Fig. 5. The Parallel Model of A Real Dielectric.

where C_p and R_p are the parallel model capacitance and resistance respectively. Hence,

$$Z = \frac{R_p}{(j\omega C_p R_p + 1)} \cdot \tag{8}$$

If a sinusoidal voltage V is applied to the dielectric as shown in Figure 4, the current through the sample is given by

$$I = \frac{V}{Z} = V\left(\frac{1}{R_p} + j\omega C_p\right) , \tag{9}$$

or

$$I = \underbrace{V/R}_{I_R} + \underbrace{j\omega C_p V}_{I_C} . \tag{10}$$

I and V are sketched in the complex plane in Figure 6, where I_C and I_R are current through the capacitor and resistor respectively. The power dissipation in the dielectric is characterized by the ratio of I_C to I_R:

$$DF = \frac{|I_R|}{|I_C|} = \tan\delta = \frac{1}{\omega R_p C_p} , \tag{11}$$

where DF is the dissipation factor. Other factors are sometimes used to characterize the loss such as power factor, and quality or Q factor, but these are not considered here.

This parallel model shows that both C and ε in Equation (3) for the real dielectric have to be complex quantities, so that applying a voltage V to the real dielectric of Figure 4 we can obtain a complex

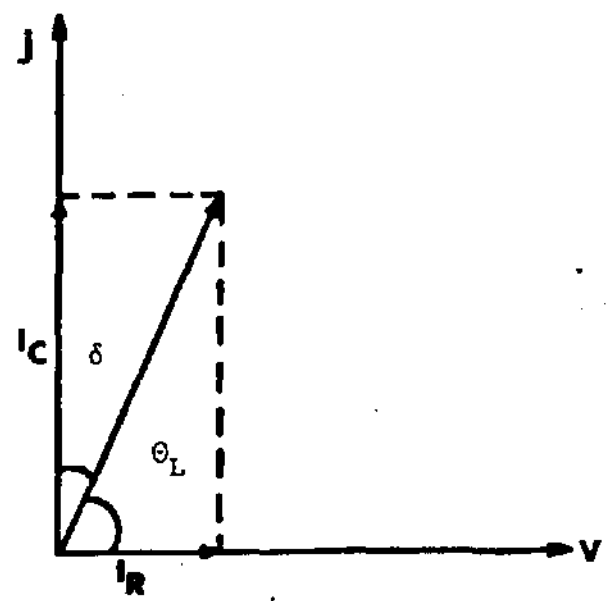


Fig. 6. Current and Voltage of A Real Dielectric.

current, I, through the dielectric as in the parallel model. We may hence define ε as

$$\varepsilon = \varepsilon' - j\varepsilon'' , \tag{12}$$

where ε' and ε'' are the real and imaginary parts of the dielectric constant and so

$$C = C_v(\varepsilon' - j\varepsilon'') = (\varepsilon' - j\varepsilon'')\frac{\varepsilon_o A_C}{\tau} . \tag{13}$$

The current through a real dielectric at voltage V is then given by

$$I = j\omega CV , \tag{14}$$

Subtituting for C from Equation (13) and rearranging, we obtain

$$J = \frac{I}{A_C} = (\omega\epsilon_o\epsilon'' + j\omega\epsilon_o\epsilon')F \ , \qquad (15)$$

where F is the field, V/t. The ac conductivity J/F follows as

$$\frac{J}{F} = \underbrace{\omega\epsilon_o\epsilon''}_{\sigma_d} + \omega\epsilon_o\epsilon' \ . \qquad (16)$$

Dielectric connductiviy, σ_d, is defined as the real part of this conductivity. σ_d is sometimes referred to as ac conductivity, σ_{ac}, but σ_d will be used here. From Equations (13) and (14)

$$I = j\omega(\epsilon' + j\epsilon'')\ C_v V \ , \qquad (17)$$

$$I = [\omega\epsilon'' + j\omega\epsilon']\ C_v V \ . \qquad (18)$$

But for the parallel model, Equation (9) gives

$$I = \left[\frac{1}{R_p} + j\omega C_p\right] V \ . \qquad (19)$$

Comparing Equations (19) and (9),

$$\varepsilon' C_v = C_p, \tag{20}$$

$$\varepsilon' = C_p/C_v, \tag{21}$$

$$1/R_p = \omega\varepsilon'' C_v = \omega C_p \varepsilon''/\varepsilon'. \tag{22}$$

From Equations (11) and (22),

$$\frac{\varepsilon''}{\varepsilon'} = \frac{1}{\omega R_p C_p} = \tan\delta\ . \tag{23}$$

Hence, ε' and ε''can be calculated from the measured C_p and $\tan\delta$.

2.2.1.2 *Measurement of Permittivity*

From the description on the ac properties of dielectrics, it is seen that once the capacitance and loss tangent of a dielectric are determined, they can be used together with the physical dimensions of the material to calculate the other ac properties such as permittivity, dielectric constant and ac and dielectric conductivity. Some of the experimental techniques to be described here use this approach; however, other techniques exist which are based on the direct measurement of permittivity or dielectric constant and loss which can then also be used to calculate the other ac properties. There is vast literature on the various measurement techniques and so the presentation here will be brief and primarily qualitative.

The most suitable method for measuring the permittivity of a material depends on the frequency range to be measured. These methods

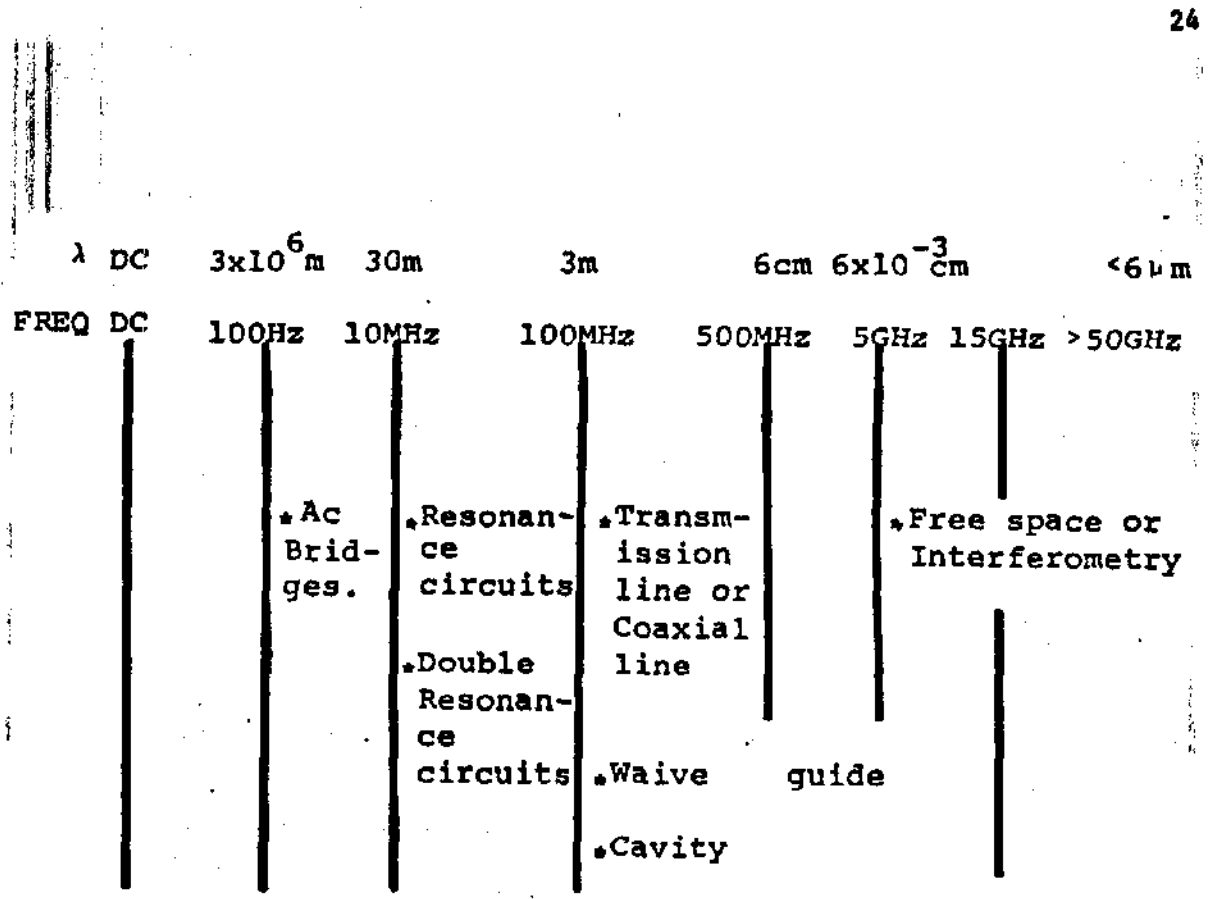


Fig. 7. Frequency Ranges of Dielectric Measurement Techniques.

and their frequency ranges are presented in Figure 7. The dc method of measuring permittivity involves the measurement of the time constant for discharge of a dielectric through a standard resistor with and without the resistor present [30]. In the frequency range from 100 Hz to 10 MHz, several kinds of ac bridges are available for the measurement of capacitance and loss tangent. Resonance methods become more suitable in the frequency range of 10-100 MHz, as bridge methods become difficult due to the increasing importance of the effects of stray capacitance. The single resonance method is suited to low loss materials ($\tan \delta < 0.05$). For higher values of $\tan \delta$, the double resonance method is more applicable. Both methods are described by Anderson [31]. At

very high frequencies (V.H.F.) above 100 MHz, the wavelength of the signal is less than 3 M and has become comparable or smaller than the physical dimensions of the dielectric; hence, distributed circuits must be used. Such methods include transmission-line (coaxial-line), waveguide (for sufficient quantity of material) or cavity (for insufficient quantity of material), and free space (interferometer) techniques. An excellent discussion of these microwave methods has been given by Pentecost [32]. Pentecost also discussed the complicating effects of high temperatures in such measurements. The ac bridge methods are of interest in this work and they are discussed further.

The ac bridge method for measuring capacitance and loss is described in detail by Stout [33]. Also described are several commercial bridges such as the General Radio type 716-C capacitance bridge. Operation of the various bridges is based on the principle of the Wheatstone Bridge, with which the reader is assumed to be familiar. However, the simple Wheatstone impedance bridge would produce huge errors in measurements at high frequencies because of electrical and electromagnetic interference between the various elements of the bridge. In the commercial bridges, these elements are well shielded and the major error is due to lead and measuring cell capacitances. Thus it is important to keep leads short and shielded. The stray capacitances that are produced on measuring the capacitance C_x, of an unshielded two terminal capacitor is illustrated in Figure 8 where the subscript 1 stands for lead and g for ground. The effect of the stray fields may be eliminated by use of micrometer electrode measuring cells described by ASTM [34]. These are however, more applicable to bulk samples. The

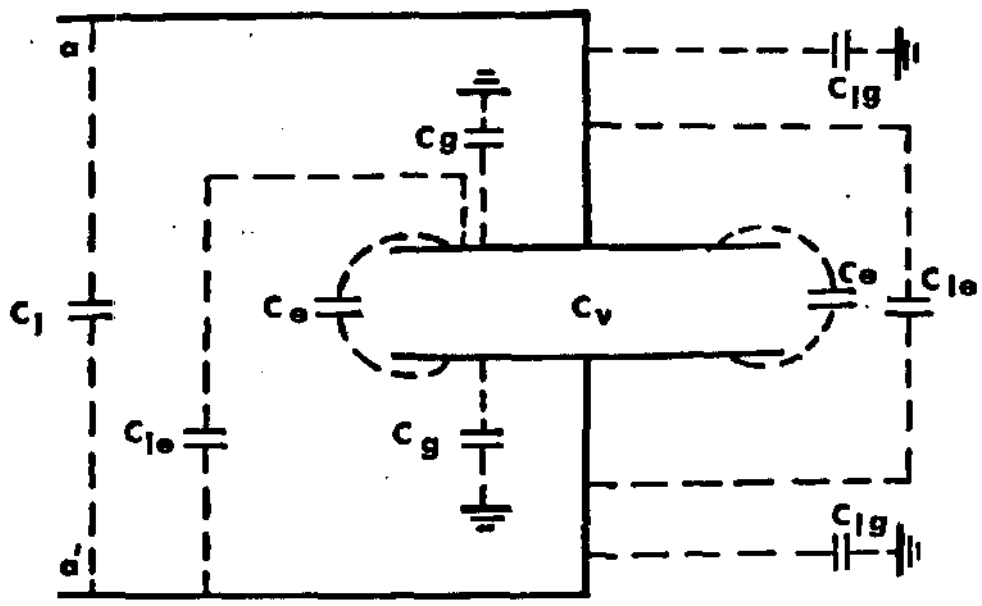


Fig. 8. Stray Capacitances of an Unshielded Two-Terminal Capacitor.

stray capacitances and inductances of leads will be negligible if tney are kept short. Fringing effects that produce the edge capacitance C_e are eliminated by using guard ring, three-terminal electrode systems; but these are usually difficult to construct, especially in thin film applications. Where two-terminal electrodes have to be used, as is often expedient, edge corrections can be made. Correction equations for various kinds of electrode structures are given by ASTM [34]. The only stray capacitances remaining are ground capacitances C_g and C_e , Figure 8. With large capacitors, the ground capacitance may be negligible in comparison. When measuring small capacitances, however, these ground capacitances may be large, even larger than the unknown capacitance to

be measured. The dielectric to be measured is usually placed in a measuring cell which may or may not be grounded. Such a cell acts as a shield and modifies the ground capacitances. This is illustrated in Figure 9 for three types of shielding. The equivalent circuits for the capacitances produced by the different kinds of shields are also shown in the Figure. Note that if the "B" terminal in Figure 9(d) is also grounded, we have a two-terminal capacitor with a total capacitance, C_T, given by

$$C_T = C_{AS} + C_{AB}. \tag{24}$$

Several types of detectors are used with ac bridges to determine the null point but each type is suitable only for a given range of frequencies. The more common ones are listed in Table 1 along with frequency ranges and appropriate comments. Further details on these detectors are given by Stout [33].

2.2.1.3 Polarization

When an electric field is applied to a material, charge separation constituting dipoles may be produced, or dipoles already present in the material may become preferentially oriented in the direction of the field. The polarization of the material is defined as the dipole moment per unit volume. The dielectric constant of a material results directly from this polarization. An excellent description of this relationship can be found in several books [35,36].

On application of an electric field to a material, four types of polarization are produced: electronic, ionic, orientational, and space charge or interfacial polarization. In electronic polarization, the

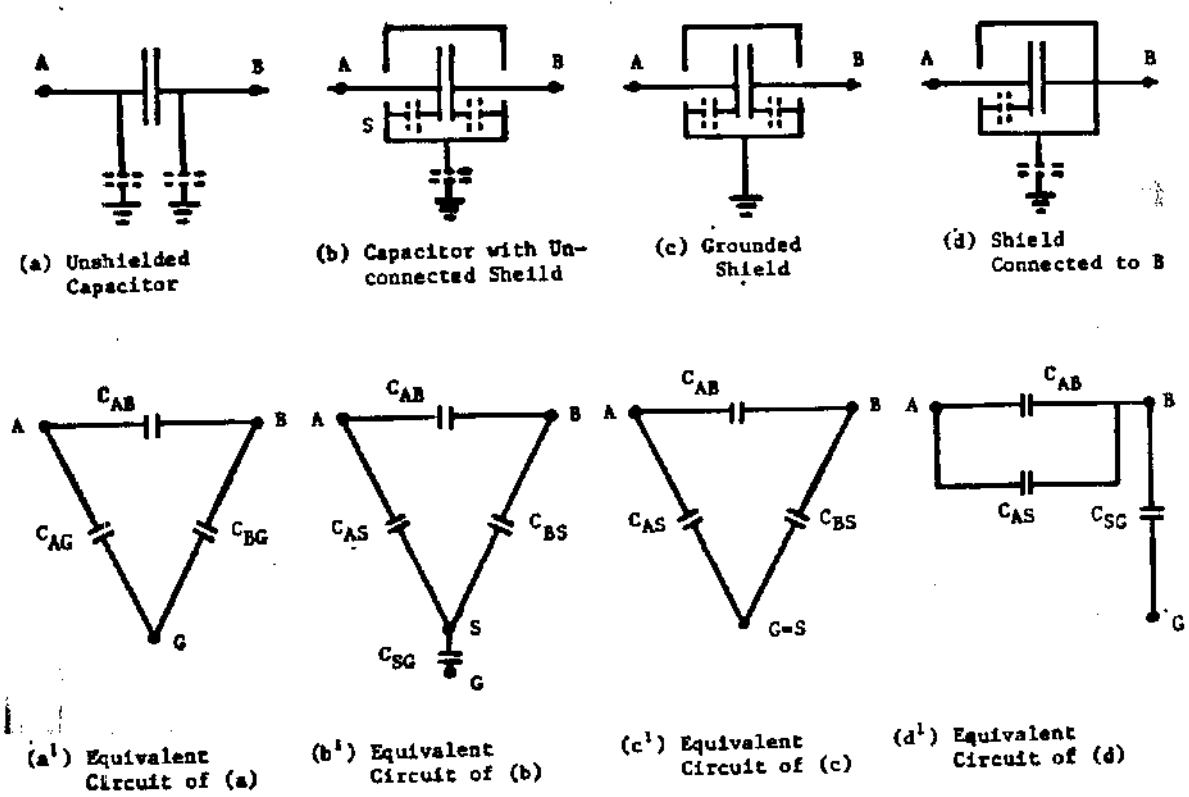


Fig. 9. Examples of A Two-Terminal Capacitor.

Table 1. Bridge Detectors and Their Frequency Ranges

	Detector	Freq. range (Hz)	Comments
a)	Galvanometers		
	vibration galvanometers	25-60	
	excited-field-ac-galv.	25-200	
b)	Telephone receivers	200-4000	Common, sensitive, inexpensive
c)	Lock-in Amplifiers	$1-10^5$	Excellent signal to noise ratio
d)	Amplifiers followed by a	25-4000	For small signals
	galvanometer		
	telephone receiver		
	indicating instrument		
	tuning eye		
	cathode ray o'scope		
e)	Cathode ray o'scope	>25	For small signals
f)	Radio receiving sets	$> 10^4$	Receivers should be well shielded.

electron clouds of atoms become deformed, with electrons pulled preferentially towards the positive electrode and away from the nucleus. This is common to all materials. Ionic or atomic polarization involves the actual displacement of bonded ions or atoms, the cations towards the negative electrode and the anions toward the positive electrode. Where dipoles already exist, the originally randomly oriented dipoles will orient preferentially in the direction of the electric field in orientation polarization. In space charge polarization, the charge carriers accumulate at boundaries of two differentially conducting regions as they move through the material. Such boundaries could be between grains, between the bulk material and the electrode, between the bulk material and grain boundaries, or the carriers may be trapped and depleted by trapping levels to produce a space charge. A few solids, ferroelectric solids such as $BaTiO_3$ and $CaTiO_3$, have a spontaneous polarization. In these solids, the crystal structure is such that the unit cells are inherently polarized. The strong local electric field of the individual dipoles mutually interact to align the dipoles in a small region (a domain) in one direction, resulting in spontaneous polarization. The solid then consists of electric domains which are randomly oriented at high temperatures but can be preferrentially oriented by an electric field below the Curie temperature to produce polarization. The polarization is characterized by a polarization vs. field (P-F) hysteresis loop. A linear P-F plot is obtained if the material is not ferroelectric. A dielectric constant above 12 at frequencies $> 10^9$ Hz is indicative of a ferroelectric contribution. The total polarization in a material, P_T, is the sum of the effect of all

the contributing mechanisms:

$$P_T = P_e + P_i + P_o + P_s + P_{sp} \tag{25}$$

where P_e is the electronic, P_i is the ionic, P_o is the orientational, P_s is the space charge, and P_{sp} is the spontaneous polarization respectively.

Polarization in an ideal capacitor is instantaneous on application of a field, but in real dielectrics, physical species such as electrons, ions, and molecules have to be moved to produce the polarization. These species have an inertia that delays response to the field, resulting in a polarization that lags behind the applied field. A measure of this lag is the relaxation time, which may be a single time but often is a spread of times. Two things result from the relaxation. First, the polarization depends on frequency because it the signal frequency is too high, processes with long relaxation times (slow processes) will not be able to follow the changes of the field and hence will not contribute to the polarization. Second, power is dissipated as the dipoles are moved against the forces that cause them to lag. This produces loss which, again, is frequency dependent. Figure 10 shows the variations of dielectric constant (polarization) with frequency and the regions of operation of the various types of polarization.

By an analysis of the relaxation process [37], the Debye equations relating permittivity to relaxation time and frequency can be obtained. For a single relaxation time,

$$\varepsilon = \varepsilon' - j\varepsilon'' = \varepsilon_\infty + \frac{\varepsilon_s - \varepsilon_\infty}{1 - j\omega\tau} , \tag{26}$$

$$\varepsilon' = \varepsilon_\infty + \frac{\varepsilon_s - \varepsilon_\infty}{1 + \omega^2\tau^2} , \tag{27}$$

$$\varepsilon'' = \frac{(\varepsilon_s - \varepsilon_\infty)\omega\tau}{1 + \omega^2\tau^2} , \tag{28}$$

and

$$\tan\delta = \frac{\varepsilon''}{\varepsilon'} = \frac{(\varepsilon_s - \varepsilon_\infty)\omega\tau}{\varepsilon_s + \varepsilon_\infty\omega^2\tau^2} . \tag{29}$$

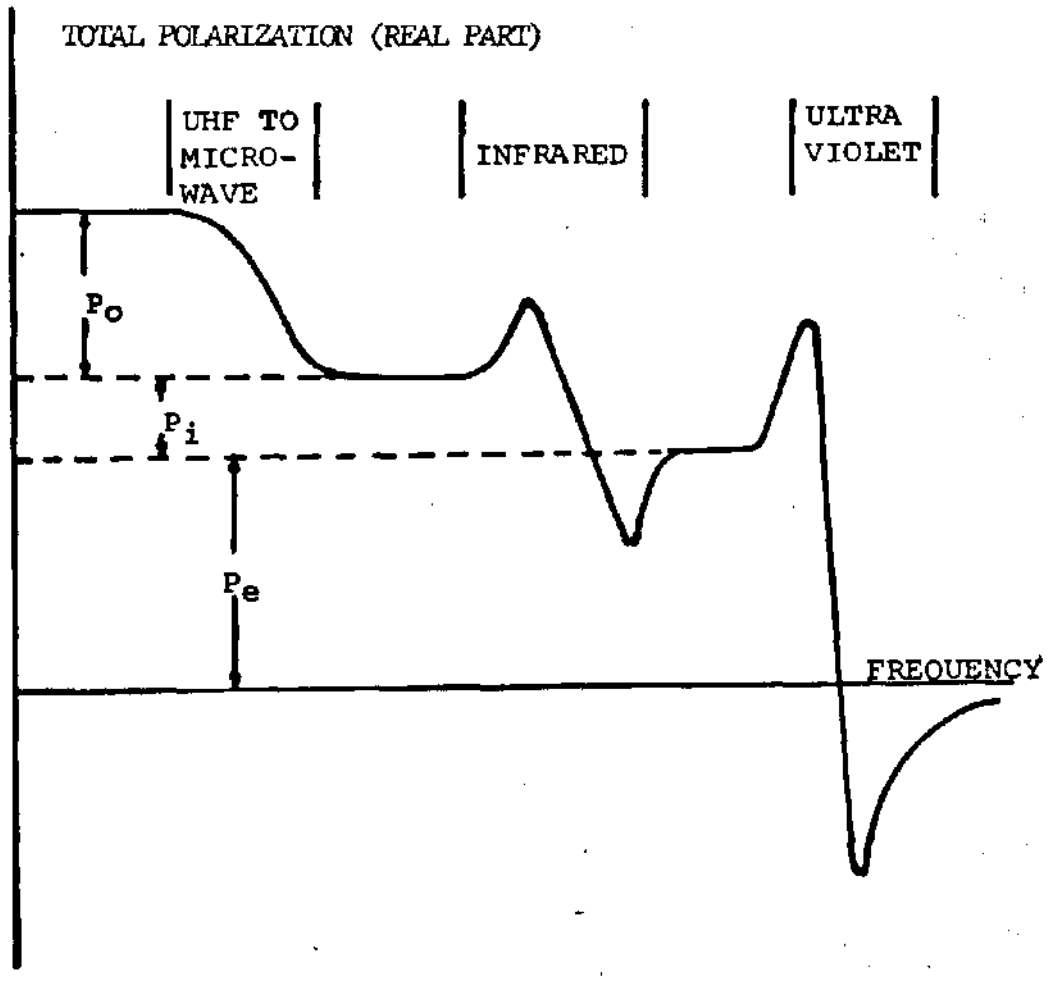


Fig. 10. Frequency Dependence of the Several Contributions to Polarization (Schematic).

where ε_s and ε_∞ are the static and infinite frequency dielectric constants respectively and τ is the relaxation time. For a spread of relaxation times Cole and Cole [38] showed that Equation (26) should be replaced by the more general expression,

$$\varepsilon' - j\varepsilon'' = \varepsilon_\infty + \frac{\varepsilon_s - \varepsilon_\infty}{1 + (j\omega\tau_a)^{(1-K_d)}} \quad , \tag{30}$$

where τ_a is the mean relaxation time and K_d is a constant of a value between zero and one.

Cole and Cole [38] showed that if a Debye type relaxation exists in a material, a plot of ε'' against ε' over the entire frequency range (a Cole-Cole plot) should give a semicircle. Such a Cole-Cole plot is sketched in Figure 11(a) for a single relaxation time. If there is a

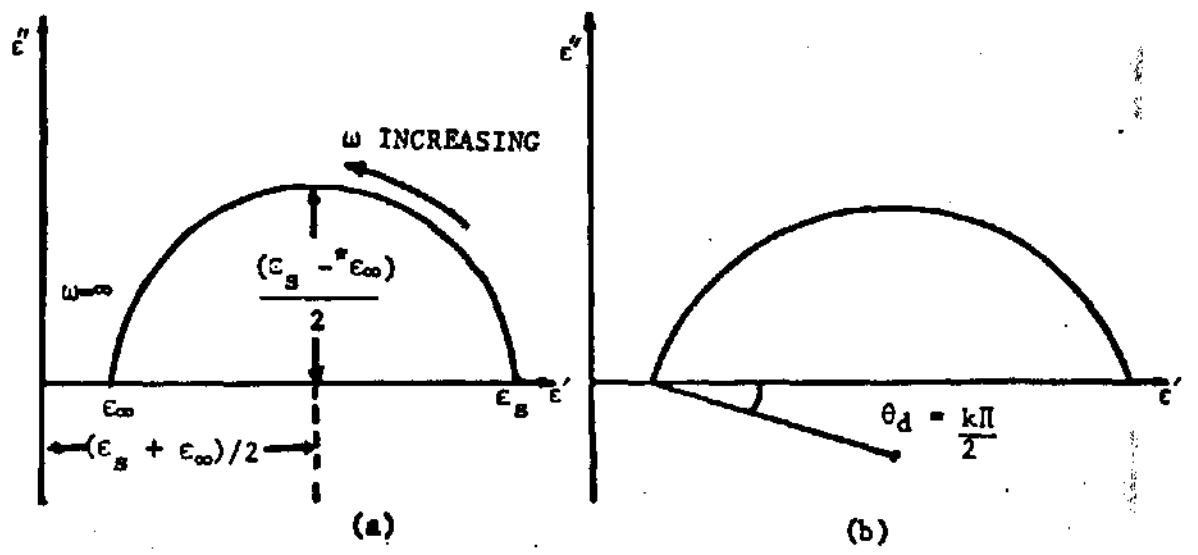


Fig. 11. Cole-Cole Plot for (a) Single, (b) Spread of Relaxation Times.

spread of relaxation times and Equation (30) applies, a Cole-Cole plot still yields points lying on a circle but the center of this circle will be depressed below the ε'-axis as shown in Figure 11(b) with the angle of depression Θ_d depending on the constant K_d.

The components of ac conduction or loss as a function of frequency are of three kinds: (1) A dc conduction contribution is present as a constant resistance independent of frequency. Using the parallel model, constant resistance translates into a reciprocal relationship between loss tangent and frequency according to Equation (23). (2) There is a contribution from the relaxation mechanisms described earlier. These will be present as loss peaks (relaxation peaks) whose peak frequencies will depend on the type of polarization mechanisms involved. (3) A frequency independent loss behavior is generally observed in insulator films which has been attributed to a distribution of relaxation times. These various components are shown schematically in Figure 12.

2.2.1.4 Impedance Spectroscopy

Impedance spectroscopy was first applied to ceramic systems (stabilized ZrO_2) by Bauerle in 1969 [39]. Since then, the method has gained popularity for the study of ceramic solid electrolytes such as stabilized ZrO_2 [40] and thoria. This method is yet to be applied to thin electrolyte films, probably because only recently are such electrolyte films being investigated.

The method involves the measurement of the admittance or impedance of the sample on the application of a small ac signal. The admittance is the reciprocal of the impedance and is a complex quantity

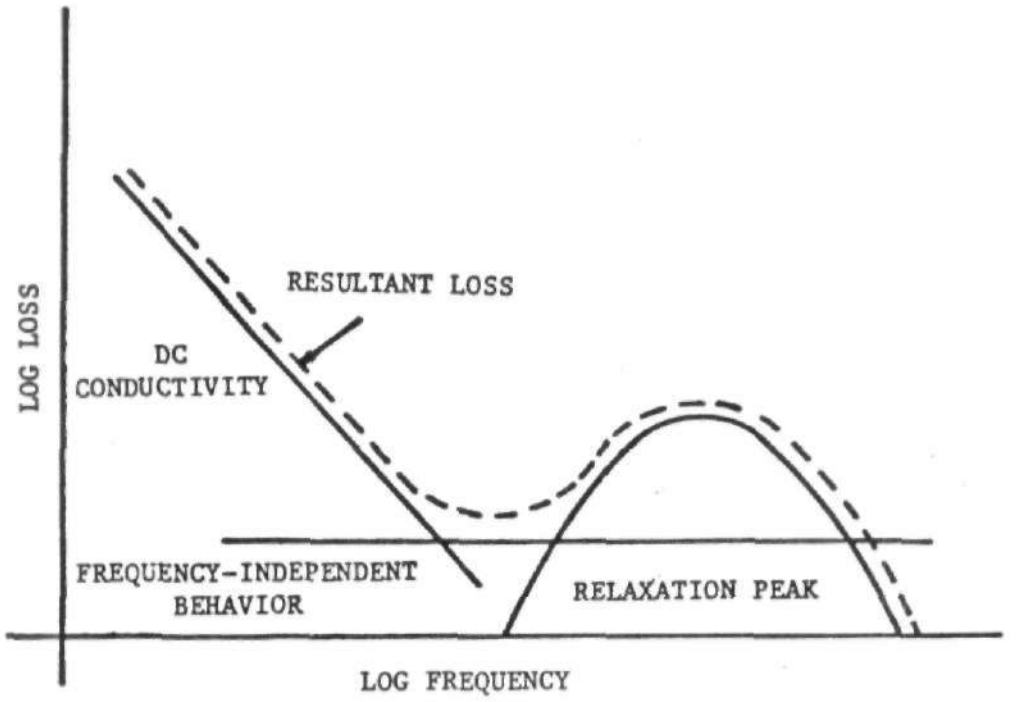


Fig. 12. Loss vs Frequency Showing the Effect of the Various Ac Conduction Processes.

that is represented as

$$A = \frac{I}{Z} = G + jB$$

where G and B are the real and imaginary parts of the admittance respectively. A plot of B against G gives a number of semicircles which can be used to determine a particular equivalent R-C circuit producing the behavior. A simple parallel model for the dielectric behavior was assumed in the previous discussion; however, the real model is often more complex. Figure 13 exhibits calculated admittance plots for some simple R-C circuits.

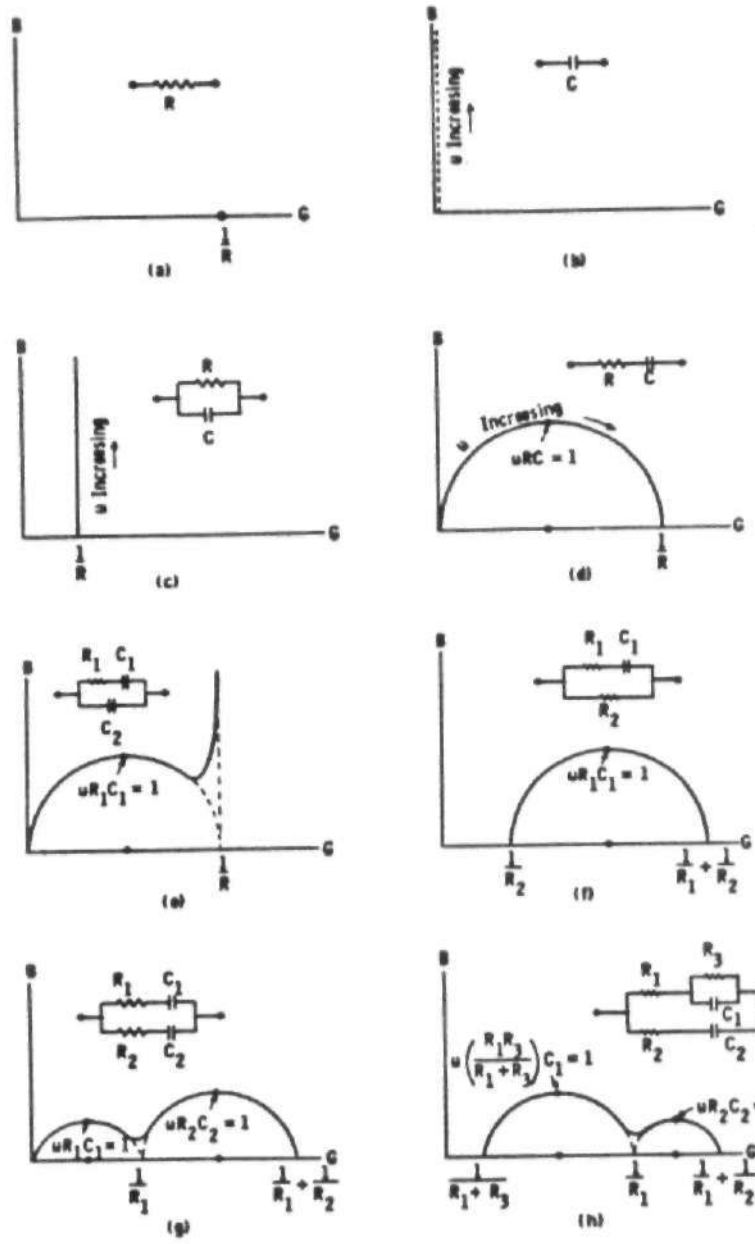


Fig. 13. Admittance Plots for Some Simple R-C Circuits.

One advantage of this method is that the different semicircles of the admittance plot, or impedance plot, can be ascribed to the effect of various physical components of the structure, such as intragrain, grain boundary, and electrode effects. This is illustrated in Figure 14, where a complete admittance plot for a solid electrolyte showing all the possible semicircles is sketched, and the equivalent circuit for the plot is presented. The resistance values of the equivalent circuit can be derived from the admittances of the admittance plot as follows:

$$\frac{1}{G_{dc}} = R_{le} + R_{he} + R_{GB} + R_{B1} + R_{B2}, \tag{32}$$

$$K_{le} = 1/G_{dc} - 1/G_2, \tag{33}$$

$$R_{he} = 1/G_2 - 1/G_3, \tag{34}$$

$$R_{GB} = 1/G_3 - 1/G_4, \tag{35}$$

$$R_{B1} = 1/G_4 - 1/G_5, \tag{36}$$

$$R_{B2} = 1/G_5, \tag{37}$$

where the subscripts le, he, and GB refer to low frequency electrode, high frequency electrode, and grain boundary respectively. Subscripts B1 and B2 refer to bulk or intragrain. The capacitance values can be similarly related to the admittance but this is not done here. from the equivalent circuit of the behavior, a physical model can be derived to provide insight into the conduction process. Another advantage of the

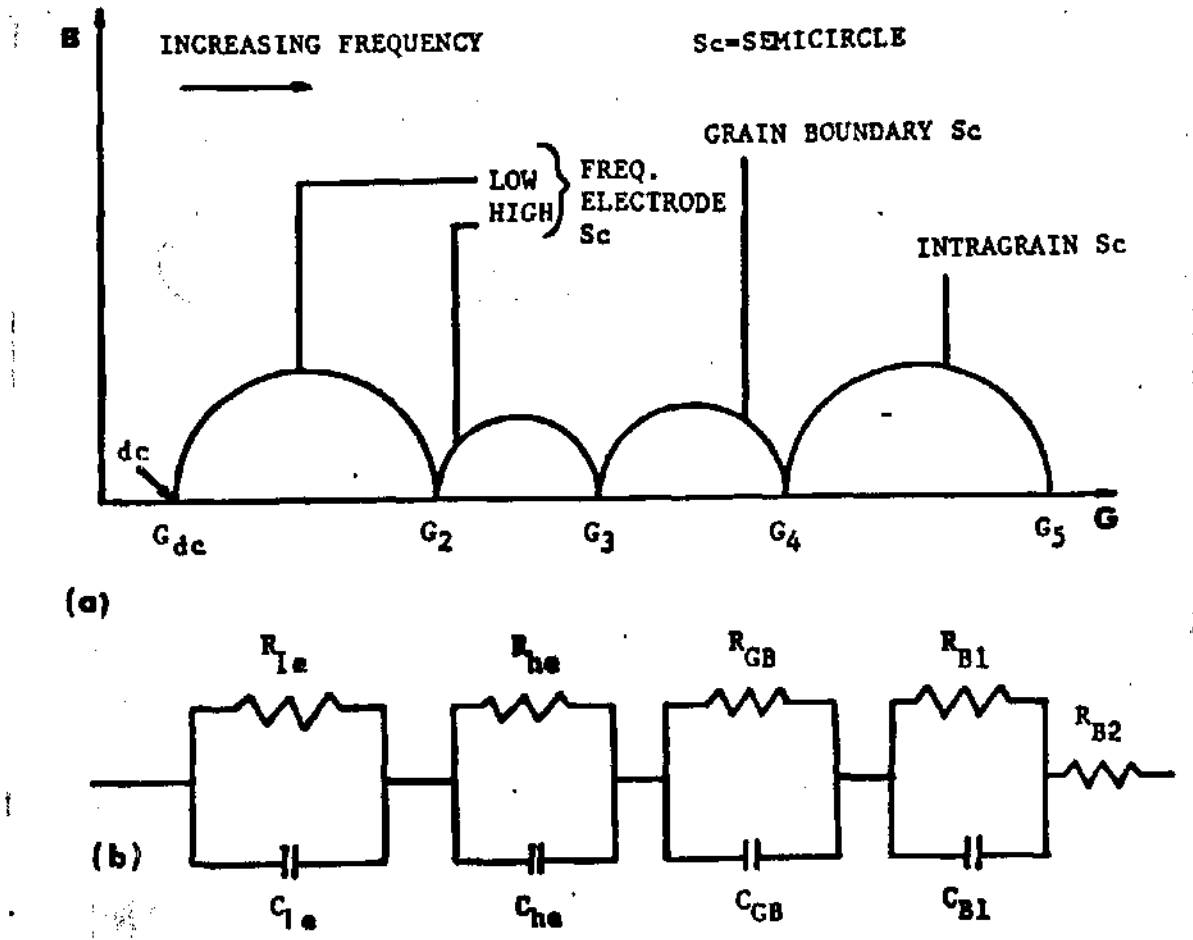


Fig. 14. Schematic Admittance Plots (a), and the Equivalent Circuit (b).

method is that the individual capacitors and resistors of the equivalent circuit can be ascribed to specific chemical and physical processes in the material which permits study of such processes. For instance, the electrode resistance has been particularly useful in the study of the kinetics and mechanisms of the electrode reactions in solid electrolytes [39].

The experimental equipment used for measuring the admittance, sources of experimental error, semicircle identification, and other experimental considerations have been discussed by Kleitz et al [41]. The equipment used includes ac bridges (most accurate), correlation function analyzers and lock-in amplifiers. The lock-in amplifier method will be described in the Procedure Section.

2.2.2 Dc Conduction

With regard to electrical conduction, solids may be classified into three general groups: the metals, with conductivities of about 10^{-4} to 10^{6} ohm^{-1} cm^{-1}; the semiconductors, with conductivities in the range of 10^{-9} to 10^{3} ohm^{-1} cm^{-1} and insulators (10^{-10}-10^{-17} ohm^{-1} cm^{-1} at room temperature). ZrO_2 ordinarily would be an insulator but, under certain conditions, can behave as a semiconductor. Furtunately the electrical conduction in insulators and semiconductors involve similar mechanisms, so that a discussion of the various dc conduction mechanisms in insulators will suffice to reveal the approaches that can be used to interpret the dc conduction results for ZrO_2. First a description of energy band structure will be presented, followed by a discussion of various conduction mechanisms.

The energy band structure of a crystalline insulator in contact with two metal electrodes, under the influence of an electric field is depicted schematically in Figure 15. This band structure may not be the most appropriate for the less ordered structures commonly found in thin film polycrystalline and amorphous structures. The true picture for such cases ought to be a smeared-out valence and conduction band with a less well defined energy gap. However, this model has been found to be

sufficiently accurate for most analyses of the energy gap in insulators. Note that the valence and conduction bands of insulators are usually curved at the interface.

The Fermi levels of metals (in conduction bands) and the insulators (in the middle of the forbidden band) are equal, as is required for solids in contact, and the insulator bands are tilted relative to the metal bands by the applied field. Usually, the metal work function ϕ_m, is less than that of the insulator ϕ_c. For instance, zirconium, and molybdenum have work functions of 4.1 and 4.6 eV respectively, as compared to about 5 for ZrO_2. The use of electrodes of these metals on ZrO_2 would produce the so-called ohmic contact, which simply implies that the electrodes supply electrons readily to the insulator because of their lower work function. Platinum however,has a ϕ_m of 5.6, which is slightly higher than that of ZrO_2 and so is expected to produce either a slightly blocking (electrons not supplied readily) or a neutral contact. Two trapping levels are shown in the figure, but the real distribution of traps in any insulator may be less or more complex. To understand this, the origin of traps in an insulator must be described.

Traps are energy levels in the forbidden band produced by impurities and defects, such as vacancies, interstitials, dislocations and grain boundaries. How they are generated may be illustrated with some aspects of defect chemistry in ZrO_2. ZrO_2 at low oxygen partial pressures, becomes oxygen deficient through an oxygen vacancy mechanism as follows:

$$O_o \rightleftharpoons V_o + 1/2O_2 \quad , \tag{38}$$

$$V_o \rightleftharpoons V_o^{\cdot} + e' \quad , \tag{39}$$

$$V_o^{\cdot} \rightleftharpoons V_o^{\cdot\cdot} + e' \quad , \tag{40}$$

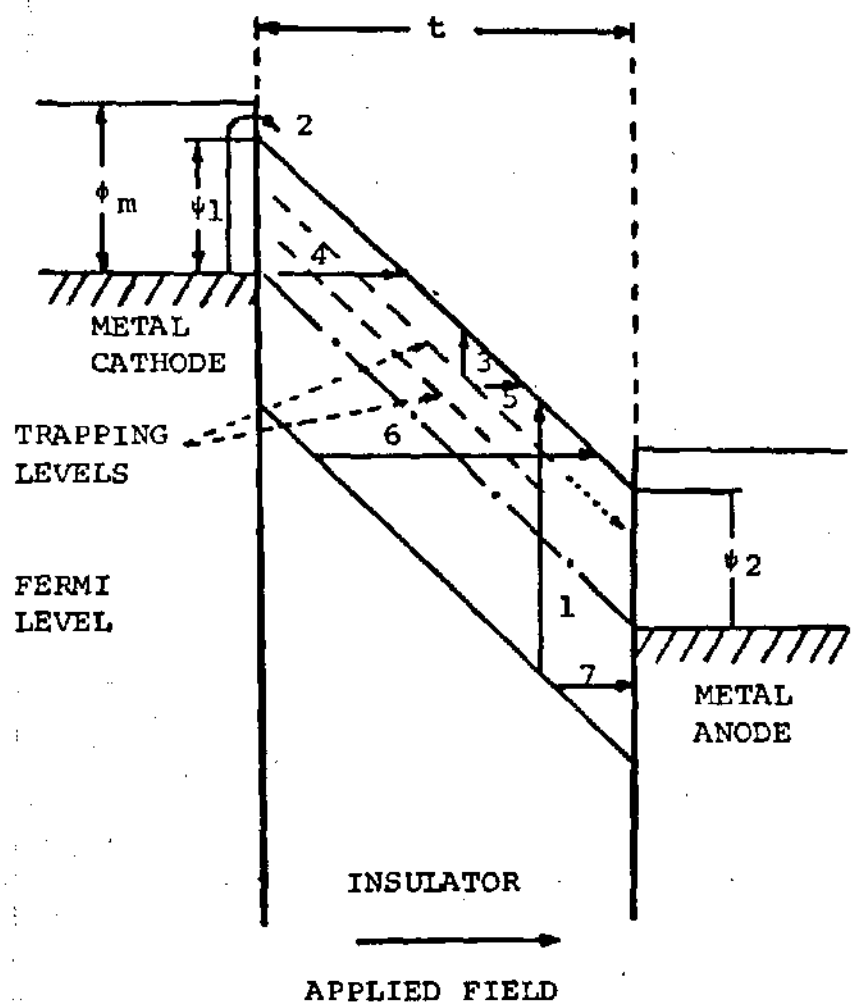


Fig. 15. Diagram of the Various Conduction Processes in a Thin Film Dielectric at High Fields.

This mechanism generates unionized, and singularly and doubly ionized, oxygen vacancies, whose energy levels are depicted in Figure 16. It is known [42] that, under these conditions, the doubly ionized vacancies and electrons are the predominant defects for ZrO_2. Hence the $V_o^{\cdot\cdot}$ level may be the dominant trapping level. In other materials, trapping levels may be considerably different. At high oxygen pressures, on the other hand, ZrO_2 becomes oxygen-rich by an interstitial mechanism [42]:

$$1/2\ O_2 \rightleftharpoons O_i, \tag{41}$$

$$O_i \rightleftharpoons O_i' + h^{\cdot}, \tag{42}$$

$$O_i' \rightleftharpoons O_i'' + h^{\cdot}, \tag{43}$$

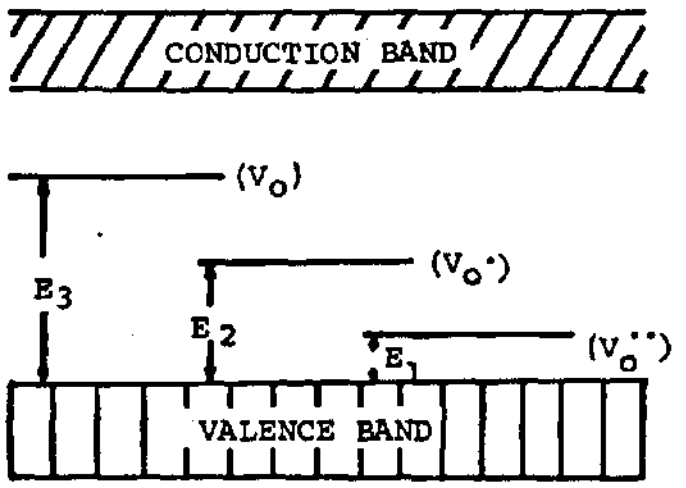


Fig. 16. Schematic Representation of Energy Levels of Oxygen Vacancies in ZrO_2.

and if the ZrO_2 is doped with an impurity such as Y_2O_3, for example, vacancies are produced [42]:

$$Y_2O_3 \rightleftharpoons 2Y' + V_o^{\cdot\cdot} + 3O_o \tag{44}$$

The interstitials and vacancies again lead to different trapping levels with different possible distributions. It can thus be seen that the type and distribution of trapping levels will depend on the defect mechanisms operative in the material, which in turn depend on factors like the type of material, temperature, and component (e.g., oxygen) partial pressures.

Conduction in an insulator may be electronic, when the current is carried by electrons and holes (moving in opposite directions) or ionic, when the current is carried by ions. These carriers move through the material by a variety of mechanisms which may be divided into high-field and low-field processes. High fields enhance conduction by lowering the barrier heights. Listed below are the conduction mechanisms which are operative at high fields. All of the processes are non-ohmic unless otherwise stated and are illustrated in Figure 15.

1. Electronic conduction
    1. Field assisted thermal emission (processes 1,2,3).
    2. Tunneling and internal field emission (processes 4,5,6,7,8).
    3. Electron hop (process 9). -Ohmic.
    4. Space-charge-limited-currents (SCLC).
2. Ionic conduction. -Ohmic

Low field conduction processes occur below 0.1 MV/cm, where most insulators have an ohmic conduction. Under these conditions, tunneling

can occur only in films less than 30 Å thick, which are too thin to be of any significance. Emission into the conduction band is not favored. Electron hop and ionic conduction are thus the only likely mechanisms at low fields. Each of the conduction mechanisms is discussed below in detail. However, tunnelling processes are omitted as these are not likely in the thick films ($\sim$ 2μm) of concern here.

2.2.2.1 Field Assisted Thermal Emission

Three possible mechanisms arise from processes that involve thermal emission of electrons into the conduction band: intrinsic conduction, Schottky, and Poole-Frenkel mechanisms. Intrinsic conduction is unlikely because of the high energy gap involved. For both Schottky and Poole-Frenkel mechanisms, the potential barrier involved is lowered by the field.

Schottky conduction involves electron emission from the metal at the negative potential, analogous to thermal emission except that the metal-insulator barrier height is lowered by the applied field. The current density is given by:

$$J \approx \Psi(1- r)\ T^2 \exp - \left[\frac{\phi - \alpha F^{1/2}}{KT}\right], \qquad (45)$$

where F_i is the field at the interface which is usually assumed as the average field in the insulator, Ψ is the Richardson-Duschman constant ($\sim$ 120 $AcmAcm^{-20}K^{-2}$), r is the reflection coefficient, e is the charge of an electron, and α is the parameter of Schottky effect defined by

$$\alpha = (e\ /4\pi\varepsilon)^{1/2}, \qquad (46)$$

where ϵ is usually considered to be the high frequency dielectric constant.

In the case of Poole-Frenkel conduction, the potential barrier lowered by the field is that between a trap and the conduction band. Hence the bulk of the sample is involved rather than an interface. This conduction in the simplest case, may be represented by

$$J = J_o \exp -\left[\frac{\phi - 2\alpha F^{1/2}}{KT}\right], \qquad (47a)$$

$$J = J \exp -\frac{\phi}{KT} \exp(\beta), \qquad (47b)$$

where β is the parameter for the Poole-Frenkel effect and J_o is the pre-exponential factor. Many complications can arise for this mechanism. If the trap is not coulombic, the exponent of F will not be one-half. If the electron does not leave the trap in the field direction, an integration over the distribution of electrons is required. In this case, β ought to be replaced by $2[1+(\beta-1)\exp(\beta)]/2$. Equation (47) is sensitive to defect structure and for some types of trap distributions, Poole-Frenkel conduction becomes identical to the Schottky effect. Finally, the pre-exponential factor, J_o, depends on the details of the conduction. For equations (45) and (47), a plot of ln J vs the square root of the field or voltage should give a straight line with a slope of α/K and $2\alpha/K$, in the simplest cases of Schottky and Poole-Frenkel conduction respectively. With more complex cases, the two mechanisms may be difficult to distinguish experimentally. Also, the possibility exists for these two mechanisms and others to occur

simultaneously, with trap distributions that are practically unknown.

Once electrons reach the conduction band of an insulator by any of the emission or tunneling processes, they should move fast (high mobility) through the ideal crystal. In this case, electrons do not accumulate in the conduction band to produce space charge because the electron emission processes are slower. However, in real insulators, electrons are scattered by lattice vibrations as in metals, causing significant reduction of the electron mobility at high temperatures. Trapping levels are present which hold the electrons as they move through the conduction band to later be re-emitted. This further reduces the mobility of the electrons in the conduction band. The reduction in carrier mobility by either or both processes may be to such an extent that space charge accumulates in the conduction band or in traps as conduction in the conduction band becomes the limiting process. A thorough discussion of these mechanisms has been given by Lampert [43] and Rose [44]. The conduction depends on the number of carriers (one or two), the presence of traps and/or recombination centers, and their distribution. The conduction in a trap-free insulator is given by the Mott and Gurney law:

$$J = 9\mu\varepsilon\varepsilon_{o}V^{2}/8t^{3}, \tag{48}$$

where μ is the electron mobility and t is the sample thickness. For a single trapping level we have the modified Mott and Gurney law:

$$J = \Theta' 9\mu\varepsilon\varepsilon_{o}V^{2}/8t^{3}, \tag{49}$$

where Θ is the ratio of free charge carriers to free-plus-trapped

charge. For traps distributed uniformly throughout the band gap

$$J = e\mu n_o \frac{V}{t} exp\left(\frac{\varepsilon\varepsilon_o V}{eN_t KTt^2}\right), \tag{50}$$

where N_t is the trap density per unit volume and per unit energy and n_o is the equilibrium free carrier concentration. There are also equations for exponential distribution of traps and other types of trap distributions, but these are omitted from this discussion.

In the Mott and Gurney laws, conductivity is proportional to $\sqrt{V}$ (square law) and $1/t^3$, which are characteristics that can be used to identify it. Typical one-carrier SCLC behavior for an insulator is illustrated schematically in Figure 17.

2.2.2.2 Ohmic Conduction Processes

Ohmic conduction processes for insulators include electron hop and ionic conduction. The electron hop process is sometimes referred to as impurity conduction. It involves the conduction of current by electrons or holes in the forbidden band hopping from one trap site to another over energy barriers, as illustrated in Figure 18 where the arrow indicates the movement of the electrons. This process requires the presence of acceptor and donor sites in the forbidden band. The more disordered the structure of the insulator, or the higher the impurity content, the more extensive are the trapping levels (structura and impurity traps) that could contribute to this type of conduction.

The current is carried in ionic conduction by ions (cations and/or anions) and vacancies jumping from one defect site to another

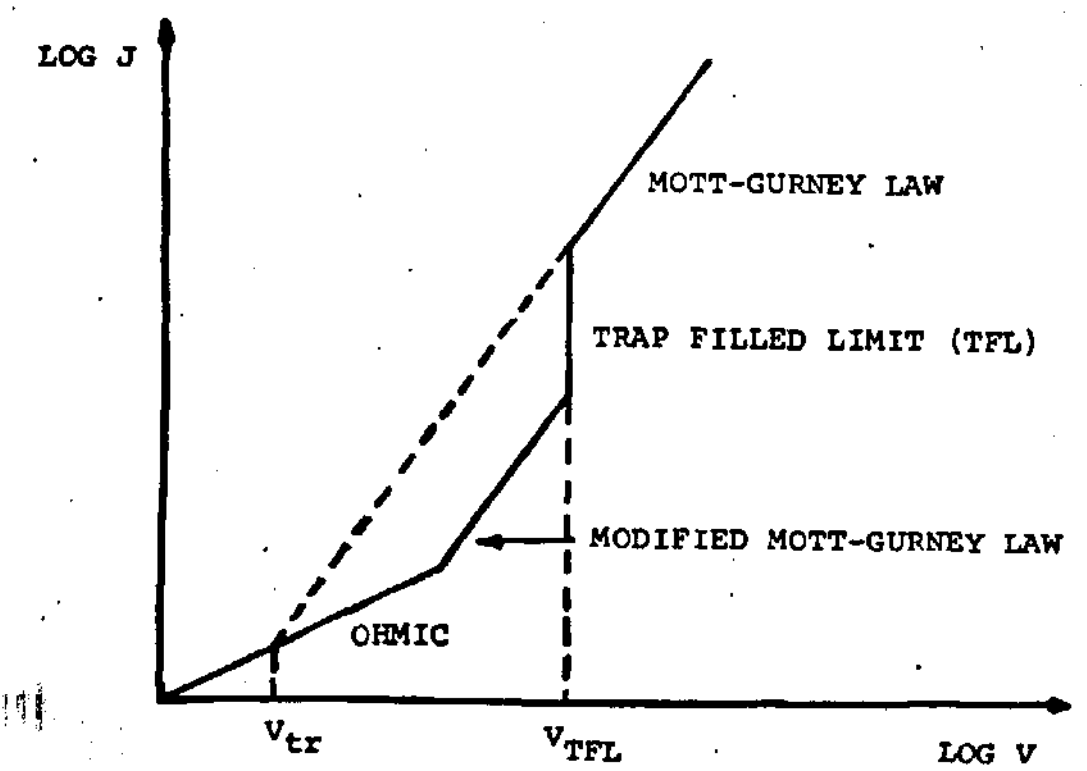


Fig. 17. One Carrier SCLC-Voltage Characteristics for An Insulator With A Single Trap Level.

across energy barriers. Under an applied field, these jumps produce a drift of the ions. In some solids, the cations are the major carriers but in others such as ZrO_2, the anions (oxygen in ZrO_2) is the major carrier. In this process, the ions have to be discharged at the electrodes in order for conduction to occur. Electrode reactions can occur that may or may not limit the rate of the process. For instance, the transfer of current by oxygen ions in ZrO_2 is illustrated in Figure 19. If by any means such as very low oxygen partial pressures, the electrode discharge processes are prevented, charge soon accumulates at the electrodes, creating polarization.

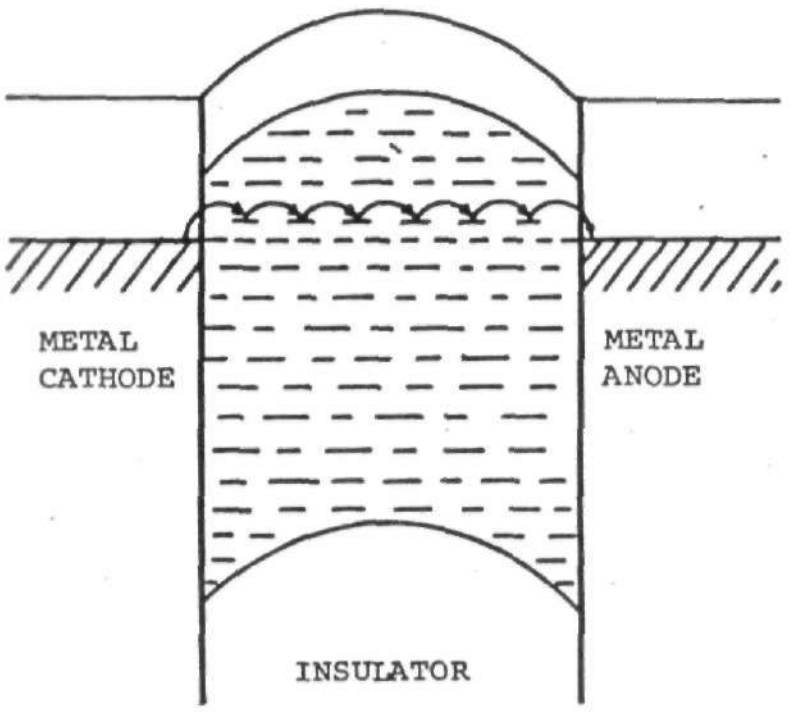


Fig. 18. Energy Band Diagram Showing Electron Hop.

Defects in the structure can influence the conduction considerably. In ZrO_2, oxygen vacancies constitute a mechanism by which the oxygen ions drift through the solid, and often these vacancies are intentionally introduced into the structure to enhance oxygen ion transference number (fraction of the total current carried by oxygen ions). For example, cubic stabilized ZrO_2 electrolytes have the number of oxygen vacancies fixed by the amount of stabilizers used. Oxygen transference numbers of about one are realized in such materials at

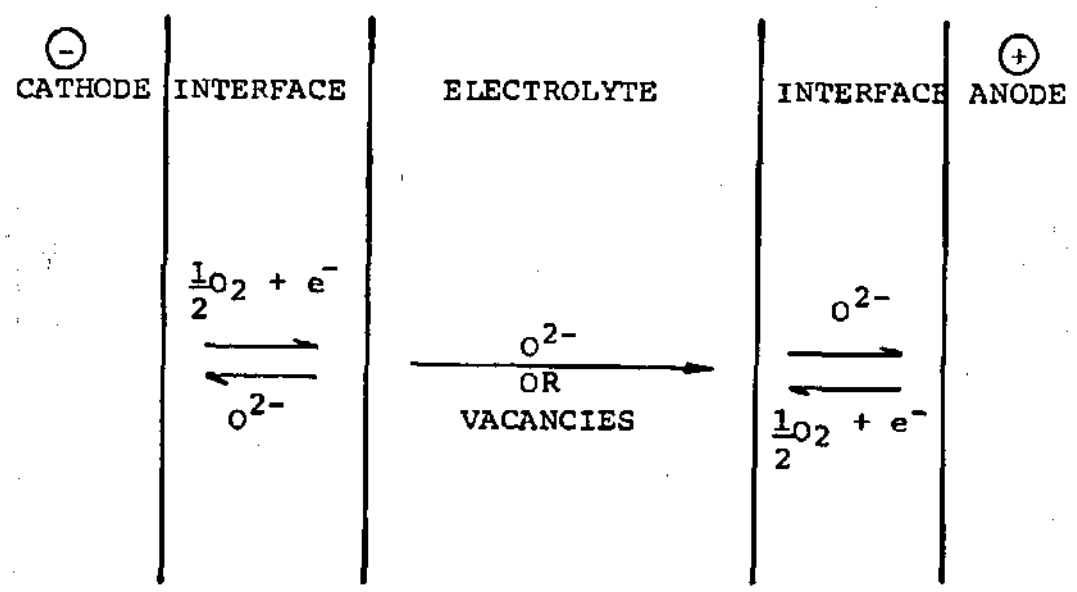


Fig. 19. Ionic Conduction by Oxygen Ions in an Electrolyte.

elevated temperatures.

Harrop and Campbell [45] presented three behaviors of ionic conduction processes as field is increased. For fields less than 10 V/cm, and Fel << kT 9

$$J = \frac{C}{kT} \exp -\left(\frac{\phi}{kT}\right), \tag{51}$$

where ϕ is the energy barrier for the hopping process, l is the separation of the barriers and C is a constant. For Fel = kT, the barrier is appreciably distorted by the field and

$$J = \overline{C} \exp -\left(\frac{\phi}{kT} - \frac{Fel}{2kT}\right). \tag{52}$$

When Fel>>kT, the analysis becomes complex, as multiple hops can occur in this region.

Both ionic and electron hop conduction can be represented by an Arrhenius type Equation of the form

$$\sigma = \sigma_o \exp(-E/kT), \tag{53}$$

where σ_o is a constant and E is the activation energy of the process. An Arrhenius plot will usually show increasing linear slopes (activation energies) with increasing temperature as is illustrated in Figure 20.

It is often quite difficult to distinguish between ionic and electronic currents, especially if the activation energy is large. An activation energy of 0.1eV and a high charge mobility are usually associated with electronic conduction, whereas a value > 0.6 eV with a low mobility, can be either ionic or electronic conduction. Other characteristics of ionic conduction that have been used to distinguish it from electronic conduction, though not always clearly, are as follows:

1. Slow polarization effects should occur, producing a transient current which decays with time so long as the ionic species is not discharged at the electrodes. However, similar transient currents can be produced by electron trapping and dielectric relaxation.
2. Material transport may occur, but it would take years to observe any significant changes with the low current levels used for most testing.
3. Delay time between an applied voltage pulse and the current

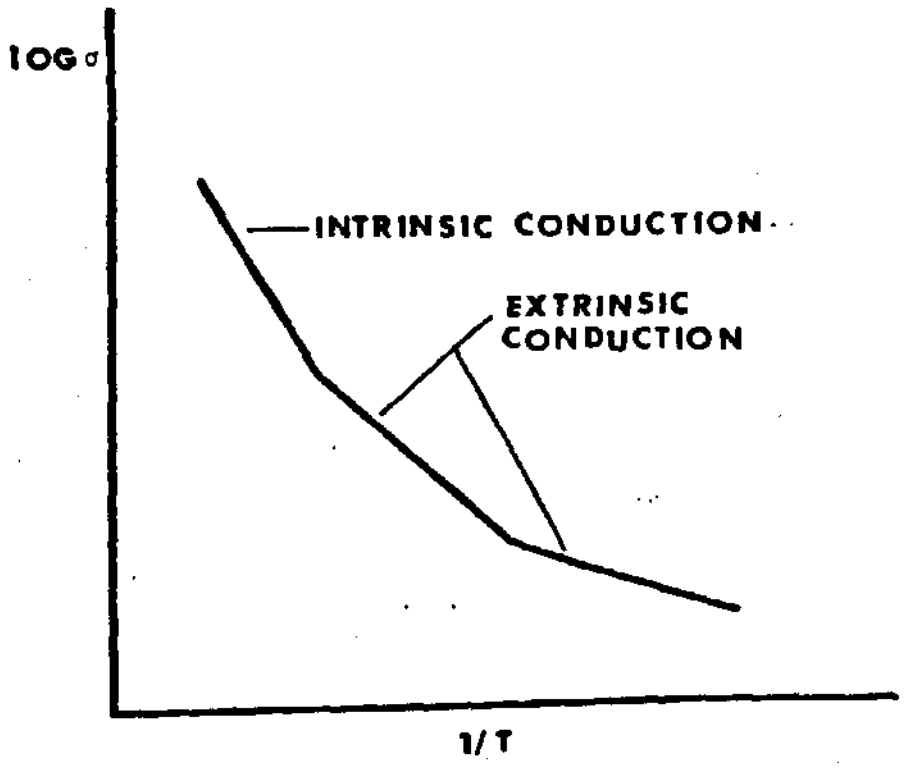


Fig. 20. Arrhenius Plot of Conductivity of A Typical Insulator (Schematic).

pulse response, caused by long transient times for ions, was used successfully by Mead [46].

2.2.3 Conduction in ZrO_2 Thin Films

Most of the work done to date on dc conduction in ZrO_2 thin films has been on anodized and oxidized or corroded samples. Sputtered films, especially the stabilized cubic form, have been studied, though not to as great an extent as pure ZrO_2. Evaporated films have had little study. Investigation of ac conduction in plasma sprayed samples have

been reported in the literature [47], but this survey will not include those results since the properties of such films are significantly different from those of concern in this work. The following will also be omitted from this survey: (1) Conduction in anodized films where a liquid electrode is used, such as the results of Charlesby [48], Wood and Pearson [5], and Vermilyear [49]. Liquid electrodes introduce eletrochemical processes that are not of interest here. Furthermore, water will be present in the films to yield conduction that is totally different from that of dry films. (2) Studies concerned mostly with switching phenomena such as those of Hickmott [50] and heat stimulated currents (e.g., Zudov and Zudova, [51]) both of which are out of the scope of the present work. (3) Results of sputtered YSZ films of Greene et al [9], CSZ films of Croset et al [10], and Calcium implanted films of Croset et al [15]. These are the major published works on electrical properties of stabilized ZrO_2 films to date, but the main thrust in this work is pure ZrO_2 films. It may be noted, however, that oxygen ion transference numbers ranging from zero (Greene et al [9]) to one (Croset et al [10]) at temperatures of 25° -400 °C have been reported for stabilized films, indicating a range of conduction mechanisms from purely electronic to purely ionic.

2.2.3.1 Ac Conduction

Harrop and Wanklyn [6] studied the bulk dielectric spectra of dry ZrO_2 films prepared by anodization and steam corrosion on electropolished and pickled zirconium surfaces. The second electrode was either silver paint or Au/Pd. Anodic films gave a frequency independent dielectric constant of 22, in good agreement with wet

measurements [52], indicating that significant electrode polarization did not occur. Conduction was ohmic with anodic films exhibiting low loss consistent with near stoichiometric structure whereas corrosion films showed high losses with a loss peak for those corroded on pickled surfaces. The loss peak was attributed to dipole polarization produced by substitutional or interstitial flourine ions in the oxide film The activation energy of the orientation polarization was 0.72 eV, with the fluorine ion concentration in a film of 1500 Å thickness calculated to be 10^{20} ions /cc.

Dawson and Creamer [3] studied ac conduction in anodized ZrO_2 films using various counter electrodes, (Ag, Au/Pd, Au and indium). The film thickness was in the range 2000-4000 Å. For gold and Au/Pd elecrodes, reproducible results were obtained once the films had been heated to 180 °C, but the electrodes blistered with a resultant decrease in area of contact between the ZrO_2 and the electrode if the temperature exceeded 300 °C. Indium electrodes tended to reduce the conductivities, producing an activation energy of 0.56 eV for temperatures of 250-300 °C. This was attributed to an n-type electronic conduction with an Arrhenius-type conductivity-temperature relationship. The decrease in conductivity produced by the indium electrode was attributed to the substitutional diffusion of In^{3+} ions into the Zr^{4+} lattice, constituting electron traps and hence reducing the effective number of free carriers. However, note that the only electronic process to yield ohmic conduction would be electron hop, which acting alone, would have an activation energy less than 0.1 eV. Hence, the high activation energy of 0.56 eV obtained here suggests that other mechanisms, such as

interfacial polarization or even ionic conduction, were operative.

Chan and Loh [2] studied ac and dc properties of anodic ZrO_2 films over a wide range of temperatures and frequencies. As regards the ac properties, they obtained a dielectric constant of 25 at 1000 Hz, independent of film thickness. The conductance showed two distinct dispersion regions. At frequencies below 10^4 Hz, the conductance, G, was proportional to frequency, f, and at frequencies above 10^4 Hz, $G \propto f$ and insensitive to temperature. A gradual variation of activation energy, E, at fixed frequencies was obtained. Above 27°C, a single E of about 0.3 eV was approached for all frequencies. The ac conduction was observed to be over two orders of magnitude higher than the dc conduction. Thus, either the conduction mechanisms were different, or the charge transport was more efficient under ac conditions. An electron hop mechanism was proposed to explain the results.

Tauber, Dumbri, and Caffrey [11] measured several dc and ac electrical properties of pyrolytic ZrO_2 formed on silicon using aluminum as the counter-electrode. For 2000 Å films, a dielectric constant of 17 was obtained at room temperature, independent of frequency. This value is lower than the value of 22 ± 3 obtained by Harrop and Wanklyn [53] for a single crystal ZrO_2 of unspecified orientation. The lower dielectric constant indicates the possibility of porosity or significant disorder in the films. A $\sigma_d \propto f^y$ dependence was obtained, where y was a temperature dependent parameter, approaching unity near room temperature and decreasing with increasing temperature to 0.5 at 300°C. The conductivity in the range 10^3-10^5 Hz was attributed to the remanence of

a low-frequency Debye-type mechanism. Morley et al [54], when considering the Cole-Cole form of the Debye equation for frequencies greater than the relaxation frequency, have shown that conductivity can be approximated by

$$\sigma = \epsilon_o (\epsilon_s - \epsilon_\infty)(2\pi)^y f^y / \tau_a^{(1-y)} , \qquad (54)$$

where ϵ_o, ϵ_s, and ϵ_∞ are permittivities of free space, the static and high frequency limits of the real part of the dielectric constant, respectively, and τ_a is the mean or most probable relaxation time. For a broad distribution of relaxation times, as would be expected at low temperatures, y approaches one; while as the temperature increases and the distribution narrows, y approaches zero. The authors observed no low frequency loss peaks, but suggested that such a mechanism as interfacial polarization may be operative for ZrO_2.

Movchan et al. [13] studied the electrical properties of ZrO_2 condensates 50 μm thick deposited by E-beam evaporation on aluminum and copper at 100°-500° and 150°-600°C, respectively. The electrical properties were related to substrate metal and deposition temperature. However, details of this work were not available at this time other than from the abstract [55]. Another abstract indicates that Muranova and Terpugov [56] studied loss mechanisms in thin-film waveguides of SiO_2-MgO, ZrO_2 and Ta_2O_5 produced by E-beam evaporation and high frequency atomization methods. This literature was also not available at this writing.

2.2.3.1 Dc Properties

Misch and Gunzel [7] studied anodic and corrosion films on zirconium and found that the conduction in these films (0.6, 0.75, 0.9, and 1.5 μm thick) increased during heating in vacuum. The conductivities also increased with time, a change that was attributed to the diffusion of anion vacancies into the oxide, with an estimated diffusion coefficient of 4×10^{-13} cm /sec.

Later, Misch [8] studied anodized, thermally oxidized, and corroded ZrO_2 films with aluminum and zirconium as counter-electrodes. The resistance of the films was measured in air at room temperature and in vacuum at temperatures up to 290 °C. At room temperature the films were essentially insulators. Upon heating the oxidized films in vacuum to 185° and 290 °C, the resistance dropped and the films became semiconducting. Above 300 °C, the resistance showed a slight drift which was attributed to irreversible diffusion changes.

Vermilyea [57] studied the transient behavior of ionic conduction in anodic oxide films of Ta_2O_5 and ZrO_2 at high fields. He found that activation energy and barrier separation, l, varied with changes in field and temperature for Ta_2O_5 but not for ZrO_2 films.

Zudov and Zudova [58] studied polarization currents as a function of time at room temperature for Al-Al_2O_3-Au and Zr-ZrO_2-Au diodes. The ZrO_2 layer was 700 Å thick and polarization currents were measured both in vacuum ($\sim 10^{-4}$ mm Hg) and at one atmosphere pressure. An analysis of the depolarization current, I_{dep}, vs. time curves showed that the decrease in I_{dep} depended markedly on the atmosphere. The results led the authors to suggest the existence of an additional polarization

mechanism (e.g., ionic). The authors also studied the V-I characteristics of $Zr-ZrO_2$-metal structures, 5600 Å thick, at a constant voltage [59]. The V-I curves had an ohmic segment and an exponential segment. The latter was related to the thermal generation of carriers and the temperature dependence of the current was determined. Conduction was reported to be mainly due to bulk processes. The relation $I \propto \exp(\gamma V_p)$ for $V_p > 30$ V was said to be related to the formation of a negative space charge due to the injected electrons being captured mainly by the cathode traps.

Chan and Loh [2] studied the I-V-T characteristics of anodized ZrO_2 films. Provided the films were heat treated, they showed the following features: at low fields, the conduction behavior was ohmic; at moderate field, the current exhibited an $I \propto F^n$ dependence, where F was the field strength and $n > 1.5$, and at high fields a temperature independent region was seen, along with a very strong field dependence where n could be greater than 16. The usual approach is to take the different regions separately and propose mechanisms for them as was done by Servini and Jonscher [60]. However, Chan and Low have proposed a modified form of the Poole-Frenkel mechanism to cover the entire I-V-T characteristic ranges:

$$I = AT^n \exp\left(-\frac{E}{kT}\right) \operatorname{Sin} \alpha, \tag{55}$$

where I is the current, A is a constant, n takes the values 2,3, or 4, E is the activation energy of the Poole-Frenkel center and α is a parameter which depends on the field and the temperature T. There was a good fit between this equation and the results for the heat treated

sample with n = 2 and E = 0.26 eV. An Arrhenius plot of the current vs 1/T for the ohmic region gave an activation energy of 0.29 eV for temperatures above -73 °C.

Tauber, Dumbri, and Caffrey [11] studied dc and ac conduction in CVD (pyrolytic) ZrO_2 films formed on silicon with an aluminum counter-elecrode. The films were 2000 Å thick. The dc conduction showed an ohmic characteristic for several of the less resistive (10^{12}-10^{14} cm resistivity) films. However, a particularly resistive film (10^{15} cm) showed no ohmic behavior even at the lowest detectable currents (10^{13} A), but rather a power law, $J \propto F^n$ relation where n was 6 when the dot (Al electrode) was placed at a negative potential, and 2.75 and 5 for the dot positive. The authors noted that a specific mechanism was hard to assign to such a power law but suggested that an aspect of SCLC may have been operative for the dot negative.

A study of electron traps in anodic ZrO_2 was conducted by Zudova, Zudov, and Sterkhov [61]. The information available on this work was limited to an abstract. It however, indicated that deep electron traps were found in ZrO_2 (0.5, 0.55, 0.63, 0.73 eV); and shallow levels equally distributed up to 0.4 eV below the conduction band were also found. The total concentration of traps was given as $2 \times 10^{23}/m^3$.

Balog, Schieber and Michman [12] obtained I-V characteristic results for CVD ZrO_2 formed on silicon with an aluminum counter-electrode. Their dot (Al electrode) positive results were similar to those of Tauber et al. presented above. However, their dot negative results showed an $I \propto F$ dependence as compared to $I \propto F^6$ obtained by Tauber et al. above. Their results would indicate that

silicon had a greater tendency to inject electrons than aluminum, in contradiction to the results of Tauber et al. Balog et al also suggested a SCLC mechanism to be operative.

2.2.3.3 Effects of Electrodes and Flaws

Belova,Gorskay, and Zakgeim [62] observed very high resistivities (10^{14}-10^{15} ohm.cm) in both directions for anodized ZrO_2 films with aluminum counter-electrodes, which led them to conclude that there was little rectifying characteristics in those films.

Dawson and Creamer [3] investigated the effect of various counter electrodes on the ac conduction of anodized ZrO_2 films. Gold and Au/Pd were satisfactory at temperatures below 300 °C but blistered above that. The blistering resulted in a smaller contact area and lower conductivities. On heating films with silver electrodes at 260 °C for 12 hours, the conductivity increased by about 30%. On the other hand, heating a film with indium electrodes for 12 hours at 100 °C reduced the conductivity. The latter effect was ascribed to the diffusion of In^{3+} ions into the Zr^{4+} lattice.

The effect of various metal contacts on the dc conduction of anodic ZrO_2 films was investigated by Nicley and Davis [63]. Two techniques with gallium contacts were employed: dipping a fresh surface into a pool of gallium and dipping a surface prepared by rubbing gallium onto the surface with a paper tissue. The apparent dc resistance measured with silver or unrubbed gallium contacts drifted to higher values with time and these contacts and techniques were therefore, considered not useful. The rubbed gallium contacts gave currents that did not drift; however, they conluded that the rubbed gallium contact

was apparently not useful for direct determination of the resistance of the complete film.

Chan and Low [2] studied the I-V characteristics of anodized ZrO_2 at 27°C. The films were 2500 Å thick and various counter-electrodes (Al, Au, Cu, Bi, Ba, Sn, Mg, Ni) were used. The characteritics were similar for all the electrodes, indicating that electrode processes had little effect on the conduction. This was in good agreement with the conclusions of Belova, Gorskaya, and Zakgeim above. The electrodes, however, exhibited differences in their stability characteristics similar to those observed by Dawson and, Creamer [3]. Gold and, to a lesser extent, copper were found to be bad electrodes because of their tendency to diffuse into the dielectric film, causing long-time continuous aging in the electrical properties. Aluminum showed poor adhesion to the dielectric, thus causing mechanical instability. Barium was reactive in air and even when protected by gold (2000 Å thick) was mechanically unstable. Nickel and magnesium, protected by gold, were the most satisfactory for ZrO_2.

Tauber et al. [11] determined the I-V characteristics for CVD ZrO_2, 2000 Å thick using silicon and aluminum electrodes and found a polarity dependence with the dot (Al) negative case showing higher currents. They concluded that if electrons were the conducting species, then silicon had a greater tendency to inject electrons than aluminum contacts. This result is, however, at variance with those above where polarity effects were not observed, but, of course, silicon is not a metal contact and may be slightly oxidized on the surface, thus reducing its tendency to inject electrons.

Vermilyea [48] discussed electronic conduction in anodic oxide films of several metals (Ta, Nb, W, Zr, Al). Flaw conduction, characterized by marked hysteresis effects was concluded to dominate the behavior of thick films. Flaws were defined as a region larger than an atom in size which was chemically or physically different from the remainder of the film. Examples of flaws are voids and regions of different composition or crystal structure. Two mechanisms were suggested for the flaw conduction: one, the opening of physical holes and the other involving some kind of electronic junction. Bulk conduction, involving primarily electron injection into the insulator containing traps, was suggested to dominate in thin films of Ta_2O_5, Nb_2O_5 and WO_3.

2.2.3.4 Experimental Ac and Dc Values

A summary of the various published works on the ac and dc conduction for dry ZrO_2 thin films is presented in Tables 2 and 3 respectively. Relevant information on the films and their properties are included in these tables.

Table 2. Experimental Values for Ac Conduction In ZrO_2 Films

SN References	Typical Loss (Temp.°C)	Freq. KHz	E(eV) (Temp.°C)	tanδ = ?	Conduction Mechanism	Material	Thick-ness (Å)	Electrodes	Atmos-phere
1. Belova Gorskaya and Zakgeim (1961) [61]	0.005 (20)	- -	-	$Exp(f)$		Anodized ZrO_2	-	Zr, Al	-
2. Harrop and Wanklyn (1964) [6]	0.010-0.012 (~150-80)	1.59 22	-		-	Anodized Zro ZrO_2	-	Zr, Ag paint	Vacuum
	0.022-0.08 (150-80)	1.59 -			Fluorine Dipole Polarization	Steam Corroded on pickled surface, Polished surface	1500	or	
	0.008-0.05 (~150-80)	1.59 -			Ohmic			Au/Pd	
3. Dawson and Creamer (1965) [3]	$(2x10^{-10}-2x10^{-9})$* (120-130)	1.59 -	0.56		Ohmic n-type Electronic	Anodized ZrO_2	2000-4000	Zr, Ag Zr, Au/Pd Zr, In	Ar gas
4. Chan and Low (1970) [2]	-	1.0 25	0.3 (>27)	f, f^2	Electron Hop	Anodized ZrO_2	1000	Au/Mg, Zr	Vacuum
5. Tauber, Dumbri and Caffrey (1971) [11]	$(6x10^{-11}-2x10^{-9})$* (27-327)	1.0 17	-	f^y	Interfacial Polarization and its Remenance	Pyrolytic ZrO_2	2000	Si, Al	Dry N_2
6. Husted, et. al. (1971) [4]	0.013	1.0 -	-		-	Ionized Gas Anodized ZrO	6000	Zr, Au	
7. Belog, et. al. (1977) [12]	-	- 17 - 18	-		SCLC		1850	Al, Si - Al	
8. Croset, et. al. (1977) [10]		25	1.18 (200-400)		Ionic Conduction	Sputtered CSZ	500-1700	Al, Si	Ar Gas

** ()* = conductivity values

Table 3. Experimental Values for Dc Conduction In ZrO_2 Films

SM References	Typical ρ(Ω/Cm) (Temp.°C)	Activation Energy E (ev) (Temp.°C)	I = ?	Conduction Mechanism	Material	Thickness (Å)	Electrodes	Atmosphere
1. Belova, Gorskayg and Zakgelm (1961) [61]	10^{14}-10^{15}(<150)	-	-	-	Anodized ZrO_2	-	Zr, Al	-
2. Michaelov, Akimovich and Stefanishing (1965) [14]	-	-	-	n-type semiconducting	E-Beam Evap. ZrO_2	-	-	-
3. Zudov and Zudova (1968) [58]			F and Exp. (F)	SCLC	Anodized ZrO_2	5600	Zr, Metal	-
4. Chan and Loh (1970) [2]	-	.29 (>-73)	F And F^2, F^3, F^4	Modified Poole-Frenkel	Anodized ZrO_2	1000	Au/Mg	Vacuum
5. Tauber, Dumbri and Caffrey (1971) [11]	10^{12}-10^{15}	-	F, F^6 F^2-8,5	SCLC	Pyrolytic ZrO_2	2000	Si, Al	Dry N_2
6. Husted, Gruss and Mackus (1971) [4]	$1.4x10^{17}$ (Rm.T)				Ionized Gas Ionized ZrO_2	6000	Zr, Al	Ambient <30% RH
7. Green, Wickersham and Zilko (1976) [9]	10^4-10^6(350-5)	>0-19		Electronic and Ionic	Sputtered YSZ, oxygen deficient	1000-5000	Pt, Ag or Au	-
8. Balog Schieber, Michman and Patai (1977) [12]	$1.7x10^{15}$-$8.4x10^{16}$		F^2 F^2-6, 3.4	SCLC	CVD ZrO_2	1850	Al, Si-Al	-

CHAPTER III

EXPERIMENTAL PROCEDURE

In this chapter, the various equipment, electrical circuits and experimental procedures used during the course of this study are described. First, the preparation of the evaporant material is presented followed by a description of the thin film deposition facility, vacuum equipment, electron-beam evaporation, thickness and rate monitoring equipment, and the actual deposition process used in the evaporation of the Mo-ZrO_2-Mo structures. Also included is a discussion of the preparation of YSZ films by multilayer deposition. X-ray diffraction (XRD) and scanning electron microscope (SEM) techniques used in studying the structural properties of the films are detailed. Finally, the vacuum equipment for the measurement of the ac and dc properties is described along with the electrical circuits and procedures for measuring the ac and dc properties. The procedure for conducting the impedance spectroscopy studies are also described.

3.1 Evaporant Preparation

The metal evaporants used were as-received bulk metal, but the dielectric evaporants had to be prepared from powders. Three different methods were used in preparing the ZrO_2 evaporant: slip casting, dry pressing and skull melting. The Y_2O_3 evaporant was prepared by dry pressing. Initially, the ZrO_2 evaporants were slip cast or dry pressed,

but neither method densified the sources sufficiently to allow well-controlled evaporation. Such non-uniform evaporation produced films with poor electrical properties. Low density ZrO_2 evaporants were unsatisfactory because the films deposited were rather thick ($\sim$ 2 μm), and the E-beam drilled through the evaporant before the completion of the deposition.

Skull melting provided the required high-density ZrO_2 material, while dry pressing was unsatisfactory for the Y_2O_3 evaporant. Even though slip casting and dry pressing of ZrO_2 were not continued further, the methods will be described since they are adequate for thinner ZrO_2 deposits.

3.1.1 Slip Cast Evaporant

A good casting slip was prepared by stirring about 100 g of ZrO_2 powder (Fisher Scientific Co., Z-83, 99.5% pure) with 30 cc of distilled water in a clean beaker into a slurry. Chunks of ZrO_2 2.54 cm by 1.92 cm by 1.27 cm were made by casting the slurry in plaster molds while vibrating the molds. On casting solid, the chunks were dried in ambient air overnight, covered to protect them from dust. They were heated slowly to 1400 °C and soaked for 12 hours.

3.1.2 Dry Pressing

The Fisher Z-83 powder was pressed to 4000 psi in a 1.9 cm diameter steel die. No lubricant was needed and the volume was reduced to about half by pressing. A 1.9 cm pellet was pressed and trimmed to fit the evaporation hearth. The surface of the pellets were cleaned by scraping with a knife.

Y_2O_3 powder, 99.99% pure, supplied by Molycorp, Louvier, Co, did

not press easily and tended to freeze the die punches in the die cylinders. A pressing pressure of about 2000 psi in conjunction with an acetone-stearic acid solution lubricant was required to form pellets of good structural intergrity. The pellets were similarly trimmed and cleaned as for ZrO_2.

3.1.3 Skull Melting

All the ZrO_2 evaporants for the films described in this work were prepared by this method. Powdered ZrO_2 (Magnesium Electron Inc. New Jersey, grade G-60, 99% pure) was melted and solidified in a 7.6 cm diameter-water cooled skull, using a 50 KV, 2 MHz induction generator. The ZrO_2 boule was polycrystalline and almost theoretically dense. Blocks 1.27 cm x 1.27 cm x 1.9 cm were cut from the boule with a diamond saw, washed, and dried at 400 °C to provide the evaporants.

3.2 Thin Film Deposition

3.2.1 Thin Film Deposition Facilities

The thin film deposition facility shown in Figure 21, included a diffusion pumped system, deposition rate/thickness controller, E-beam power supply and deposition rate recorder. The vacuum chamber consisted of a pyrex bell jar 30 cm OD by 30 cm in height resting on an 18 cm tall aluminum collar. The aluminum collar served as a heat sink and rested on a vacuum feedthrough collar.

The feedthrough collar rested on an aluminum base plate and was sealed with a rubber O-ring. Neoprene gaskets served as seals between the bell jar and the aluminum collars. An oxygen leak valve provided

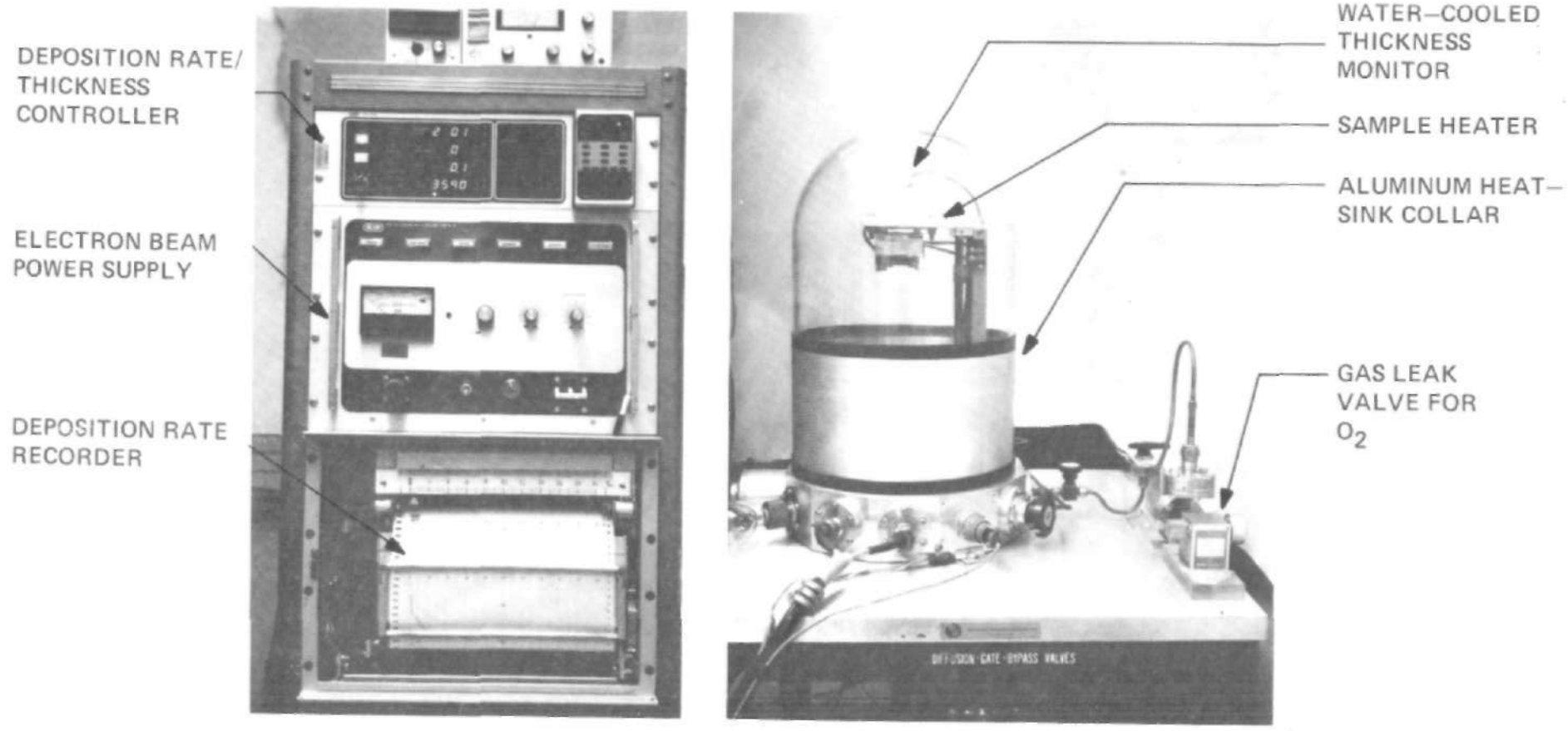


Fig. 21 Thin Film Deposition Facilities

atmosphere control. The system was normally vented with dry nitrogen to provide for more rapid cooling and to reduce water vapor adsorption, thus allowing faster pump down. The chamber was evacuated with a six-inch (15 cm) oil diffusion pump (1400 L/s) backed by a 500 L/min mechanical pump. Pressure was monitored with two thermocouple gauges and an ionization gauge.

A multihearth E-beam gun mounted in the center of the vacuum chamber provided deposition power. The multihearth gun was a six KW, self-accelerating, 180 bent-beam gun with four individual hearths. Each of the four water-cooled hearths was capable of holding 3.2 cc of evaporant material, and could be mechanically rotated from outside the vacuum chamber. An external rotating permanent magnet provided movement of the beam in the hearth orthogonal to the axis of the power supply beam position controller. The voltage of the electron gun was fixed at 10 KV so power was monitored by electron beam current.

The substrate heater/holder assembly can be seen in Figure 22, and the gun and other internal parts of the vacuum chamber are sketched in Figure 23. The substrate heater/holder (5 cm on a side) was constructed from stainless steel blocks. A 0.13 mm thick tantalum strip heating element, approximately 1.5 cm by 25 cm, was used to heat the stainless steel substrate holder assembly. Beryllia substrates served to electrically insulate the element from the steel assembly, and a copper block served as a heat sink from the heating element to the substrate holder. The substrate holder was a copper block with a recess to support the substrate to provide an exposed deposition area of 2.5 cm by 2.5 cm. The substrate holder was positioned in a slot in the heat

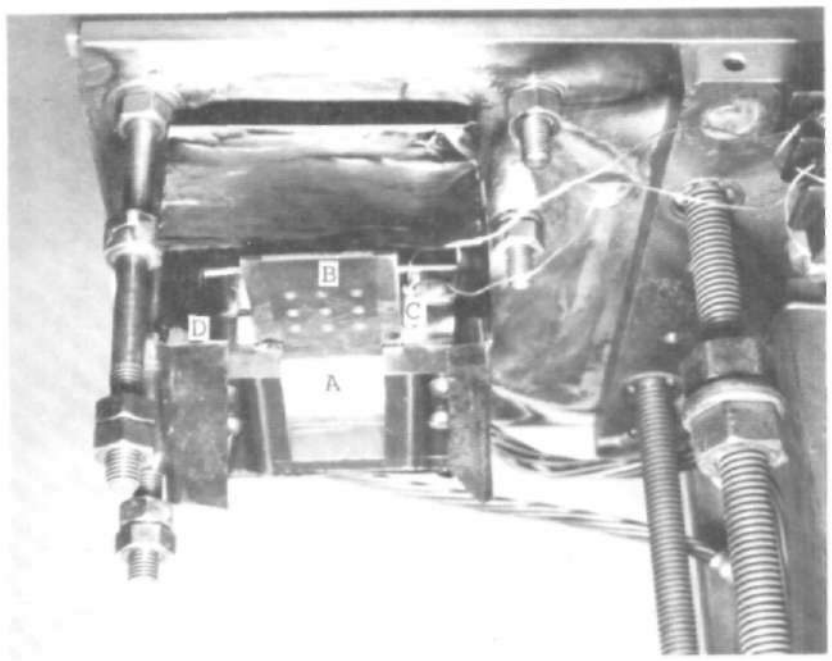


Fig. 22. Photograph of the Substrate Holder Assembly Prior to Deposition, Showing:

A. The Substrate
B. The Mask Plate
C. The Thermocouple
D. The Heater Block

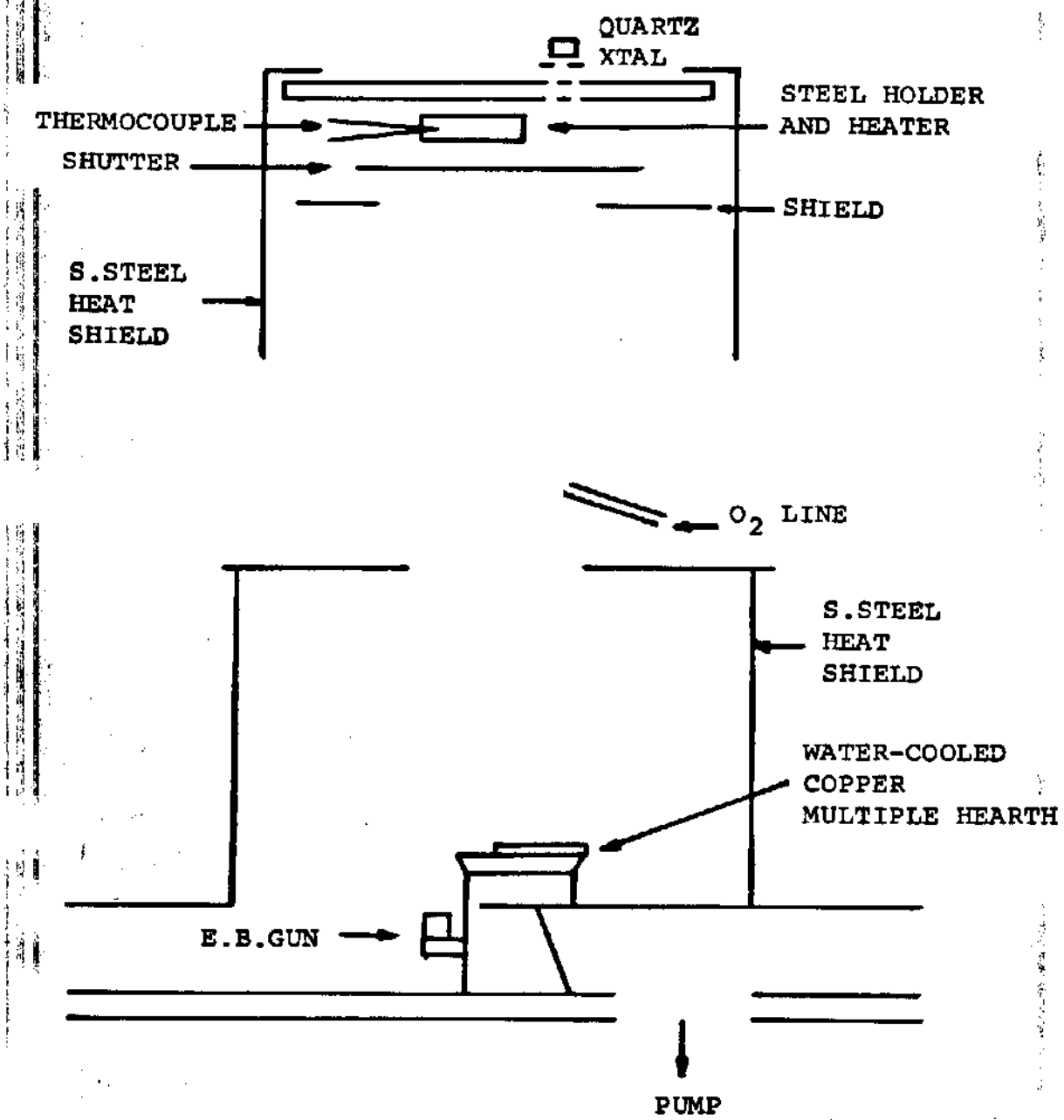


Fig. 23. Schematic Diagram of E-Beam Evaporation.

shell during the deposition as shown in Figure 22. A stainless steel mask containing nine holes, each of 0.25 cm diameter, was provided for masking the substrate during deposition. A Chromel/Alumel thermocouple was pressed to contact the bottom of a hole drilled 2 cm into the holder. The entire heater/holder assembly was electrically insulated from the support tower by porcelain insulators.

Power was supplied to the substrate heater through a step down, 60 A transformer controlled by a 10 A autotransformer, and a digital thermocouple temperature readout was used to monitor substrate temperature. The maximum autotransformer setting could produce 150 watts of power to the heating element, resulting in an approximate substrate temperature of 700 °C. The reproducibility of the substrate temperature at the same power setting was $\pm$ 20 °C; the main temperature error was judged to be the degree of contact between the thermocouple and the sample block, and the sample and heat sink blocks. The displayed temperature decreased 40 °C during the deposition due to radiation losses from the unshielded substrate.

Thickness and deposition rate were controlled by a Sloan Model MDC 9000 thin-film deposition controller, a microprocessor-based instrument. The controller provided thickness and rate control by changing beam power as a result of feedback from a piezoelectric crystal monitor. A fast-response strip chart recorder was used to monitor the deposition rate.

3.2.2 Thin Film Deposition Procedure

In this section, the procedure for the actual deposition of the thin films is described. Deposition of the Mo-ZrO_2-Mo structures is described first followed by preparation of the YSZ films by multilayer deposition.

3.2.2.1 Deposition of Mo-ZrO_2-Mo Structures

A typical deposition of Mo-ZrO_2-Mo structures was conducted in the following manner. Predeposition procedures involved cleaning various components and assembling them in the vacuum chamber. Any metal deposits on the steel shields and plates, substrate holder, and mask were removed with 600 grit SiC grinding paper. Deposits on the pyrex bell jar were removed by wiping with lint free tissue wetted with acetone. The various parts were then washed with soap and warm water, rinsed with water, acetone and methanol in that order and then placed in a dust-free chamber to dry. The glazed Al_2O_3 substrate, supplied by the Technical Ceramic Products Division of 3M Corporation, was washed with soap and warm water, rinsed with water and ultrasonically vibrated in acetone for $\sim$ 5 minutes. The substrate, steel mask and substrate holder were vapor degreased with trichloroethelene (TCE). Molybdenum and ZrO_2 evaporants were placed in the hearths and a quartz crystal was placed in the thickness/rate sensor head. The cleaned parts were assembled, with the mask positioned so as to protrude about 6 mm into the deposition area. A movable deposition shield was positioned between the evaporant and the substrate. The chamber was pumped down with the mechanical pump to $\sim$ 50 torr, and the diffusion pump further reduced the pressure to the range of 10^{-6} torr, usually overnight.

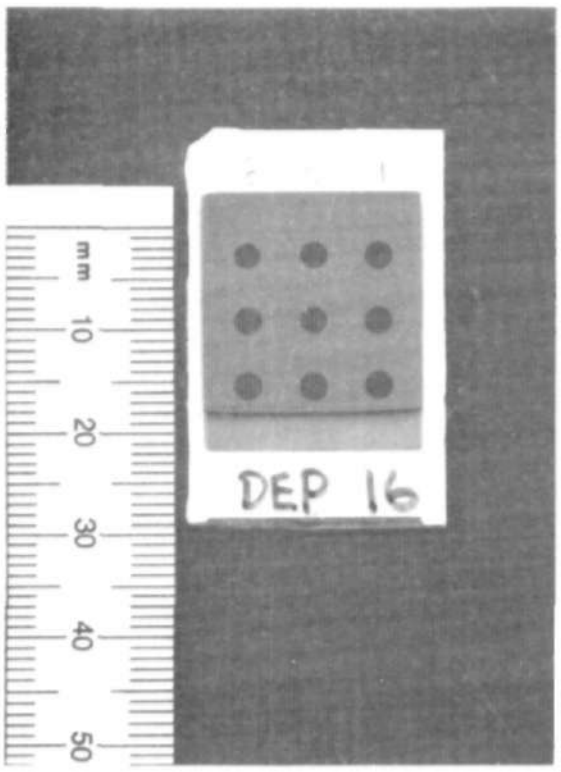
The substrate was heated prior to evaporation, which required two hours for temperatures above 400 °C. The molybdenum evaporant was positioned for evaporation, the beam sweep was set on minimum (because metals are conductive and distribute the heat well), and the MDC contoller was started in the automatic mode. Programs for the different evaporants, specifying set-up conditions such as rise time, soak time, rate etc. are tabulated in Appendix B. During the rise time, the controller linearly ramped the power up to the specified soak power, and then held it constant during the soak time. Deposition of the evaporant followed the soaking period. During deposition, the rate was controlled by the controller and the substrate shield was opened as soon as a stable rate was attained. The beam current for molybdenum evaporation was usually 180 mA, corresponding to 1800 watts. Once the required thickness (usually 3000 Å), was deposited, the shield was closed and the controller power was programmed to zero in 30 seconds. After molybdenum deposition, the substrate mask was pushed 3 mm into the deposition area. This allowed the insulator to be formed on the molybdenum (or other lower electrode), and exposed a 3 mm strip for electrical contact to the bottom electrode.

For ZrO_2 deposition oxygen was introduced into the chamber and monitored at a pressure of 10^{-4} torr. The beam sweep was set to maximum to distribute the heat. More heat distribution was afforded by using a rotating external magnet (slighly eliptical in cross section) which rotated the beam around the hearth. Again, the MDC controller was started and the evaporation conducted as described above. During ZrO_2 deposition, the beam had to be moved from back to front in the hearth to

prevent drilling, since material flow was minimal. On moving the beam to a new position, the material would initially outgas, causing pressure and rate surges, so such changes had to be made very gradually. The current needed for ZrO_2 evaporation was usually about 70 mA. Most of the films deposited were about 20,000 Å thick.

After the ZrO_2 deposit, the substrate mask was pushed all the way into the deposition area so that dots (top electrodes) of molybdenum could be deposited. The hearth was rotated to molybdenum, oxygen leak was stopped and a top molybnenum electrode was deposited as described earlier. The vacuum chamber was allowed to cool after this final deposit, usually overnight, vented with nitrogen and dismantled. The Mo-ZrO_2-Mo structure was stored in a desiccator until needed. A typical Mo-ZrO_2-Mo sample is depicted in Figure 24(a). The nine capacitors were designated as shown schematically in Figure 24(b). The various deposition conditions such as pressure, rate, and temperature used in the deposition of the ZrO_2 films are surmarized in Table 4.

(a)



(b)

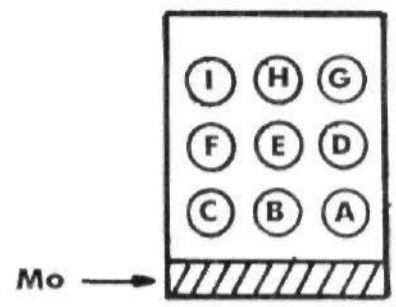


Fig. 24. Thin Film Samples (a) Photograph (b) Sketch Showing the Designation of Individual Capacitors.

Table 4. Thin Film Deposition Conditions

Sample	Depositn. Temp(C)	Beam Current (mA)	Oxygen Pressure (10^{-5} torr)	Rate A/s.	Program Thickness (μm)	SEM Thickness (μm)
Z5	488	80	5.0	5.0	0.50	-
Z6	475	80	5.0	5.0	0.35	-
Z7	225	100	6.0	5.0	0.38	1.556
Z8	480	70	7.0	5.0	0.50	1.978
Z9	190	70	3.5	5.0	0.5	-
Z11	200	90	5.0	5.0	0.5	-
Z12	350	100	4.0	5.0	0.5	2.000
Z13	400	80	4.0	5.0	0.5	2.148
Z14	300	80	3.0	5.0	0.5	2.037
Z15	450	70	5.5	5.0	0.5	1.963
Z16	510	80	30.	5.0	0.5	1.74
Z17	600	70	5.0	5.0	0.5	-
Z18	470	40	1.5	5.0	0.5	-
Z19	480	70	5.0	5.0	0.5	-
Pt/Rh	490	185	0.7	2.0	0.1	-
Pt,YZ20	498	90	6.0	5.0		
Mo,YZ21	490	90	6.0	5.0		

* Program thickness implies the actual thickness entered into the MDC 9000 program

3.2.2.2 Preparation of YSZ Films

It was thought that by bringing Y_2O_3 and ZrO_2 sufficiently close together in a multilayer film, the components would diffuse and react at a high temperature to form the cubic stabilized structure. Since the individual oxide layers could be kept thin, the diffusion lenghths would be small, smaller, infact, than those typically encountered in the preparation of bulk YSZ.

To provide sufficient Y_2O_3 for stabilization and still keep the diffusion paths small, five layers of the oxides were deposited according to the thicknesses indicated in Figure 25. These thicknesses were calculated to provide a 10 mole percent Y_2O_3-stabilized ZrO_2 upon

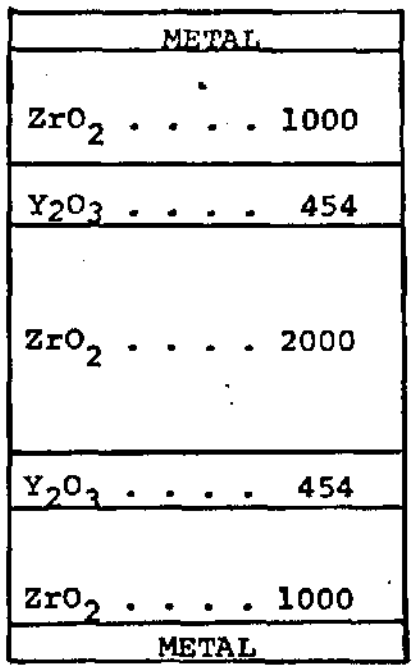


Fig. 25. Sketch of Oxide Layers in Multilayer Deposition, Showing Thickness in Å.

total reaction. A Pt/Rh-Y_2O_3,ZrO_2-Pt/Rh and a Mo-Y_2O_3,ZrO_2-Mo sample were prepared as described for Mo-ZrO_2-Mo samples, except that the ZrO_2 was replaced by the five oxide layers in Figure 25. The deposition program for molybdenum and ZrO_2 were identical as above and the programs for Y_2O_3 and Pt/Rh are also recorded in Appendix B. The oxides were deposited in oxygen while the metals were deposited without it.

The Pt/Rh-Y_2O_3,ZrO_2-Pt/Rh samples were heated in air to 800 °C for five hours and 1200 °C for nine hours. The Mo-Y_2O_3,ZrO_2-Mo samples were heated to 1200 °C in an induction furnace with N_2 atmosphere for seven hours. The top Pt/Rh elecrode of the Pt/Rh-Y_2O_3,ZrO_2-Pt/Rh samples was found to be non-conductive after the 1200 °C heating. Upon etching a strip of the heat-treated Pt/Rh-Y_2O_3,ZrO_2-Pt/Rh in phosphoric acid at 200 °C for 30 minutes, the lower Pt/Rh electrode was exposed and found to be conductive. Upper electrode dots of Au/Pd were sputtered on the unetched portions of the Pt/Rh-Y_2O_3,ZrO_2-Pt/Rh using the substrate mask in such a way that the Au/Pd dots were formed on the portions where Pt/Rh had not been deposited.

3.3 Crystal and Physical Structure

The crystal structure of the ZrO_2 films were determined with a Philips X-ray diffractometer, using Cu K_α radiation, a voltage of 45 KV, and a current of 25 mA. The diffractometer was generally scanned at one or one-half degree 2θ per minute, using a time constant of 1.0 and 3.0 respectively. For broadening and intensity measurements, a scanning rate of one-eighth degree 2θ/min and time constant of 10 were used. The intensities were integrated peak intensities with the background

substracted, whereas broadening was the peak breadth at half height. The crystallite size, t, for crystallites with the $(11\bar{1})$ and (111) monoclinic ZrO_2 planes parallel to the surface of the films were calculated with the X-ray line broadening equation [64]

$$t = \lambda/\beta' \text{ Cos } \Theta \text{ ,} \qquad (56)$$

where λ is the X-ray wavelength (Å), β' is the intrinsic broadening (in $^\circ 2\Theta$) and is the Bragg angle for the reflections. The intrinsic broadening was obtained from the experimental values by the Jones' correction method [65] using strain-free (vapor-grown) 3μm particle size rutile to measure instrumental broadening. The films were assumed to be strain-free. For two samples, the texture was studied by generating pole figures for the $(11\bar{1})$ and (111) monoclinic ZrO reflections, scanning between angles of 90° and 33°. A pole figure device of the Engineering Experiment Station of this institute was used. It consisted of a General Electric diffractometer with a modified quarter circle goniostat with a pole figure stage and a microcomputer axis controller.

To observe grain size and measure film thickness, the samples were fractured perpendicular to the substrate surface and examined in a SEM. The thickness of the films was measured from the electron micrographs.

3.4 Measurement of Electrical Properties

The investigation of the electrical properties of the capacitor samples was conducted in a vacuum chamber to avoid surface conduction and other effects of the ambient gases and vapors, especially moisture. For the same reason, samples were heated to 200 °C and cooled before measurements were made.Most ac measurements were made with rather high signal voltages (∿ 8 V rms), which was possible because of the low losses of those films. However, the oxygen deficient ZrO_2 film and the Pt/Rh-Y_2O_3,ZrO_2-Pt/Rh films had high losses (tan δ >0.4), which were not measurable on the bridge used without a preceeding amplifier. For these high-loss films, impedance spectroscopy and low signal voltages (100 mV rms) were applied.

3.4.1 Vacuum System for Electrical Measurements

Figure 26 is a photograph of the interior of the vacuum system with the bell jar removed. The vacuum chamber consisted of a bell jar 22 cm ID by 20 cm high resting on an Aluminum feedthrough collar 20 cm ID and 18 cm high which in turn, rested on a brass plate. Neoprene gaskets served as seals between the bell jar and the aluminum collar and between the collar and the brass plate. The system was pumped down with a two inch diameter (90 L/s) diffusion pump backed by a 160 L/min. Duo Seal mechanical pump. Pumping was accomplished as described for the electron-beam vacuum system. Pressures lower than 10^{-4} torr were obtained.

A resistance heated copper furnace mounted on a microscope stage in the vacuum chamber served as electrical measurement chamber. This furnace is sketched in Figure 27, which shows a Mo-ZrO_2-Mo sample

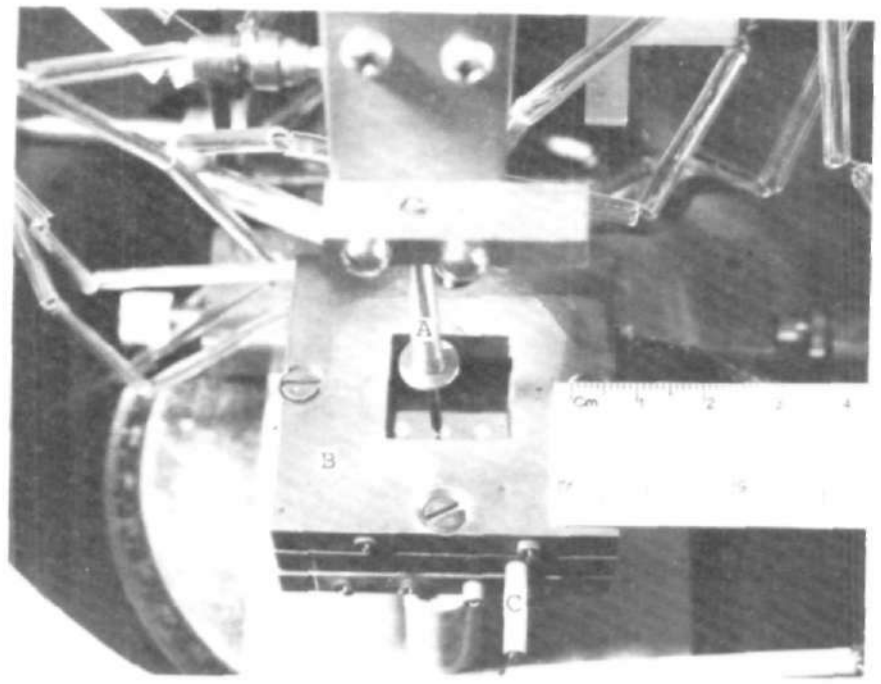


Fig. 26. Photograph of the Electrical Test Apparatus Showing:

A. Spring Loaded Top-Electrode Probe

B. Copper Furnace

C. Bottom Electrode

positioned for measurement, bottom and top electrical contacts to the molybdenum electrodes, an Iron-Constantine thermocouple and a qaurtz plate heat shield. The copper furnace had external dimensions of 5 cm by 5 cm by 2 cm. Both electrical contacts were spring loaded and the upper contact could be moved in the vertical direction. The microscope stage could be moved in two perpendicular horizontal directions, using mechanical motion feedthroughs, and allowed the measurement of all nine capacitors on a sample without breaking the vacuum.

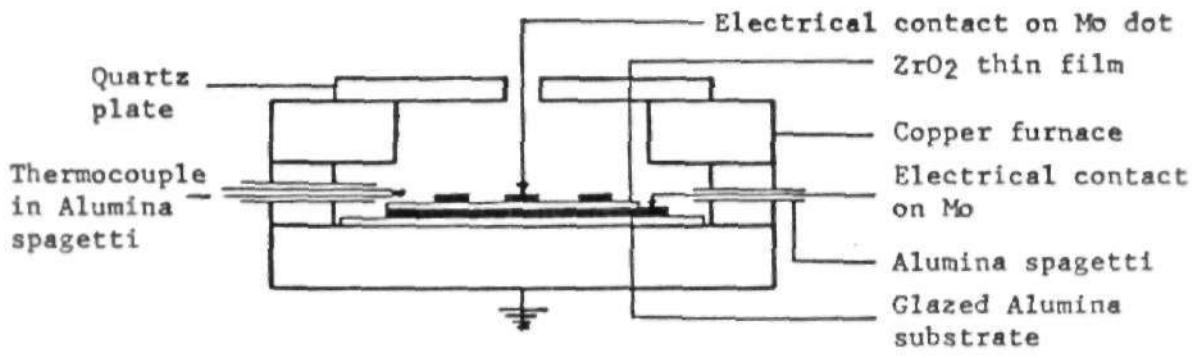


Fig. 27. Copper Furnace for Electrical Measurements (Schematic).

The copper furnace was grounded and heated with a 24 gauge wire, 70 cm long, insulated with Al_2O_3 spagetti through the top and bottom blocks of the copper furnace in a manner that minimized inductive effects. Chromel wire was used initially, but had a tendency to short to the furnace, probably due to pyrolysis of vacuum oil and deposition of carbon on the Al_2O_3 insulators. The insulators then had to be oxidized and the wires rewound. It was suspected that the chromium catalysed the pyrolysis reaction, so stainless steel wiring was used later, with much success. The heater wires were extended with copper wires. All of the electrical wiring, the thermocouple, heater coil, and electrical contact extensions were insulated from the parts of the vacuum chamber with Al_2O_3 insulation tubing. Power to the heater coil was provided by an Omega Engineering Model 22 proportional-band temperature controller, operating through an autotransformer. An iron-constantine thermocouple served to provide temperature feedback to the controller. Temperature was monitored with a Doric Trendicator,

Model 400 A, Type J/F, digital temperature readout. Temperatures were equilibrated for at least five minutes before measurement and controlled to within 1°C during the entire duration of the measurement. The vacuum chamber was shielded from external electric fields with a wire mesh cover.

3.4.2 Ac Measurements

The capacitance and loss tangent of the films were measured with a General Radio capacitance bridge, Type 716C; a Hewlett-Packard Model 2000 CD wide-range oscillator; and a Tektronix, Type 565 dual-beam oscilloscope as the detector. A sample signal voltage of $\sim$8 V rms was used, corresponding to a field of 0.04 MV/cm. Parallel model capacitance C_p was measured and the measurement was conducted as a function of frequency (60 Hz-50 KHz) and temperature (25°-325°C). The calculation of the various electrical properties from C_p and tan δ were presented in Section 2.2.1.1. A computer program, ACPROP, given in Appendix C, was written to calculate and plot from these measurements: real and imaginary permittivity as a function of frequency and temperature, real and imaginary dielectric constant as a function of frequency at two temperatures, dielectric conductivity as a function of frequency at two temperatures, Cole-Cole plots, and the product of 1000 Hz dielectric conductivity and temperature as a function of reciprocal temperature. The program could also perform a linear regression analysis on any segment of all the plots except the permittivity and Cole-Cole plots.

3.4.3 Dc Measurements

The dc measurements included current-voltage (I-V), and current-temperature (Arrhenius) characteristics, and charge storage. All the measurements were conducted with the circuit diagrammed in Figure 28. For the I-V and Arrhenius characteristics, the double pole, single throw, switch, S, in Figure 28 was connected to A. Voltage was measured with a Hewlett-Packard multimeter, Model 3469A, and was applied by the Lamda Electronics regulated power supply, Model 71. Current was

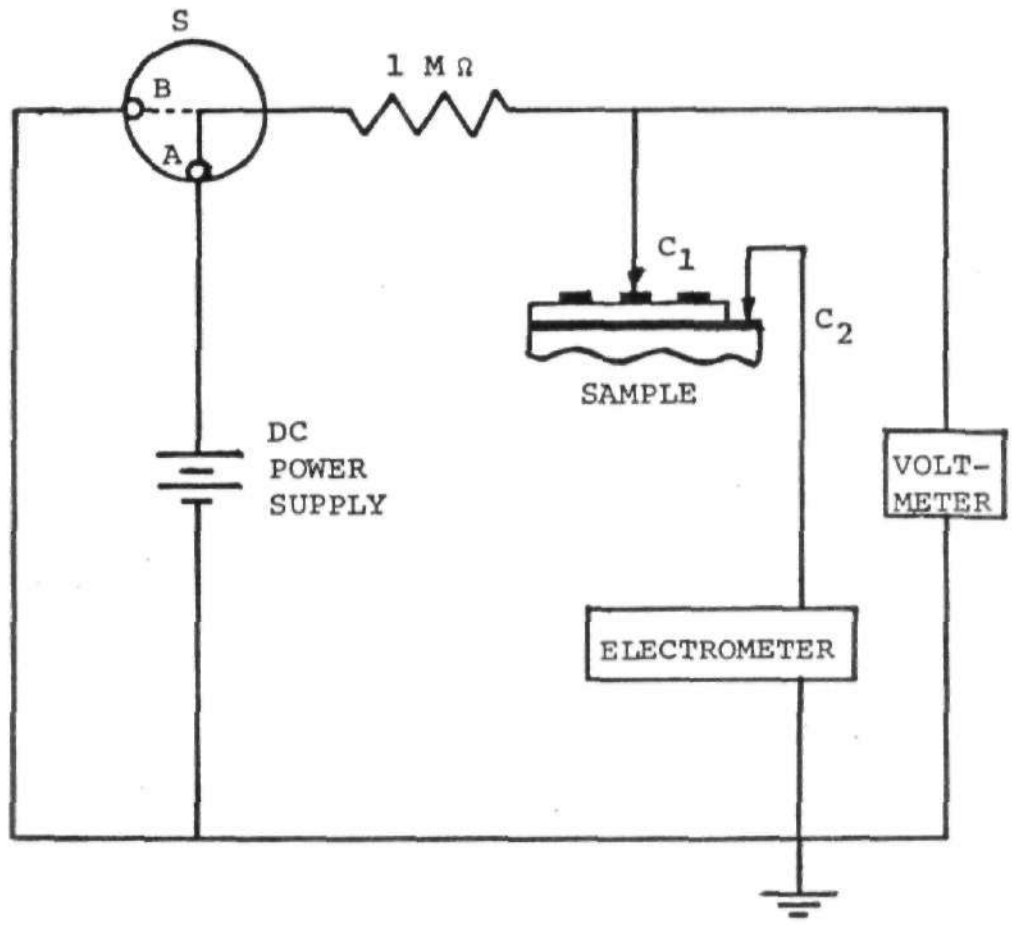


Fig. 28. Circuit for Dc Measurements

measured with a Keithley solid state electrometer, Model 610 C. Voltages up to 225 V were used for the I-V characteristics, and temperatures between 25°C and 350°C were used for the current-temperature measurements. Top electrode (dot) positive and dot negative measurements were made by interchanging the electrical contacts C1 and C2 in Figure 28.

Charge storage measurements were made by first charging the samples at a given voltage and temperature for about 30 minutes, with switch S in Figure 28 connected to terminal A, and then discharging the sample through the 1 M Ω resistor with switch S shorted to ground (connected to terminal B). Charge storage was measured with the Keithley electrometer. The meter was zeroed on the coulombs scale before every measurement. The discharge was also recorded on a recorder and the charge storage was determined only when the voltage was practically constant. This usually required about 10 minutes of discharging. Both dot positive and dot negative charge storage measurements were made for samples Z14B and Z15E as a function of charging voltage. Temperatures of 25°, 60° and 90°C were used.

A computer program, DC4, (given in Appendix D) was written to plot either dc conductivity or the product of dc conductivity and temperature vs. reciprocal temperature. The program could perform a linear regression analysis on any segment of these plots and could also perform a Poole-Frenkel or Schottky analysis on the results.

3.4.4 Impedance Spectroscopy

The circuit for the admittance measurements is shown in Figure 29(a). A Princeton Applied Research lock-in amplifier, Model 5101, with a signal imput impedance of 10 MΩ was used for measuring the admittance of the samples. The ouput of a Hewlett-Packard, Model 200CD wide-range oscillator was applied to a 500Ω potentiometer, from which the 1 V rms reference voltage for the lock-in amplifier and a sample voltage of 100 mV rms were supplied, as shown in Figure 29(a). To determine admittance with this lock-in amplifier, either the phase and magnitude of the voltages are measured, or the real part (V_x) and the imaginary part (V_y) of the voltages are measured at 0° and 90° phase angles respectively. The latter method was used in this work. V_y and the resistor voltage V_R in Figure 29(a) were measured by applying each to the signal channel and measuring the V_x and V_y components relative to the reference voltage. Then

$$V = V_x + jV_y \ , \tag{57}$$

where V was V_I or V_R. V_I and V_R were also monitored with a Fluke digital-readout multimeter (not shown in Figure 29(a)) with an input impedance of 10 MΩ. This input impedance was high enough not to introduce significant errors into the measurements. V_I was usually maintained at about 100 mV rms and V_R at about 5 mV rms by varying the potentiometer or the decade resistor box in Figure 29(a). This was done in order to keep the two voltages significantly different to minimize errors, but still measurable with sufficient accuracy. The admittance was calculated from

$$A = I/V = (V_R/R)/(V_I - V_R) \tag{58}$$

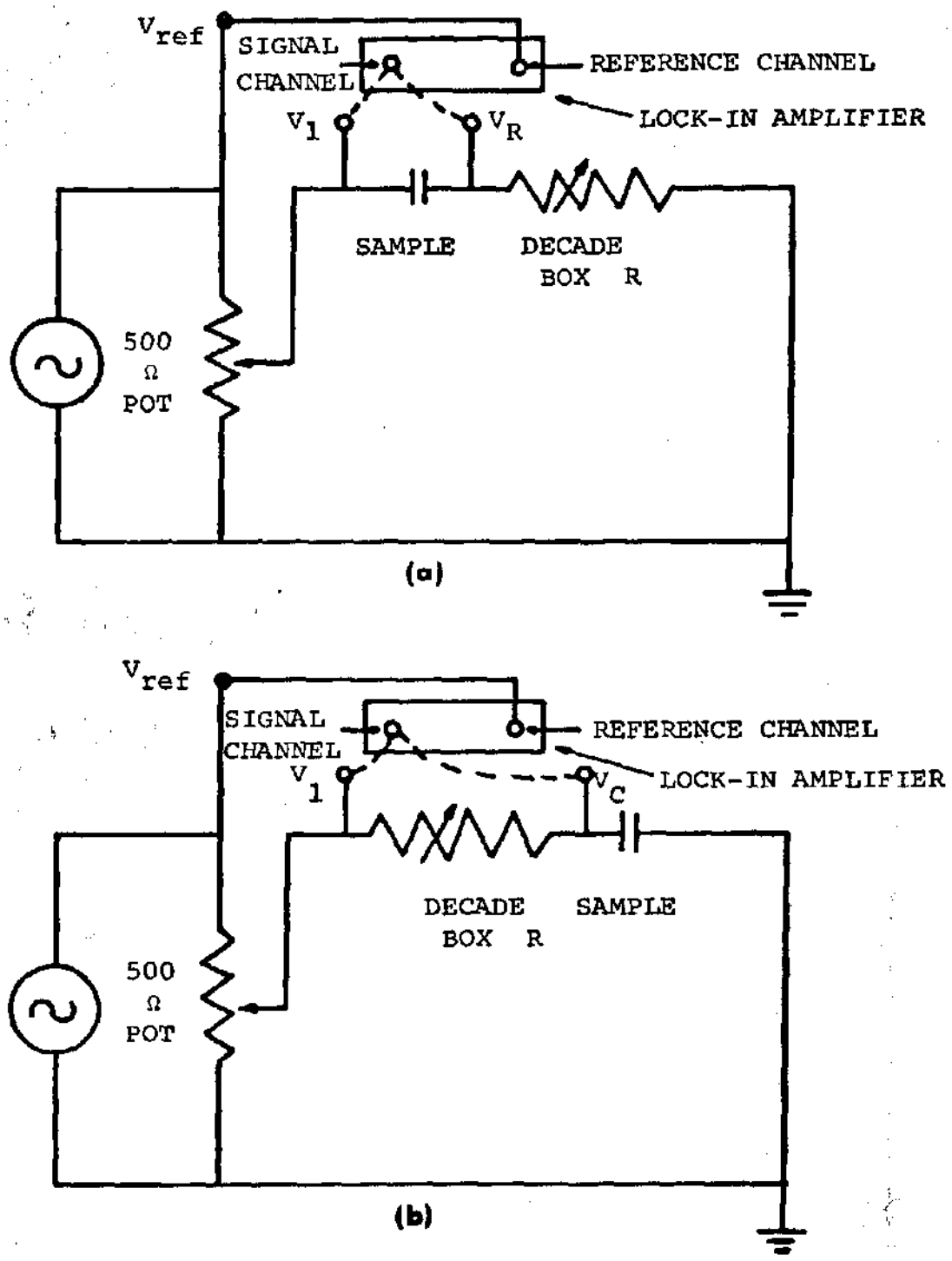


Fig. 29. Circuit for Admittance Measurements (a) for High Impedance (b) for Low Impedance.

The admittance was resolved into the form

$$A = G + jB \tag{59}$$

where G is the conductance and B is the susceptance.

The circuit of Figure 29(a) was used for the lower values of the loss. When the losses were large, the positions of the capacitor and the decade box in Figure 29(a) were interchanged, Figure 29(b). In this case, V_1 and the capacitor voltage V_c were measured and the admittance was calculated from

$$A = \frac{I}{V} = \frac{(V_1 - V_c)/R}{V_c} \tag{60}$$

The admittance measurements were made as a function of frequency from 5 Hz to 100 KHz, and B was plotted against G to obtain the admittance plot. In some cases temperature was also varied. A computer program, ADMIT, given in Appendix E was written to calculate the admittance and plot B as a function of G for several temperatures. The admittances obtained with the lock-in amplofier agreed with bridge measurements within 5% for the magnitude and $\pm$ 2° for the phase between 60 Hz. and 4kHz.

CHAPTER IV

RESULTS AND DISCUSSION

This chapter presents the results of this investigation. The results for the pure monoclinic ZrO_2 films are first presented, followed by the results for the Y_2O_3,ZrO_2 films. For both types of films, the structural characteristics, and ac and dc properties are discussed. Impedance spectroscopy studies on the films are also presented. In these discussions, comparisons are made to similar published work and attempts are made to deduce ac and dc conduction mechanisms.

4.1 ZrO_2 Films

4.1.1 Crystal and Physical Characteristics

All the ZrO_2 films were polycrystalline, with only the monoclinic phase present for deposition temperatures between 300 and 600 C. At lower temperatures (190°-200°C), however, the cubic phase was the major crystalline phase formed. X-ray patterns of films deposited at 200° 450° and 600°C, in the {111} region, are presented in Figure 30. This figure also includes the pattern for the source monoclinic ZrO_2 material for comparison. The patterns of cubic and tetragonal ZrO_2 are quite similar, but can be distinguished with the (400) cubic and (004) and (400) tetragonal peaks. Miller et al. [66] showed that the molar ratio of the cubic to the tetragonal ZrO_2 phases may be calculated from

$$\frac{M_F}{M_{T'}} = 0.88 \frac{I_F\ (400)}{I_{T'}\ (400) + I_{T'}\ (004)} \qquad (61)$$

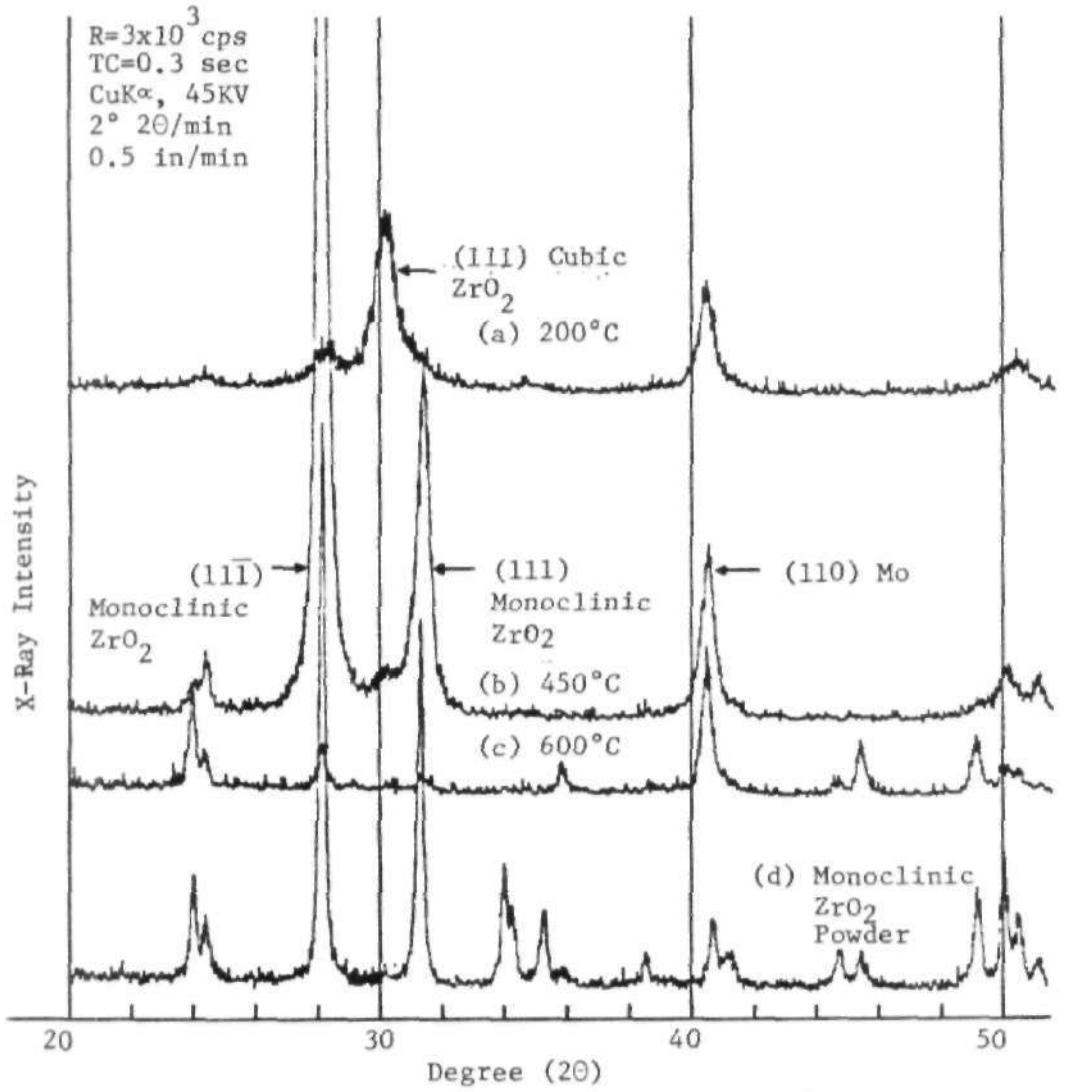


Fig. 30. X-ray Diffraction Patterns in the {111} Region for Evaporated ZrO_2 Thin Film, Deposited at (a) 200°C, (b) 450°C, (c) 600°C. Also Shown is the Pattern for Powder ZrO_2 Source Material (d).

where M stands for moles, subscripts F and T' stand for the cubic and tetragonal phases respectively and I_F and $I_{T'}$ is the intensity of the respective diffraction peaks. The X-ray patterns in the region of the (004) and (400) peaks for some of the samples are presented in Figure 31 to show the cubic (400) peaks at about 73.8° 2Θ and the positions of the tetragonal peaks. As can be seen, the (004) and (400) tetragonal peaks are not observable and therefore, the cubic phase is present to some degree in all the films. It is possible that some amorphous phase was present in the films, especially for those deposited at lower temperatures. However, the amount of the different phases could not be quantified because preferred orientation was observed. The ratios of the $(11\bar{1})$ and (111) monoclinic integrated peak intensitiies of the films to those of random orientation powder are plotted as a function of the deposition temperature in Figure 32. The ratio increased from 0.18 to 4.8 for the $(11\bar{1})$ and from zero to 2.1 for the (111) reflections as the deposition temperature increased from 190 °C to 510 °C. The $(11\bar{1})$ intensity ratios varied linearly with deposition temperature in this range and could be represented by

$$\frac{I_{sample}}{I_{powder}} = 0.149T - 2.714 \ , \qquad (62)$$

where T is deposition temperature in °C. However, the (111) intensity ratio increased less rapidly and tended to be levelling off at 510 °C. The intensity ratio greater than 1.0 indicated preferred orientation, especially for the samples deposited above 300 °C where the films were predominantly monoclinic. At lower temperatures, 200 °C, the films were

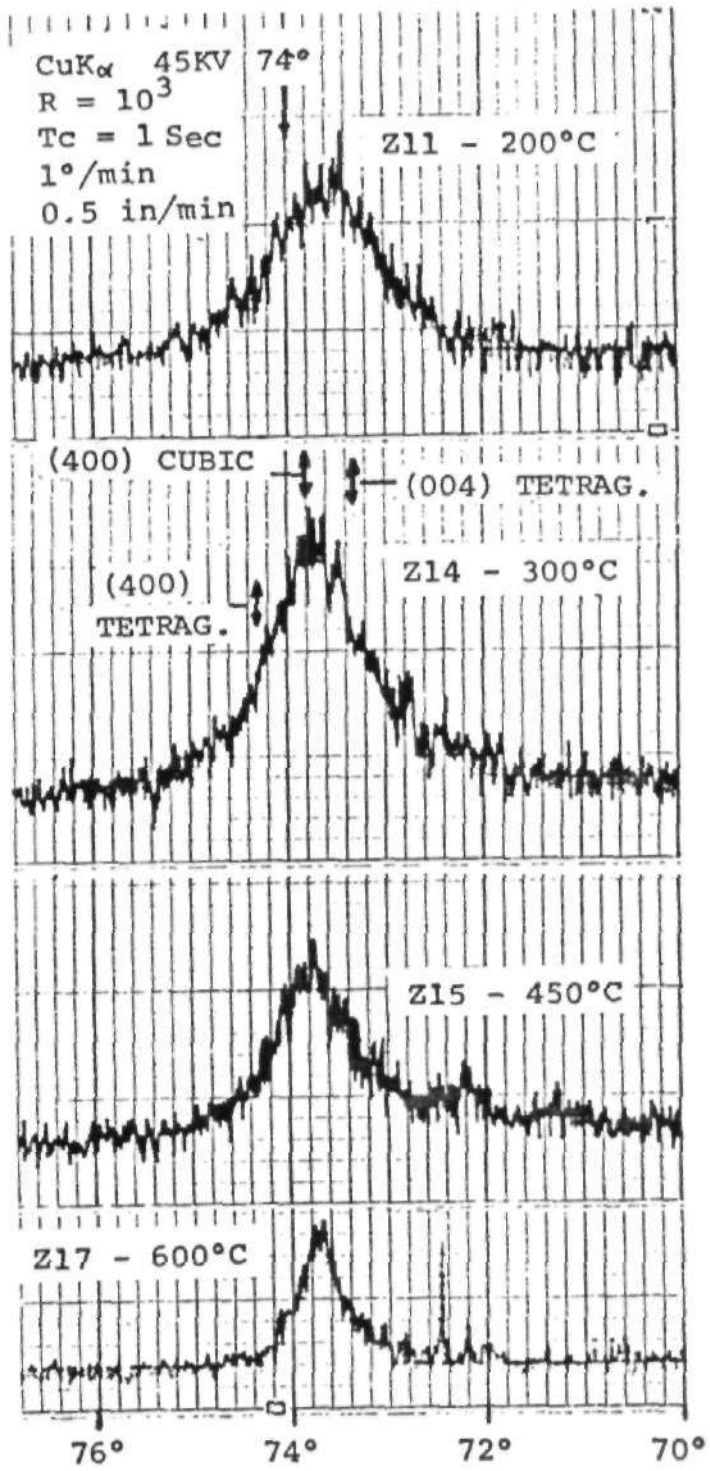


Fig. 31. X-ray Pattern in the {400} Region for ZrO_2 Films Deposited at Varying Temperatures.

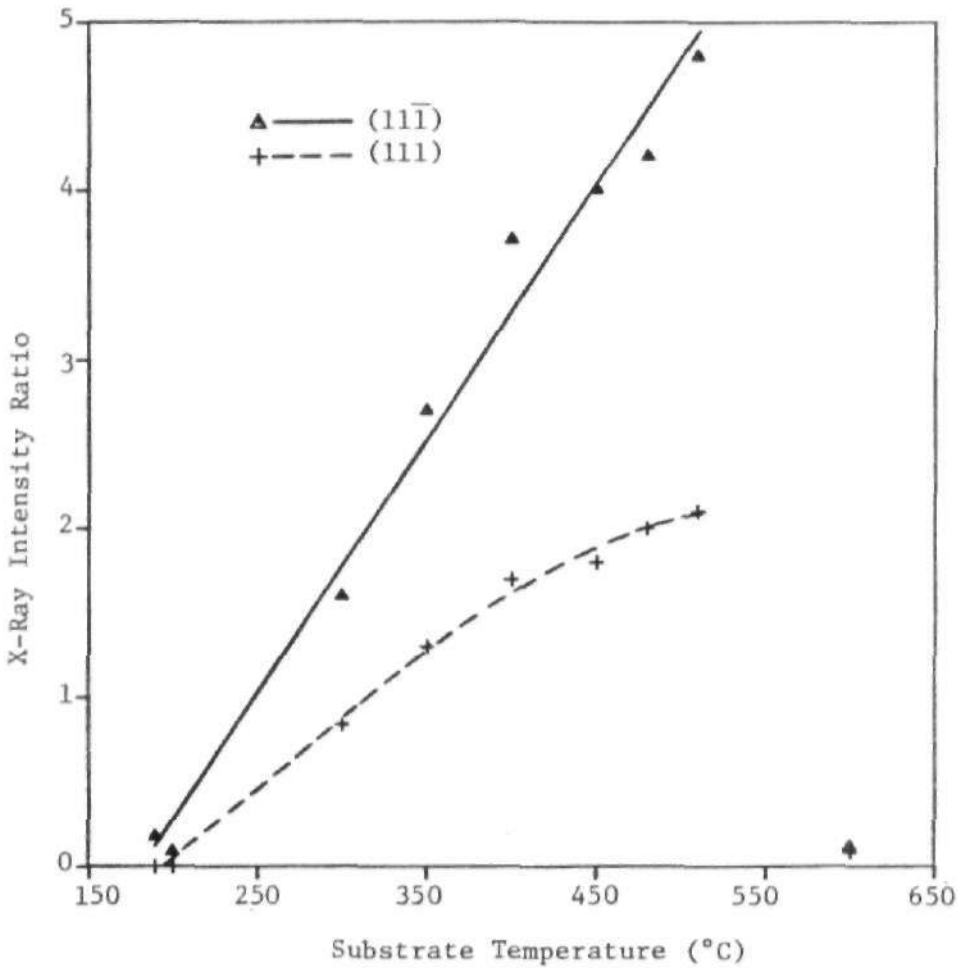


Fig. 32. Ratio of X-ray Intensities of Evaporated ZrO_2 Thin Film Sample to the ZrO_2 Powder Intensities for the (11$\bar{1}$) and (111) Reflections, as a Function of the Deposition Temperature.

mainly cubic with only a small monoclinic content. Therefore, the intensity ratio was less than 1.0 due to the reduced monoclinic content.

At a deposition temperature of 600 °C, the $(11\bar{1})$ and (111) intensity ratios decreased dramatically to almost zero. Preferred orientation most likely changed to other planes. Pole figures confirmed this change in preferred orientation. Figure 33 is the (111) monoclinic ZrO_2 pole figure for a sample deposited at 420 °C showing a slight fiber axis. However, the sample deposited at 510 °C shows a more pronounced $(11\bar{1})$ fiber axis in the $(11\bar{1})$ pole figure presented in Figure 34. This increased $(11\bar{1})$ fiber texture could be due to the increased mobility of the ZrO_2 molecules on the substrate surface with increased temperature. Such increased mobility favors a thermodynamically favored crystallite orientation to enhance preferred orientation.

The crystallite size of the monoclinic ZrO_2 films is plotted in Figure 35 as a function of deposition temperature. It increases from 118 Å to 484 Å for the $(11\bar{1})$ and from 175 Å to 265 Å for the (111) orientations, as deposition temperature increases from 190 ° to 600 °C. The crystallite size for the $(11\bar{1})$ orientations were generally larger and increased more rapidly with temperature than that for the (111) orientations. This indicates preferred crystallite growth in the direction perpendicular to the $(11\bar{1})$ planes.

A typical scanning electron micrograph of the films is shown in Figure 36. The molybdenum and ZrO_2 films are clearly distinguishable. The grain size could be measured in some, but not all of the films and it is doubtful if individual crystallites were visible. Some of the films showed columnar grains, which actually consisted of many

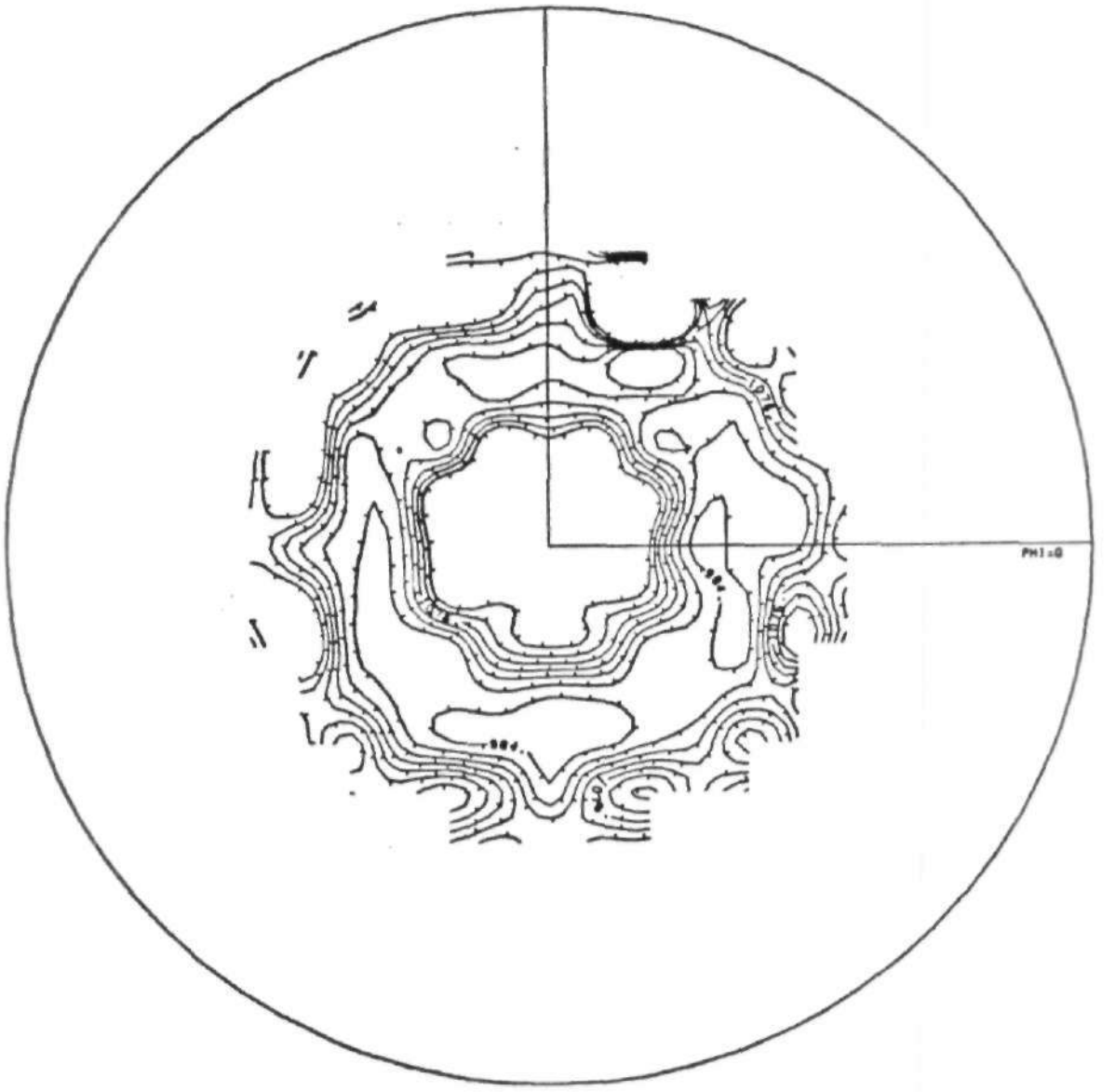


Fig. 33. $(11\bar{1})$ Pole Figure for ZrO_2 Thin Film, Sample Z4, Deposited at 420°C, Showing a $(11\bar{1})$ Fiber Axis.

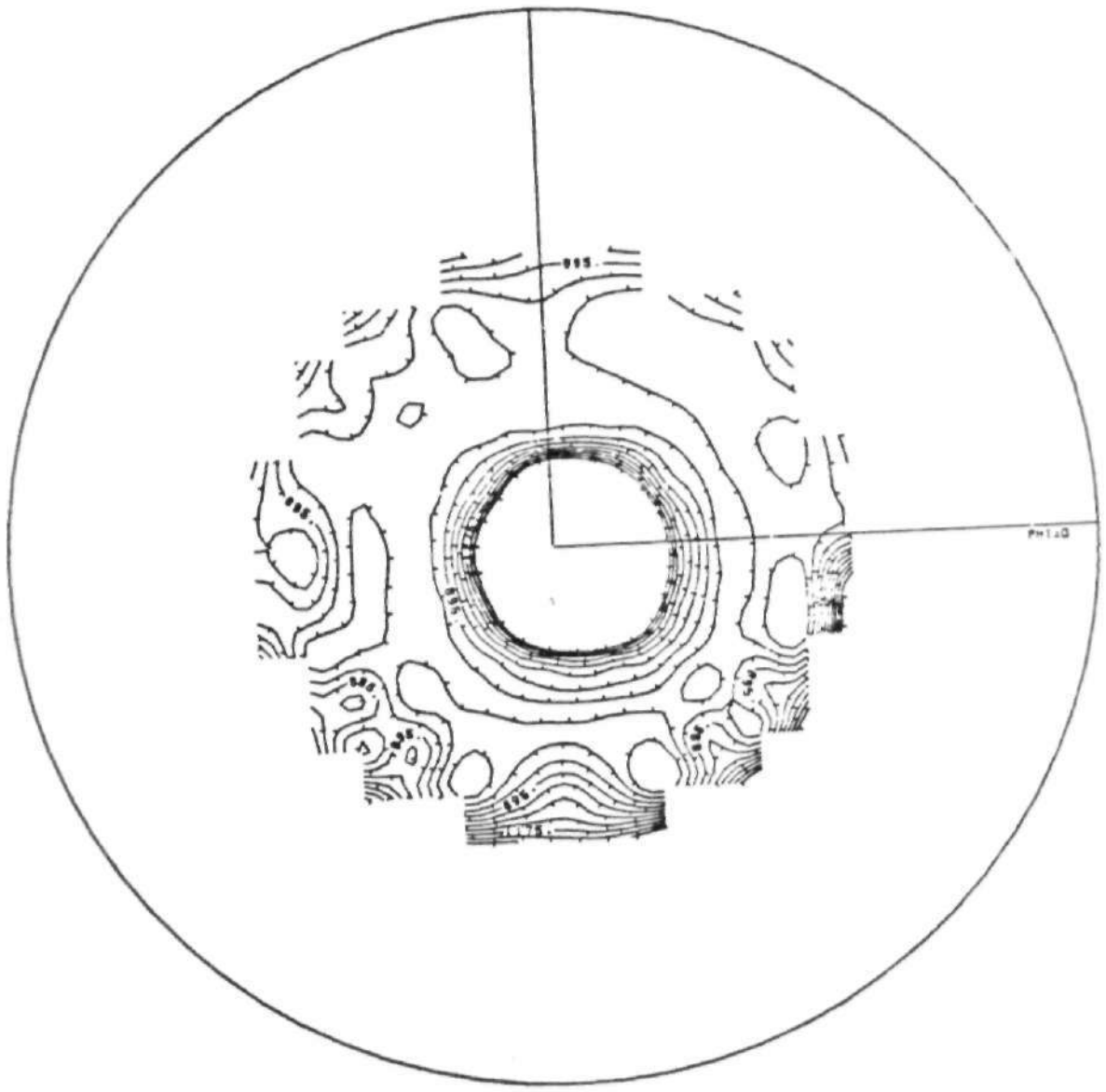


Fig. 34. $(11\bar{1})$ Pole Figure of ZrO_2 Thin Film, Sample Z16, Deposited at 510°C Showing a $(11\bar{1})$ Fiber Axis.

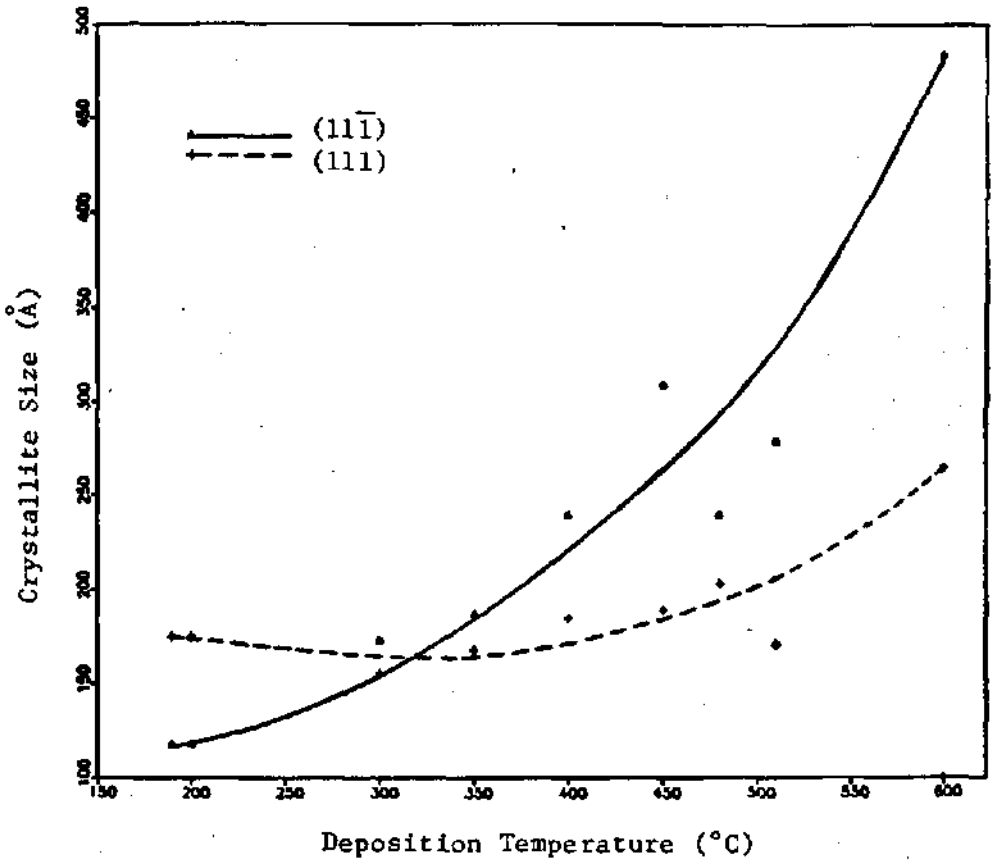


Fig. 35. Crystallite Size of Vapor Deposited ZrO_2 Thin Films for the (11$\bar{1}$) and (111) Orientations as a Function of Deposition Temperature.

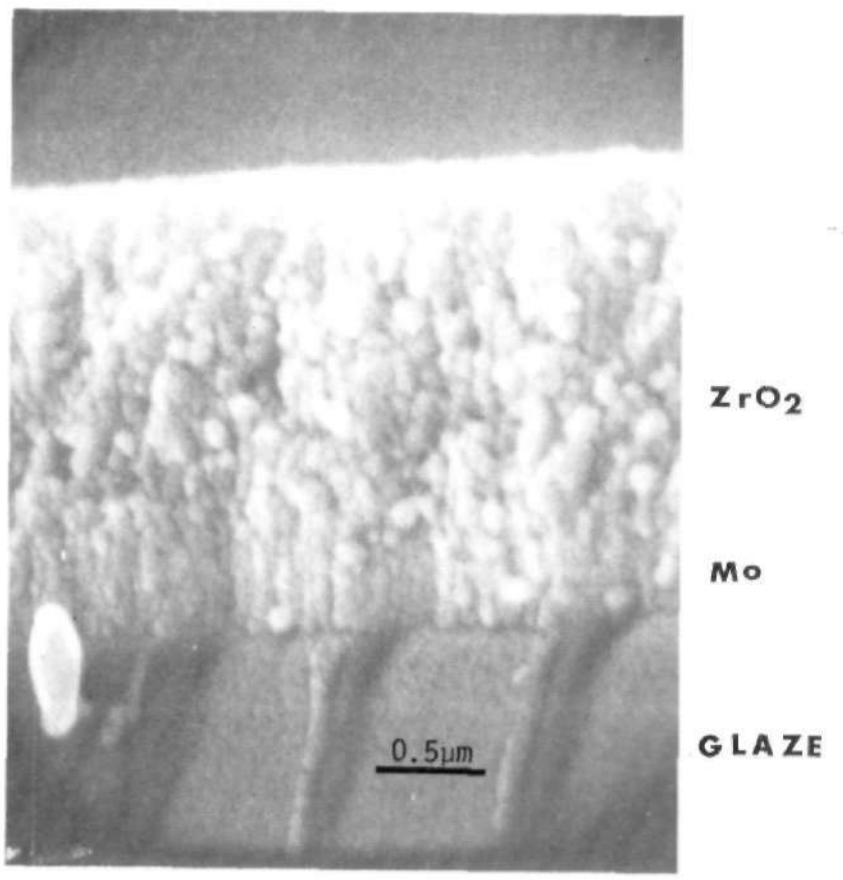


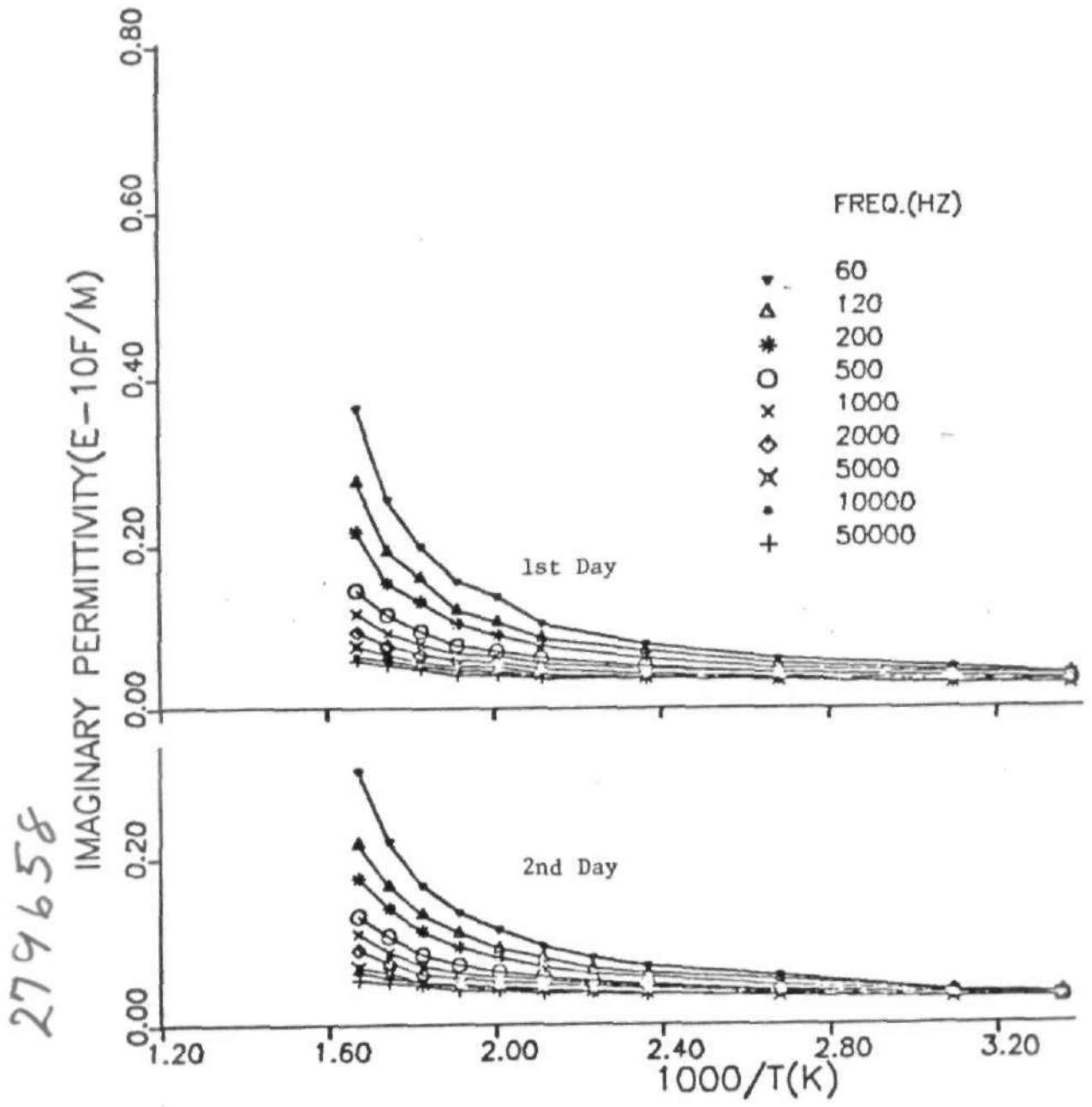
Fig. 36. Scanning Electron Micrograph of the Fracture Surface of ZrO_2 Thin Film, Sample Z4, Deposited At 420°C.

crystallites.

4.1.2 Ac Properties

It was important initially to establish the temperature and vacuum treatment of the ZrO_2 films needed to stabilize the ac porperties. In the following discussion, stabilization of ac properties will be referred to as elecrical stabilization to distinguish it from structural stabilization which will be referred to as stabilization. Dawson et al. [3] stated that anodized ZrO_2 films with gold electrodes were electrically stabilized on cycling to 200 °C. However, films with silver and indium electrodes did not give reproducible results with that treatment. The films prepared in this study, were hence cycled to 200 °C before measurements were made in a vacuum less than 10^{-4} torr. The films deposited at temperatures above 400 °C were electrically stabilized with 200 °C cycing in vacuum, but those deposited at lower temperatures required longer heat treatments to obtain reproducible results.

Imaginary permittivity, $\varepsilon''\varepsilon_o$, versus reciprocal temperature for samples deposited at 450 °C and 350 °C, respectively, are shown in Figures 37 and 38. Measurements were made on successive days and were taken within a period of eight hours each day. The films were kept in vacuum for all the days. In Figure 37 there was a minor decrease in values for the 450 °C sample on the second day due to aging and the shape of the curves remained unchanged with time. For the 350 °C deposition, Figure 38, the $\varepsilon\varepsilon_o$ plots had a peak at about 200 °C on the first day. On the second day, the permittivity had decreased to profiles similar to the 450 °C samples of Figure 37. Upon exposing the 350 °C films to the atmosphere for two hours and re-running the tests, the initial plots



279658

Fig. 37. Imaginary Permittivity of Evaporated Mo-ZrO_2-Mo Sample Deposited at 450°C as a Function of Temperature and Frequency for Two Successive Days.

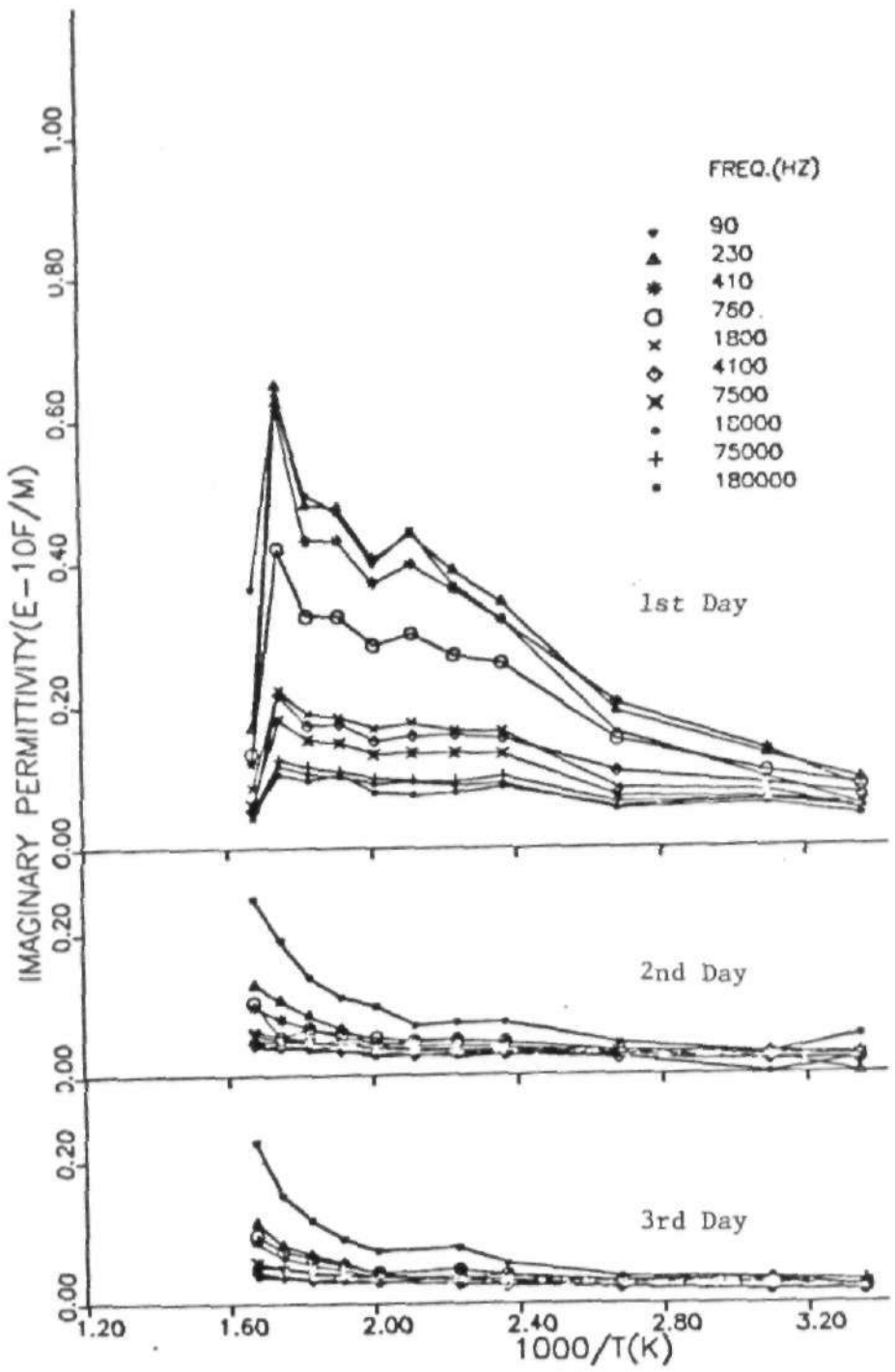


Fig. 38. Imaginary Permittivity of Evaporated Mo-ZrO_2-Mo Sample Deposited at 350°C, as a Function of Temperature and Frequency for Three Successive Days.

were approximately reproduced, showing that the relaxation peaks are due to some component of the atmosphere. The sample deposited at 300 °C did not exhibit a peak but $\varepsilon''\varepsilon_o$ was increasing with temperature at low frequencies. Decreasing $\varepsilon''\varepsilon_o$ required more extensive heating (300 °C for 21 hours) than for the 450 °C film. After heating the 300 °C sample had $\varepsilon''\varepsilon_o$ vs reciprocal temperature curves almost identical to the higher deposition temperature films. Apparently, the lower the deposition temperature, the more extensive the heat treatment in vacuum required to electrically stabilize the films. The sample deposited at 300 °C that had been electrically stabilized at 300 °C was exposed to dry oxygen gas for six hours and electrical measurements repeated. This test was repeated with nitrogen gas. Only small increases in $\varepsilon''\varepsilon_o$, much smaller than those produced by exposure to ambient air, were obtained. It was concluded that the relaxation peaks or the much higher $\varepsilon''\varepsilon_o$ values obtained for electrically unstabilized samples deposited at lower temperatures, was due to water adsorption in pores at the points of contact between ZrO_2 and molybdenum films. The possibility of the moisture being adsorbed partially or completely through the thickness of the ZrO_2 films could not be ruled out. The adhesion at the ZrO_2–molybdenum interface is poorer at lower deposition temperatures which may have been caused by interconnected porosity and thus increased moisture adsorption. Also, during deposition at the lower temperatures, the mobility of evaporant molecules on a substrate is reduced. This may reduce the growth of the nuclei and merging of islands, to produce increased porosity in the bulk ZrO_2 films. The diameter of such pores would be of the order of the grain size, that is, smaller than 200 Å,

and decreasing with decreasing deposition temperature. Calculations from the Kelvin equation indicates that water should be adsorbed by capillary condensation from a humid atmosphere by such fine pores at room temperature.

Clearly, it is important that literature on the electrical properties of films report the heat treatment and atmosphere conditions prior to measurement for properties to be useful for comparative purposes. The adhesion and moisture adsorption problems encountered here may also occur with other evaporated and sputtered films, varying in extent with the type of electrodes and deposition temperature. For example, Croset et al. [10] observed loss peaks for stabilized ZrO_2 films similar to those obtained for the electrically unstabilized sample deposited at 350°C. Both results were significantly different from those for films electrically stabilized by sufficient baking which had profiles identical to other loss profiles of uncontaminated ZrO_2 samples [3]. Contamination of pickled ZrO_2 films by fluorine was shown to produce loss peaks by Harrop et al. [6]. Hence, it cannot be determined whether Croset's loss peaks were due to oxygen vacancies in the stabilized ZrO_2 or due to water or other contaminants.

In the discussions to follow, reproducible results from films baked at 200°-300°C in vacuum for five to 21 hours are discussed. Measurement temperature will be referred to as temperature, whereas deposition temperature will be qualified. Both $\varepsilon''\varepsilon_o$, and real permittivity, $\varepsilon'\varepsilon_o$, when plotted as a function of reciprocal temperature with frequency as a parameter, had identical profiles for all samples. Figues 37 and 39 are typical plots for $\varepsilon''\varepsilon_o$, and $\varepsilon'\varepsilon_o$ respectively. The

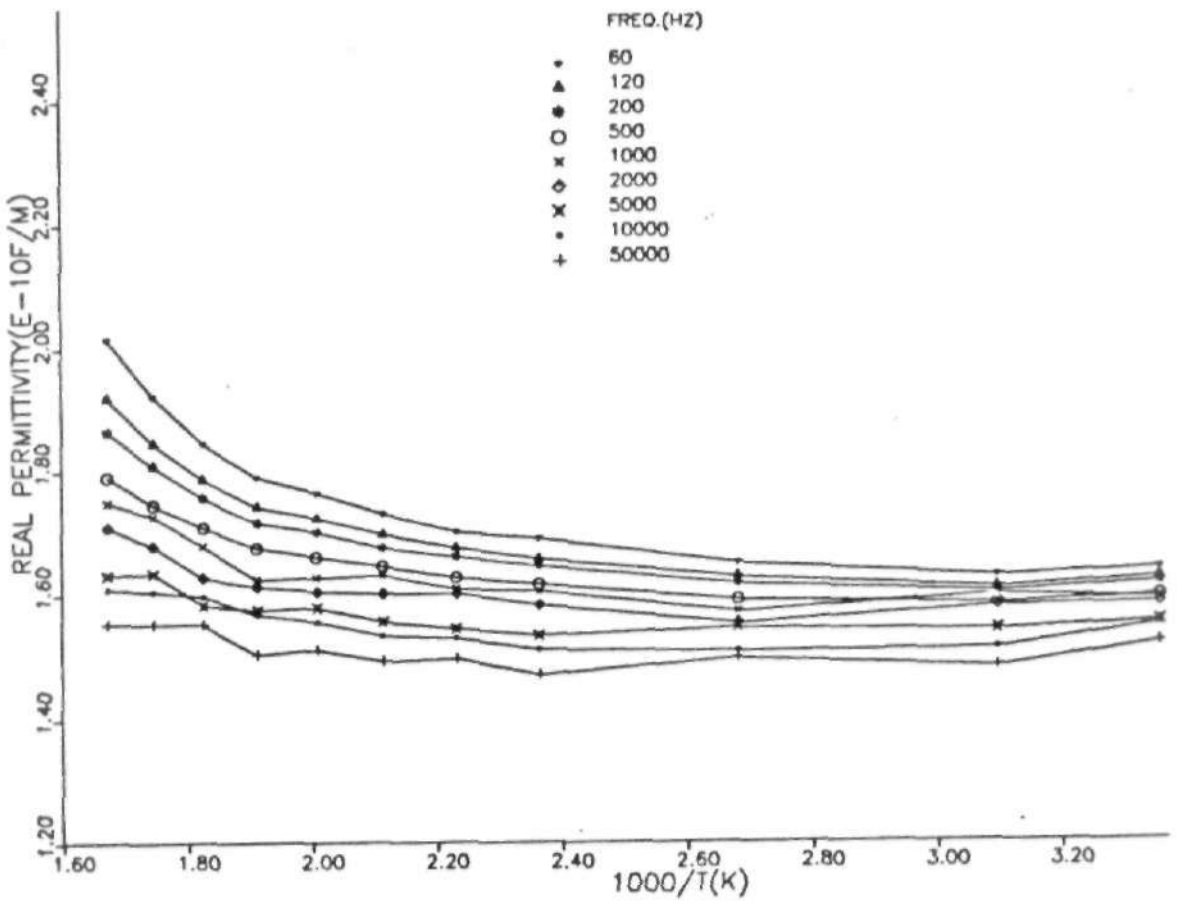


Fig. 39. Real Permittivity of Evaporated Mo-ZrO_2-Mo Sample, Deposited at 450°C as a Function of Temperature and Frequency.

values of the 1000 Hz $\varepsilon''\varepsilon_o$, are plotted as a function of temperature for samples deposited at various temperatures in Figure 40. Except for the permittivity of the samples deposited at 350 °c, which are unusually low, the permittivity at any temperature increased as the deposition temperature decreased from 450 °C to 300 °C.

Real and imaginary dielectric constants, ε' and ε'' respectively, were plotted in Figure 41 as a function of frequency on a log-log scale for 25°C (the low temperature) and 325°C (the high temperature). Both ε' and ε'' frequency dependence were linear relationships which could be expressed by

$$\varepsilon' \text{ or } \varepsilon'' = \text{Constant } f^{-x}. \qquad (63)$$

The values of x are tabulated in Table 5. At the low temperature, 25°C, a single linear relationship was obtained for vs frequency, indicating a single dispersion region. Under these conditions, $\varepsilon' \propto f^{0.01}$ holds for all the deposition temperatures. The versus frequency correlation however, was poor as indicated by low correlatio coefficient (Table 5).

At the high temperature, the and vs frequency relationship indicated two dispersion regions with the break occuring around 200-500 Hz. The increased temperature introduced an additional dissipation mechanism to produce the low- and high-frequency dispersio regions. The plot showed either two or three dispersion regions. The low frequency break also occured at 200 Hz. to 500 Hz. The x decreased as deposition temperature decreased from 450 °C to 300 °C, again, except for the samples deposited at 350 °C, which have unusually

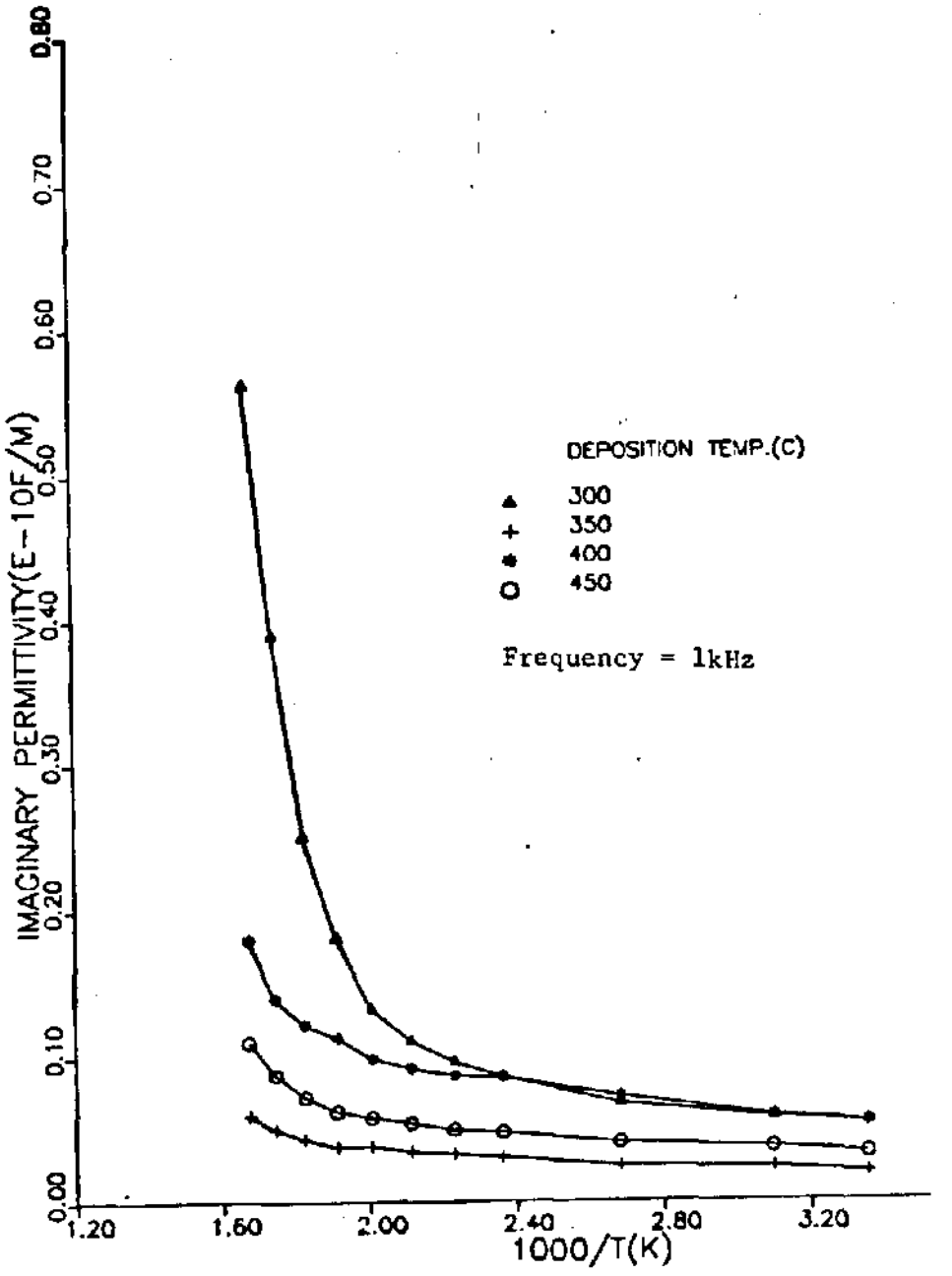


Fig. 40. Imaginary Permittivity of Evaporated Mo-ZrO_2-Mo Samples, Deposited at Varying Temperatures, as a Function of Reciprocal Temperature.

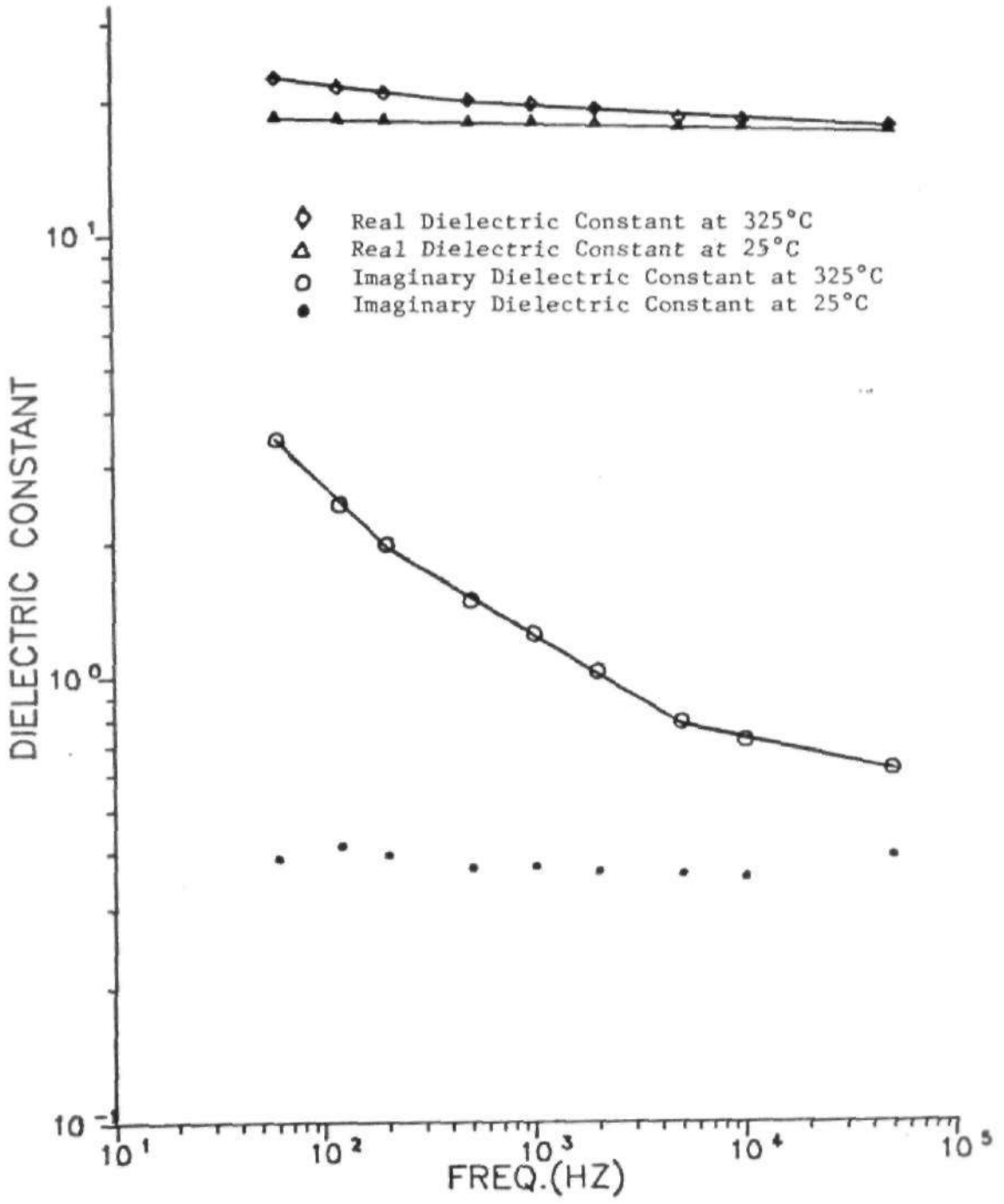


Fig. 41. Real and Imaginary Dielectric Constants of Evaporated Mo-ZrO_2-Mo Sample, Deposited at 450°C, as a Function of Frequency at 25°C and 325°C.

Table 5. Values of x for Dielectric constant-Frequency relation for ZrO_2 films deposited at varying temperatures.

		ε'			ε"	
Temp.(°C)	25	325		25	325	
Deposition Temp.(°C)		Low Freq.	High Freq.		Low Freq.	High Freq.
300	.012	.092	.062*	.006*	.691*	.484
350	.010	.051	.024	.042*	.421*	.020*
400	.016	.071	.037	.019*	.444	.092
450	.011	.056	.032	.013*	.397	.104

*Results with correlation coefficient less than 0.99.

Low Freq.: 60Hz-(.5-1)KHz.

High Freq.: (.5-1)KHz.-50KHz.

low values.

Samples deposited above 350 °C had a room temperature real dielectric constant of 22 $\pm$ 3, which is identical with that obtained by Horrop and Wanklyn [53] for single crystals of ZrO_2 of unspecified orientation. The films deposited at 300° C had a dielectric constant of 27 after an extended period of heating in vacuum, indicating that it was far from an ideal crystal structure. Departure from ideal structure could be caused by porosity and adsorbed moisture, which would

constitute additional support to the suggestion above that moisture was adsorbed by the samples deposited at lower temperatures. Such departure from crystallinity could also be due to an extensive development of defects such as grain grain boundaries. Both effects could actually be contributing in the sample deposited at 300 °C.

Dielectric conductivity, σ_d, versus frequency on log-log scale for low and high temperatures, Figure 42, yielded straight line segments. This was typical of all temperatures. At 25 °C, a single straight line was obtained, but two line segments with a break at 500-1000 Hz was typical at 325 °C. The linear regions may be expressed as

$$\sigma_d = \text{Constant } f^y. \tag{64}$$

The values of y are plotted in Figure 43 as a function of deposition temperature. At 25 °C, a frequency independent loss behavior was observed, $\sigma_d \propto f^{1.0}$, which was invariant with deposition temperature (curve 1). At 325 °C. y decreased for all deposition temperatures, the low-frequency region (curve 3) having much lower values (0.3-0.6) than the high-frequency region (0.63-0.87), curve 2. In both frequency regions, y values for the samples deposited at 300 °C were much lower than those at other deposition temperatures. The high temperature, high frequency values (curve 2) show a maximum at 350 °C, and became constant at 0.8 at higher deposition temperatures. At low frequency (curve 3), y values increased gradually with increases in deposition temperature.

To further analyze temperature dependence of dielectric conductivity, two Arrhenius type plots were considered, Equation (53), and

$$\sigma_d = \frac{\sigma_o}{T} \text{Exp} \left(- \frac{E}{kT} \right) \tag{65}$$

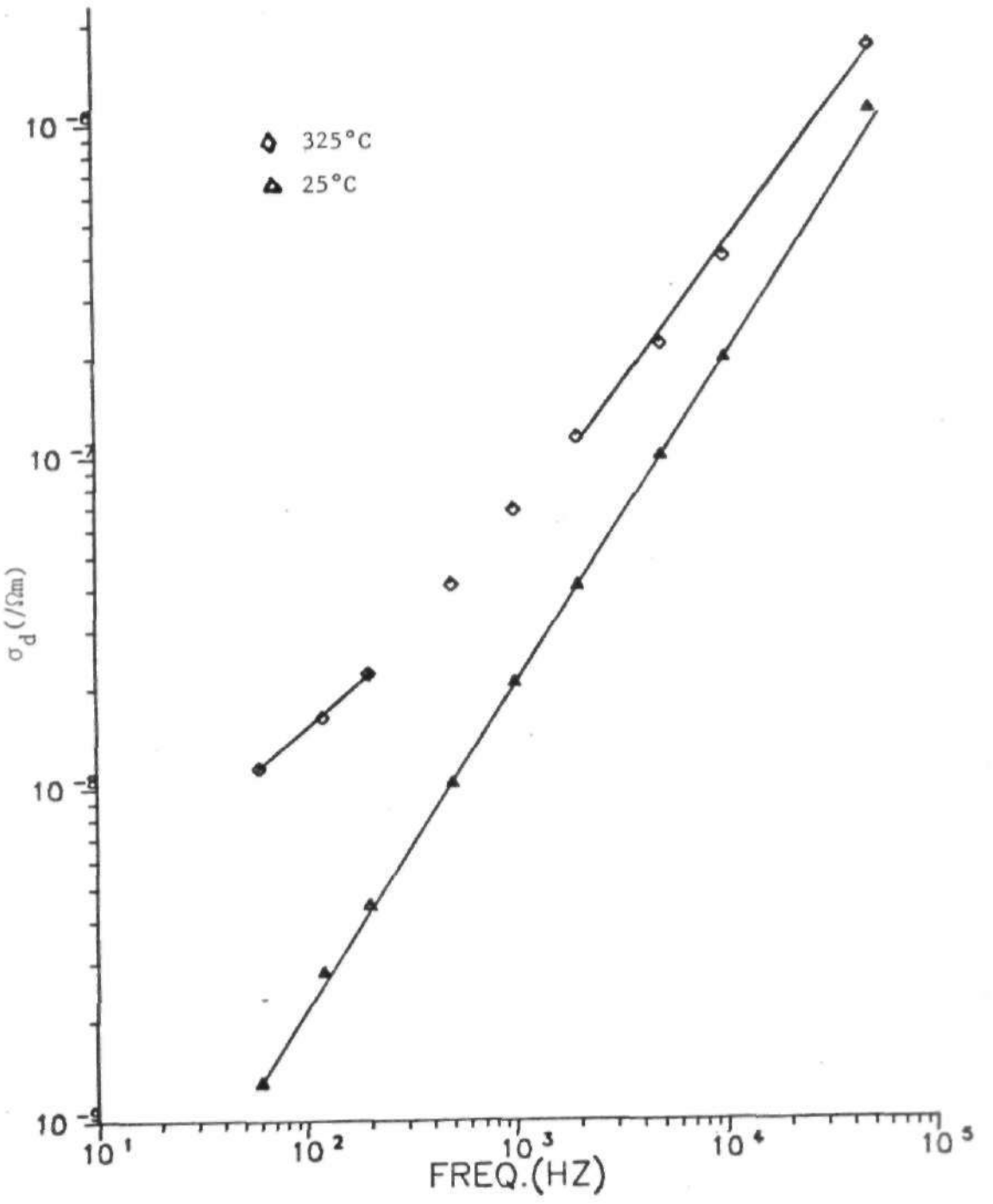


Fig. 42. Dielectric Conductivity of Evaporated Mo-ZrO_2-Mo Sample, Deposited at 450°C as a Function of Frequency at 25°C and 325°C.

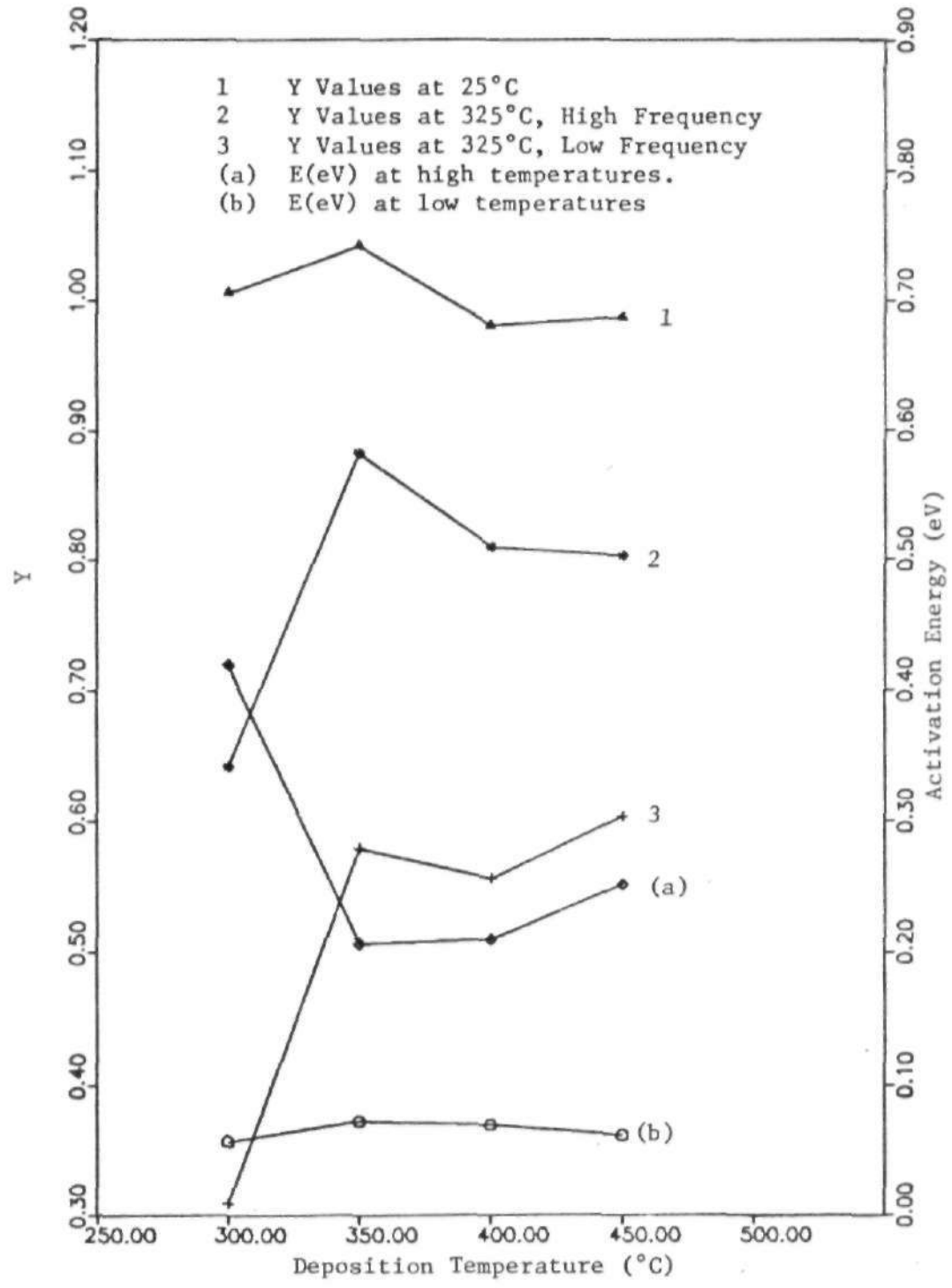


Fig. 43. Activation Energy and Y Values for Evaporated Mo-ZrO -Mo Samples as a Function of Deposition Temperatures for the Different Dispersion Regions.

Equation (65) provided the highest correlation coefficients from linear regression analysis for all deposition temperatures. Therefore, activation energies, E, were calculated from Equation (65) but E values from Equation (53) were similar. A typical 1 KHz (σ_d * T) versus reciprocal temperature plot is presented in Figure 44 and σ_d versus reciprocal temperature plot is provided in Figure 45 for comparison. All samples exhibited a low temperature (25°-150°C) linear relation and a high temperature (250°-325°C) linear region but for some deposition temperatures there was an intermediate linear region. These activation energy values are plotted as a function of deposition temperature in Figure 43. The low temperature activation energies ranged from 0.05 to 0.07 eV and were constant with deposition temperature. There was a marked increase in the activation energy values in the high temperature region, ranging from 0.21 to 0.42 eV with a minimum for a 350°C deposition temperature.

For comparative purposes, the dielectric conductivity for samples deposited at 450°C and 300°C were plotted in Figure 46 as a function of reciprocal temperature along with values obtained for ZrO_2 films deposited by other methods and an alumina film studied in this laboratory. The conductivity of samples from this work deposited at 300°C are similar to those of the anodized samples of Dawson et al. [3] with gold counter electrodes. Sputtered CSZ [10] shows much higher conductivities at temperatures below 300°C whereas the CVD samples of Tauber et al. [11] had the lowest conductivities at temperatures lower than 170°C. The conductivities of Tauber et al., however, turn up sharply at higher temperatures with an activation energy higher than

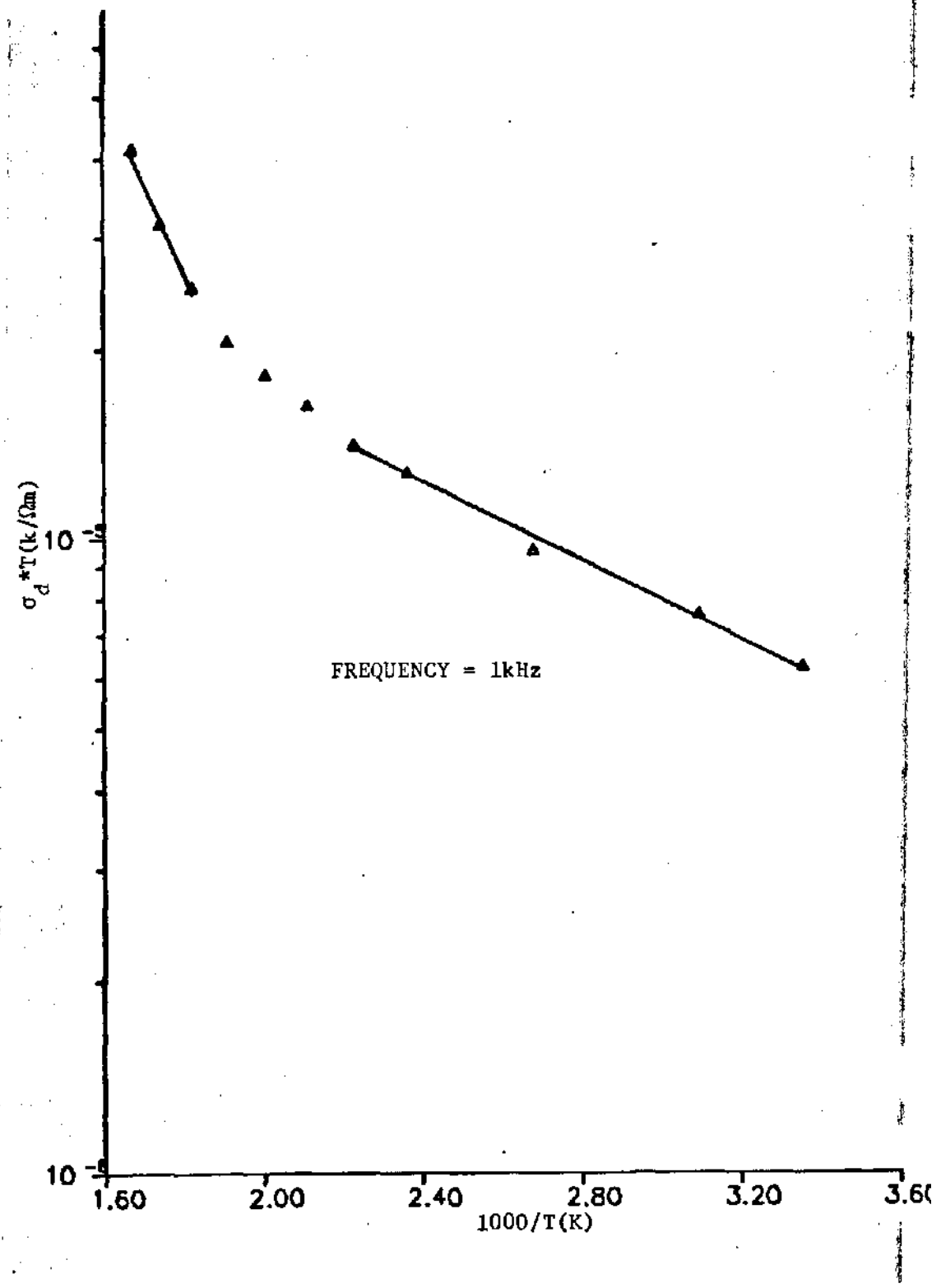


Fig. 44. Product σ_d*T for Evaporated Mo-ZrO_2-Mo Sample, Deposited a
450°C as a Function of Reciprocal Temperature.

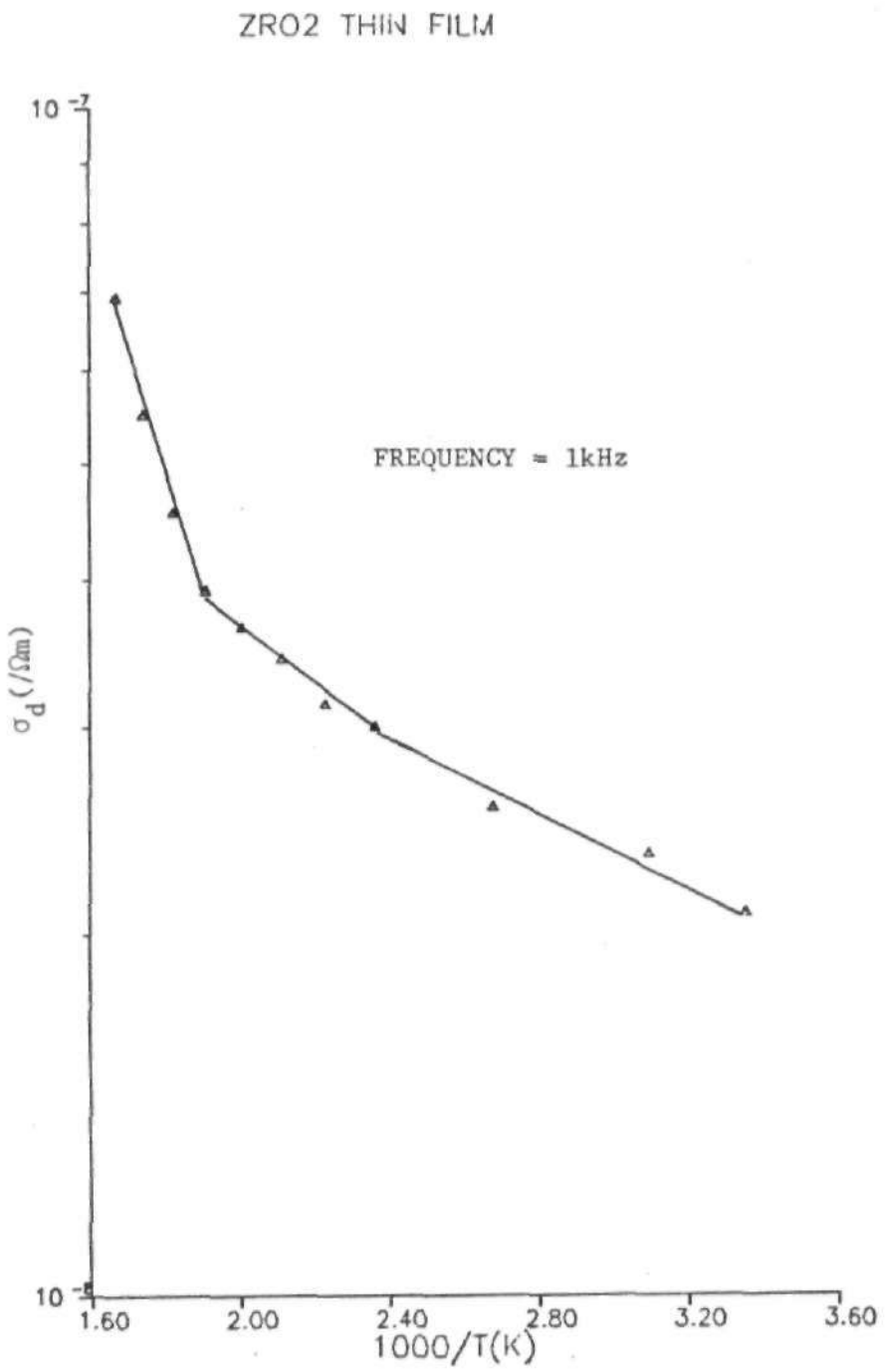


Fig. 45. Dielectric Conductivity of Evaporated Mo-ZrO_2-Mo Sample Deposited at 450°C as a Function of Reciprocal Temperature.

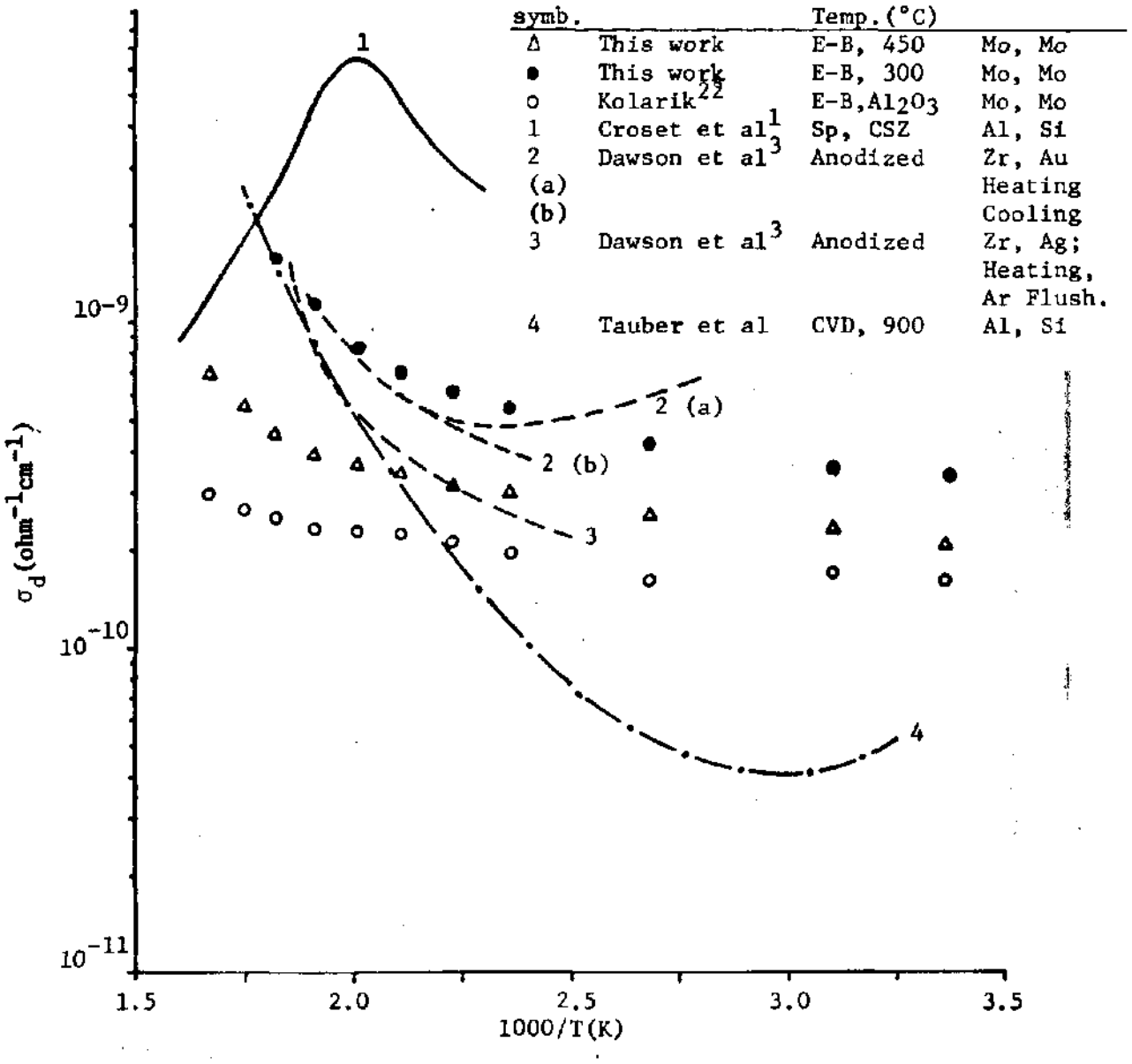


Fig. 46. Dielectric Conductivity of Zirconia Thin Films Prepared By Various Methods as a Function of Reciprocal Temperature. The Conductivity Values of Dawson et al Were Measured at 1592 Hz; All Others Were Measured at 1000 Hz. E-B = Electron-Beam, Sp = Sputtered, and CSZ = Calcia-Stabilized-Zirconia.

those for the samples in this work. At temperatures higher than 230 °C, electron-beam deposited samples had the lowest conductivities, with alumina samples of Kolarik [67] having the lowest values, followed by our film deposited at 450 °C.

The conduction in the films studied was found to be ohmic in the voltage and temperature ranges used in this work, and so only ohmic conduction mechanisms were involved. Apparently, at low temperatures the conduction is dominated by an electron-hop impurity conduction mechanism as evidenced by the very low activation energies [45]. At high temperatures however, one or more additional dissipation mechanisms seem to be operative to produce an increase in the activation energies and a decrease in the y values from 1.0. High frequency, high temperature y values of 0.8 above 400 °C deposition temperatures might suggest that a carrier hopping mechanism was operative. This was also concluded for alumina films by Birey [68] who based his conclusion on the agreement of his y values with the theoretical value of 0.79 for hopping of charge carriers. Further, the low y values (0.3-0.6) obtained in the low frequency, high temperature region could be explained by Birey's suggestion that additional low frequency dissipation mechanisms such as ion drift and interfacial polarization were contributing. However, note that at high frequency, high temperature, the sample deposited at 300 °C had a very low y value (0.3) which suggests that the low frequency dissipation mechanisms were contributing even at these high frequencies.

Tauber et al [11] obtained a variation of y values with temperature for CVD ZrO_2 in the frequency range 10^3 to 10^5 Hz that is

similar to the high temperature high frequency results obtained here. Their y values decreased from 1.0 to 0.5 as temperature increased from room temperature to 300 °C and they attributed the conduction to the remanence of a low-frequency Debye-type mechanism such as interfacial polarization. The results here furnish support for the contribution of interfacial polarization for ZrO_2 films at high temperatures and frequencies. The presence of other low frequency dissipation mechanisms such as ion drift, orientation polarization of adsorbed water or hydroxyl groups and the type of impurity orientation polarization observed by Argall et al. [69] were not detected here and if operative, they must have been masked by the interfacial mechanism having a polarization peak below 60 Hz.

An analysis of the remanence of such a mechanism has been given by Morley et al. [54] who, considering the Cole-Cole form of the Debye equation for frequencies greater than the relaxation frequencies, showed that the conductivity could be approximated by

$$\sigma = \varepsilon_\circ (\varepsilon_s - \varepsilon_\infty)(2\pi)^y f^y / \tau^{(1-y)} , \qquad (54)$$

$$= \text{Constant } f^y$$

for a given sample and distribution of relaxation times. The values of y approaches one for a broad distribution of relaxation times and zero for a narrow distribution. This provides a good interpretation of the values observed here. At high temperatures, the distribution of relaxation times narrows as compared to low temperatures, hence y values

decrease at high temperatures. The general decrease of y values with deposition temperature is also explained fairly well. The sample deposited at lower temperatures are more disordered, which probably narrows the distribution of relaxation times as the environments of the individual species become more similar. The disorder in the films include grain boundaries and amorphous regions which increased with decreased deposition temperature.

Two other arguments suggest that low frequency polarization is also contributing in the high frequency, high temperature region. First, if the conduction in this region was due to a hopping mechanism alone for the samples deposited above 400 °C, the charge carriers would consist of a mix of electrons (or holes) and ions so as to give an intermediate activation energy between (0.05-0.07 eV) for electron hop and (1.18-1.22 eV) [10,70] for ionic conduction. This should yield a y value intermediate between 1.0 and 0.79, which is not the case here. Second, the Cole-Cole plot of the permittivities, a typical one is shown in Figure 47, does not give a semicircle, as would be expected for a dominantly hopping mechanism. The conduction observed in these films at the high temperatures and frequencies is, therefore, attributed to either (a) electron hop and the remanence of interfacial polarization or (b) a mix of electron hop, ionic conduction and interfacial polarization. To resolve the exact nature of the mix of mechanisms, further experiments to isolate the specific mechanisms are needed.

The high temperature, low frequency region is controlled by electron hop and interfacial polarization. The trends of y values (0.3-0.6) obtained for the high temperature, low frequency region can be

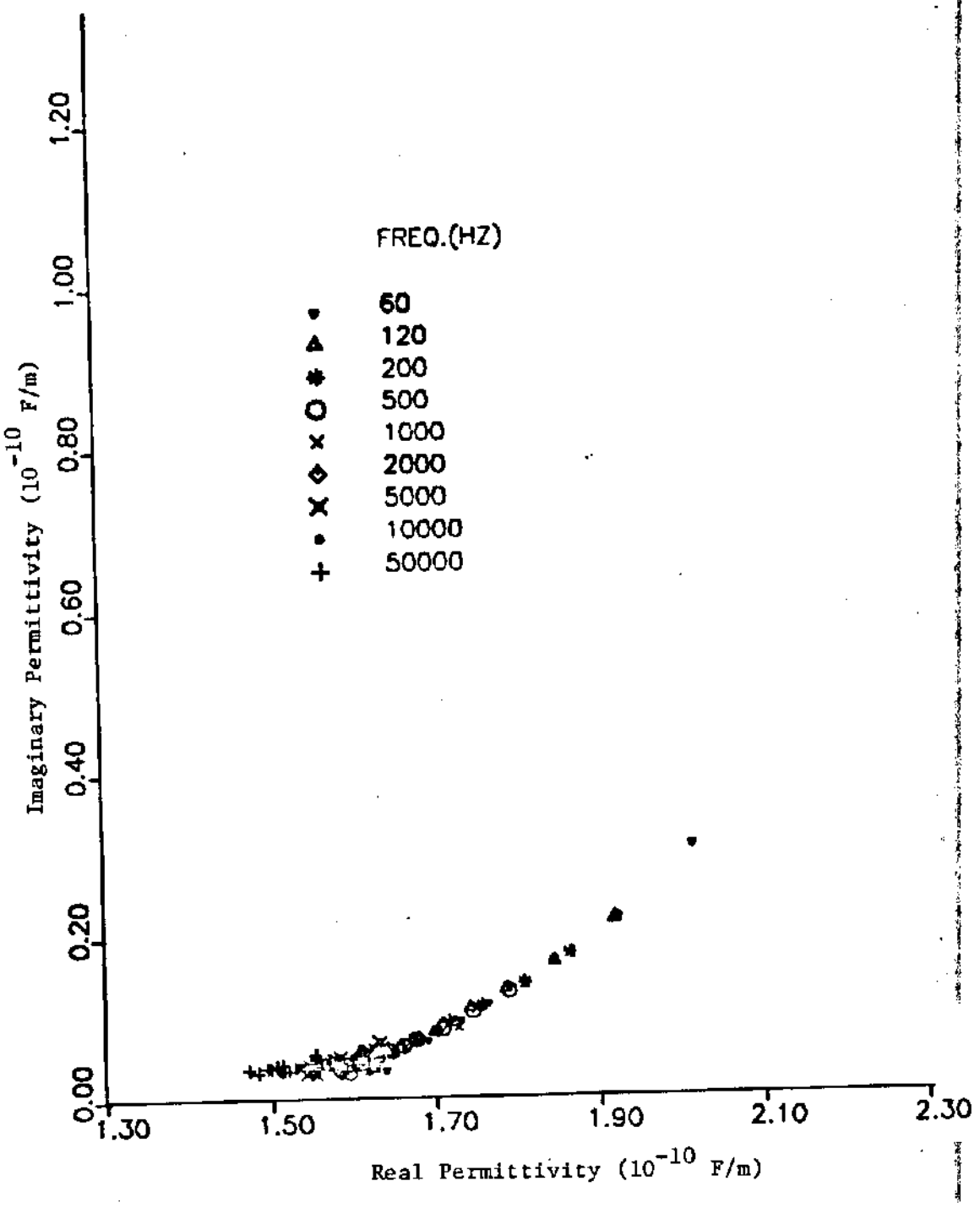


Fig. 47. Cole-Cole Plot for Evaporated Mo-ZrO_2-Mo Sample, Deposited at 450°C/

explained in terms of the film structure. Lower deposition temperatures, result in smaller grain sizes and hence more extensive grain boundary material. This would increase interfacial polarization so as to lower the y values in the manner observed here.

4.1.3 Dc Properties

From the structural studies and ac conduction results discussed earlier, as deposition temperatures increased from 300 °C to 600 °C two major characteristics were observed. Films deposited above 350 °C, showed more crystallinity and order and films deposited below 300 °C were characterized by disorder and probably amorphous character. Therefore, the dc property studies were conducted mainly for a crystalline film, Sample Z15, deposited at 450 °C and a disordered, low deposition temperature film, Sample Z14, deposited at 300 °C. Both samples were deposited in oxygen. A sample deposited at 450 °C in the absence of oxygen was found to be highly conductive, and so no further dc measurements were made on it.

4.1.3.1 Temperature Dependence

An Arrhenius plot of the Dc conductivity versus reciprocal temperature is presented in Figure 48 for Sample Z15E. The conductivity was measured at 25 V and 50 V, with both dot-positive and dot-negative polarity. The conductivity for the different voltages and polarities was identical at a given temperature except near room temperature where the current was low and and there was some scatter. Similar Arrhenius plots were obtained for Sample Z14B, and Z8F, deposited at 480 °C, so it was concluded that the 2μm films deposited in this work exhibited an ohmic and polarity-independent conduction for deposition temperatures of

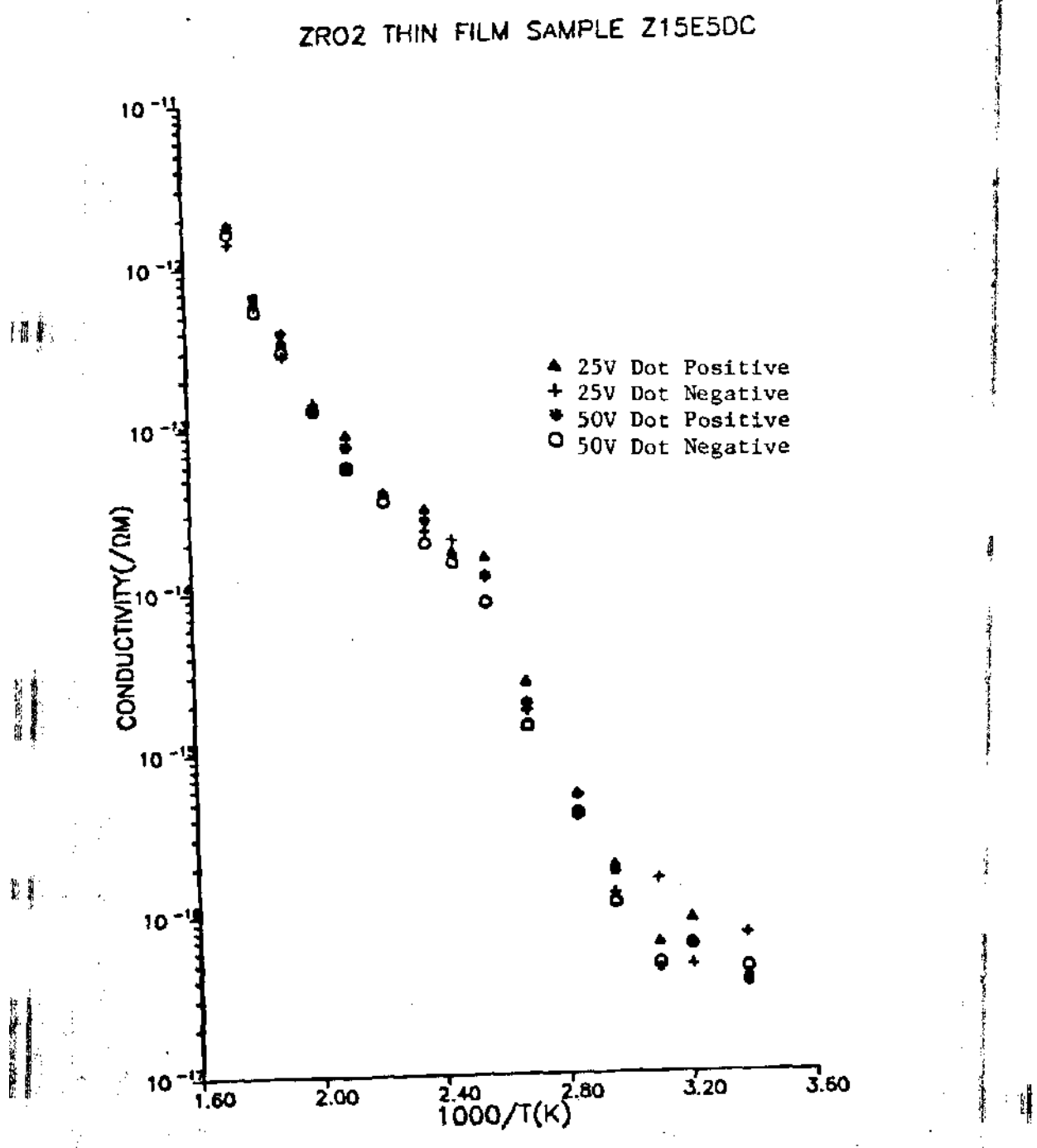


Fig. 48. Dc Conductivity of Evaporated Mo-ZrO_2-Mo Sample, Deposited at 450°C, As a Function of Reciprocal Temperature for 25 and 50 V and Positive and Negative Polarities.

300°-500°C at fields < 0.25 MV/cm . A characteristic feature of the Arrhenius plot observed for all samples was a decrease of the activation energy generally between 140° and 230°C although the Z14 sample continued to decrease above 230°C. An Arrhenius plot of 50 V dot-positive conductivity for Samples Z15E, Z8F, and Z14B (Figure 49) illustrates the dip in activation energy and shows Z14 having higher conductivity than Z15 at all temperatures. The activation energies obtained for the samples in three temperature ranges between 50° and 300°C are given in Table 6. Outside the activation energy dip region, the activation energy values fall between 0.6 and 1.0 eV. These values are higher than those obtained from the ac conduction, which ranged

Table 6. Dc Conduction Activation Energy for Electron-beam Evaporated ZrO_2 Films

Sample	Deposition Temp.(°C)	Activation Energy (eV) Temperature Range (°C) 50-100	120-200	200-300
Z8F	480	0.59	0.46	1.00
Z15E	450	0.77	0.34	0.71
Z14B	300	0.56	1.00	0.70

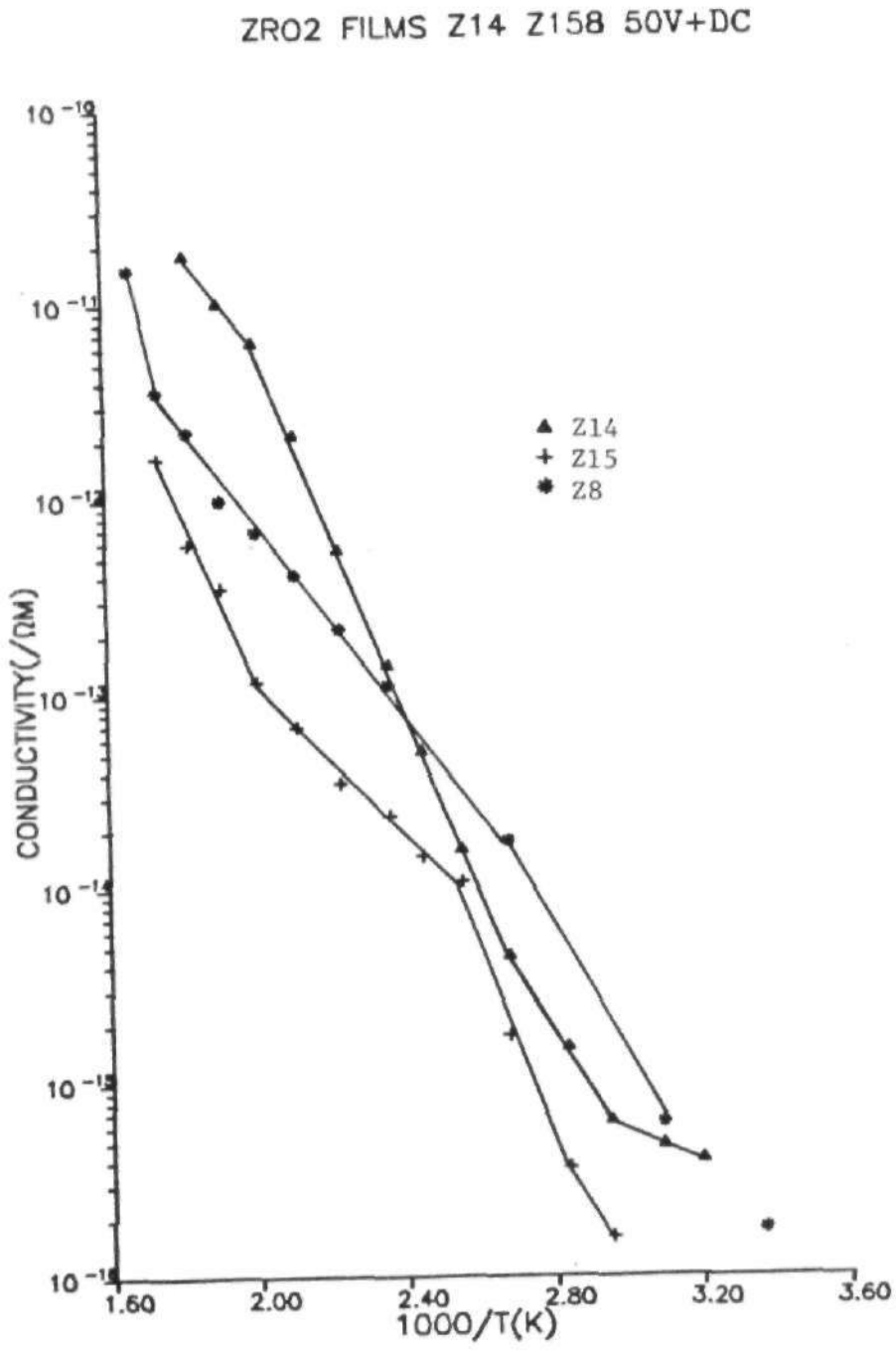


Fig. 49. Dc Conductivity, Dot Positive at 50V, of Evaporated Mo-ZrO_2-Mo Samples, Deposited at 300°C (Z14), 450°C (Z15) and 480°C (Z8) as a Function of Reciprocal Temperature.

between 0.05 and 0.4 eV. Furthermore, dc conductivity is at least two orders of magnitude lower than the dielectric conductivity near 300 °C and six orders lower at room temperature (compare Figures 48 and 45). The ohmic conduction observed could have been the result of surface conduction, the effect of adsorbed moisture, and/or a mix of oxygen ion and electronic conduction and recombination of charge carriers.

Surface conduction effects were first ruled out by establishing that the conduction was actually a bulk effect. This was done by depositing on the same glazed alumina substrate, at 450 °C, Mo-ZrO_2-Mo and ZrO_2-Mo (no bottom electrode) films. Conduction was measured between two molybdenum electrodes 4 mm apart on the ZrO_2 film with no bottom electrode. No conduction was observed between room temperature and 400 °C, indicating that surface conduction was insignificant in this case. The normal capacitors on the same ZrO_2 film exhibited typical conduction characteristics discussed above, showing that the current passed through the bulk of the films.

Another possible cause of the conduction in these films was adsorbed moisture. In this case, the decrease in the activation energy plots could be due to loss of water which was probably enhanced above the boiling point of water. It should be emphasized that the films were baked to at least 200 °C for at least five hours in 10^{-5} torr vacuum before making dc measurements. Therefore, any moisture remaining would be tightly adsorbed and difficult to remove. Films deposited at high temperatures would adsorb less moisture and require lower temperatures for desorption (120 °-230 °C). while higher desorption temperatures were required for the film deposited at 300 °C. In the ac measurements,

preheating the samples reduced loss and made the results reproducible. However, ac conductivities were higher than dc values and small amounts of moisture could appreciably affect dc conduction. It is possible that the films were impermeable to moisture movement at higher deposition temperatures, but moisture may have been present as hydroxyl groups trapped in oxygen vacancies. Peri et al. [71] observed alumina films covered with 40 % adsorbed moisture or hydroxyl groups after heating at 400 °C, and 2 % covered at 800 °C, which raised doubts as to whether any of the ZrO_2 films were ever completely dry. To confirm the moisture concept requires the study of the behavior of the activation energy dip with repeated heating at high temperatures but this could not be done in this work. Such a study could be combined with a study of the species adsorbed on the films. The activation energies observed here can then be attributed to conduction by adsorbed moisture either as water or as hydroxyl groups.

The second conduction mechanism that could be considered was a mix of ionic conduction and hopping of charge carriers since activation energies were between these respective values. The presence of cubic ZrO_2 phase in the films as discussed earlier could produce appreciable amounts of oxygen ion conduction along with the electronic conduction as noted for ac conduction. The higher activation energies obtained for the dc as compared to the ac conduction may be due to the suggestion by Chan et al [2] that the electronic conduction is probably more efficient under ac than dc conditions, thus making the high activation energies of the ionic conduction more significant in their contribution under dc conditions. The dip in activation energy could

then probably be due to a recombination of holes and electrons as the electronic contribution reduced at higher temperatures when the ions became more mobile.

If ionic conduction was present in the samples, an emf would be expected between the top and bottom molybdenum electrodes. Such an emf was indeed measured on all the samples above 250 °C in vacuum. For example, 8.5 mV at 340 °C for sample Z15F and 28 mV at 300 °C for sample Z8F. However, these voltages could not be related to ionic transference numbers since the oxygen partial pressure of the bottom Molybdenum electrode was unknown.

Note that the emf observed in the films does not favor any of the mechanisms suggested so far, since conduction by hydroxyl groups and water in the films could also produce such emf. Further work is required to resolve the specific mechanisms which are operative. It is quite possible that all three mechanisms: moisture effect, ionic conduction and electron hop were operative. The moisture effect might be dominating at lower temperatures (up to the dip in activation energy), when considerable amount of the moisture is lost. A mix of ion conduction and charge carrier hop then predominates after that.

4.1.3.2 I-V Characteristics

The I-V characteristics at 25 °C for samples Z15E and Z14B are presented in Figure 50. The conduction in Z15E was ohmic (slope of 0.9) up to 170 V and the sample had dielectric failure at 225 V (a field of 1.1 MV/cm). Sample Z14B (300 °C deposition temperature), however, exhibited ohmic conduction up to about 25 V (also a slope of 0.9). From 25 V to 49 V the I-V curve shows a slope of 1.9 (square law) and the

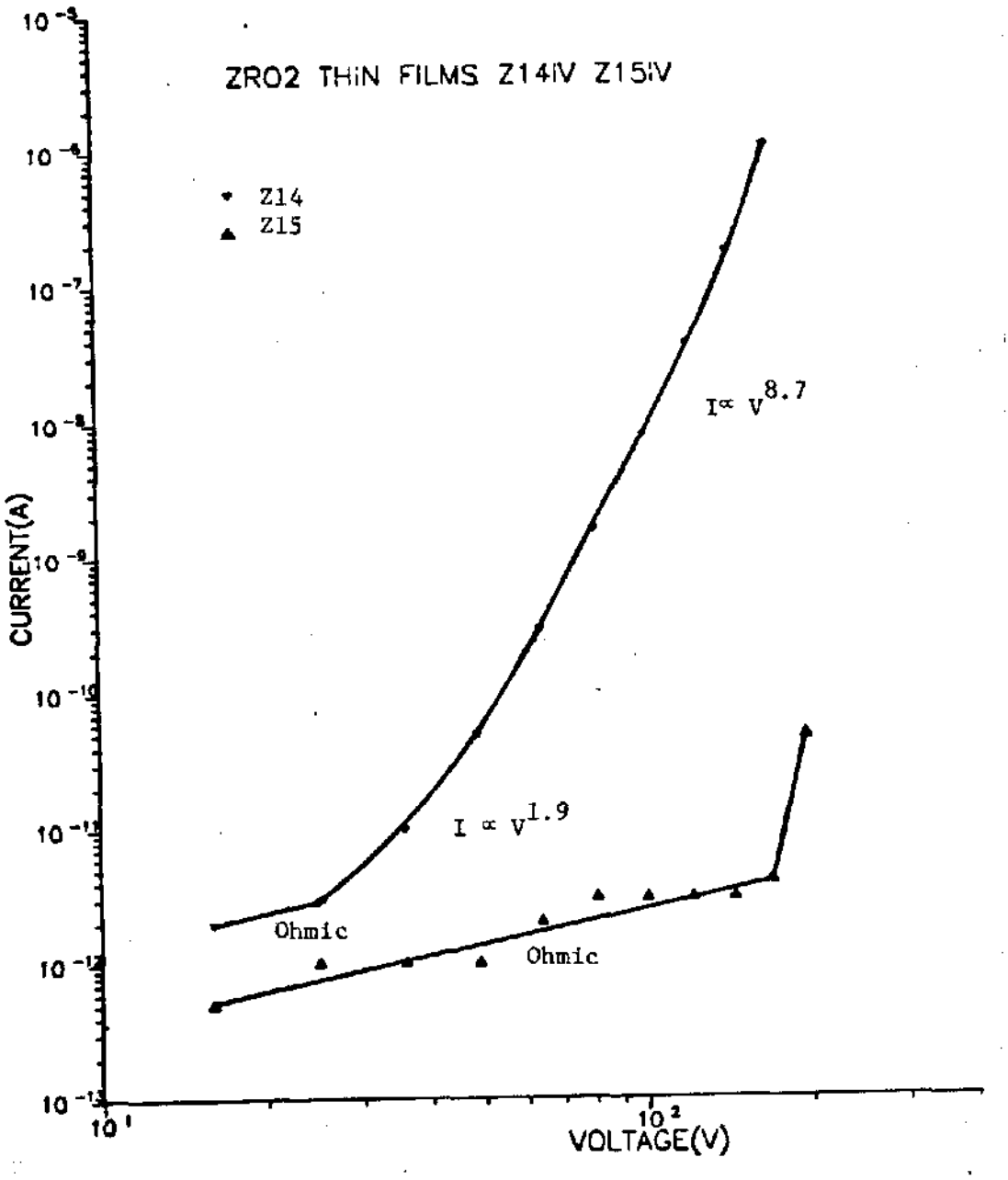


Fig. 50. Room Temperature I-V Characteristics for Evaporated Mo-ZrO -Mo Sample, Deposited at 450°C (Z15) and 300°C (Z14).

slope rises sharply afterwards to 8.7 between 81 and 169 V. Dielectric failure occured at about 196 V. The conduction in the non-ohmic region for this sample is probably due to SCLC. That would not be surprising as the Z14 sample is highly disordered and so has a high density of traps to reduce the mobility of electrons in the conduction band. Assuming a single trapping level, such SCLC would be represented by Equation (49):

$$J = \Theta' 9\varepsilon\varepsilon_0 V^2/8t^3 \qquad (49)$$

The square law region in Figure 50 yields a mobility μ, of $3.2 \times 10^{-14} cm^2/Vs$. However, the ratio of free charge carriers to free plus trapped charge, Θ', is unknown. If it is of the same order of magnitude as unity then the carrier mobility calculated was unusually low.

4.1.3.3 Charge Storage

Eisele [72] studied charge storage in electron-beam evaporated alumina films and found that the electron-injecting electrode was always next to the volume of higher charge storage which led him to conclude that the current was a measure of the number of chargeable traps present in the material. Eisele also found that in many samples the charge storage, was not symmetric with respect to polarity even though both electrodes were of the same material. Almost invariably, the larger amount was stored when the negative electrode was on top, that is near the oxide that had been deposited last. Eisele concluded that the source material had been subjected to electron bombardment for a longer

time and consequently was more oxygen depleted. These findings stimulated interest in charge storage in electron-beam evaporated ZrO_2 films as the method appeared to be a powerful way to follow the trap densities in the films.

Charge storage measurements were conducted for samples Z15E and Z14B, the former deposited at high temperature and the latter deposited at a low temperature. Dot positive and dot negative charge storage as a function of voltage and temperature are presented in Figures 51 and 52 for the two samples. A linear relation between charge storage and voltage was obtained for all the temperatures and for both dot polarities. At 25°C a static capacitance of 24 and 48.6 were calculated for samples Z15 and Z14 respectively. The values of 24 for Z15 agrees with the value extrapolated from the ac dielectric constants, but that of sample Z14 is larger than the extrapolated value of 27. However, for this sample, the extrapolation may be completely in error because the dielectric constant may rise more sharply as dc is approached. Sample Z14 shows a higher charge storage than sample Z15 (roughly double) for any given temperature, voltage, and polarity. Like previous interpretations, the former sample has more traps than the latter. With regard to the dot polarity, results quite different from those of Eisel [72] were observed. At 25° and 60°C, both samples showed little change of charge storage with the dot polarity, as can be seen in Figures 51 and 52. However, at 90°C sample Z15 shows a higher charge storage for the dot positive while sample Z14 showed the opposite, a higher charge storage for the dot negative. It was observed, however, that during the measurements the dot positive storage was measured

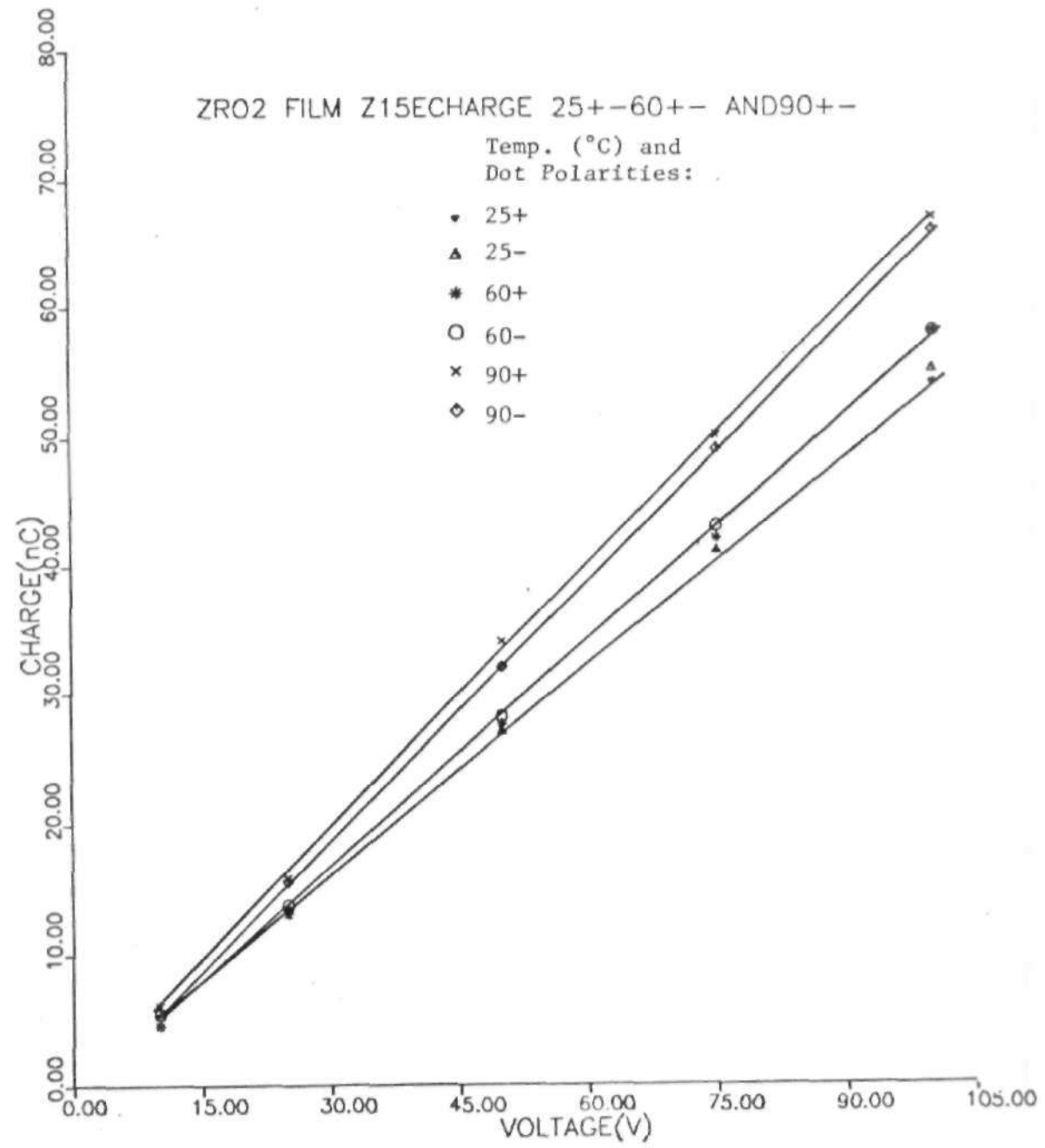


Fig. 51. Charge Storage for Evaporated Mo-ZrO_2-Mo Sample, Deposited at 450°C as a Function of Voltage for Three Temperatures and Positive and Negative Polarities.

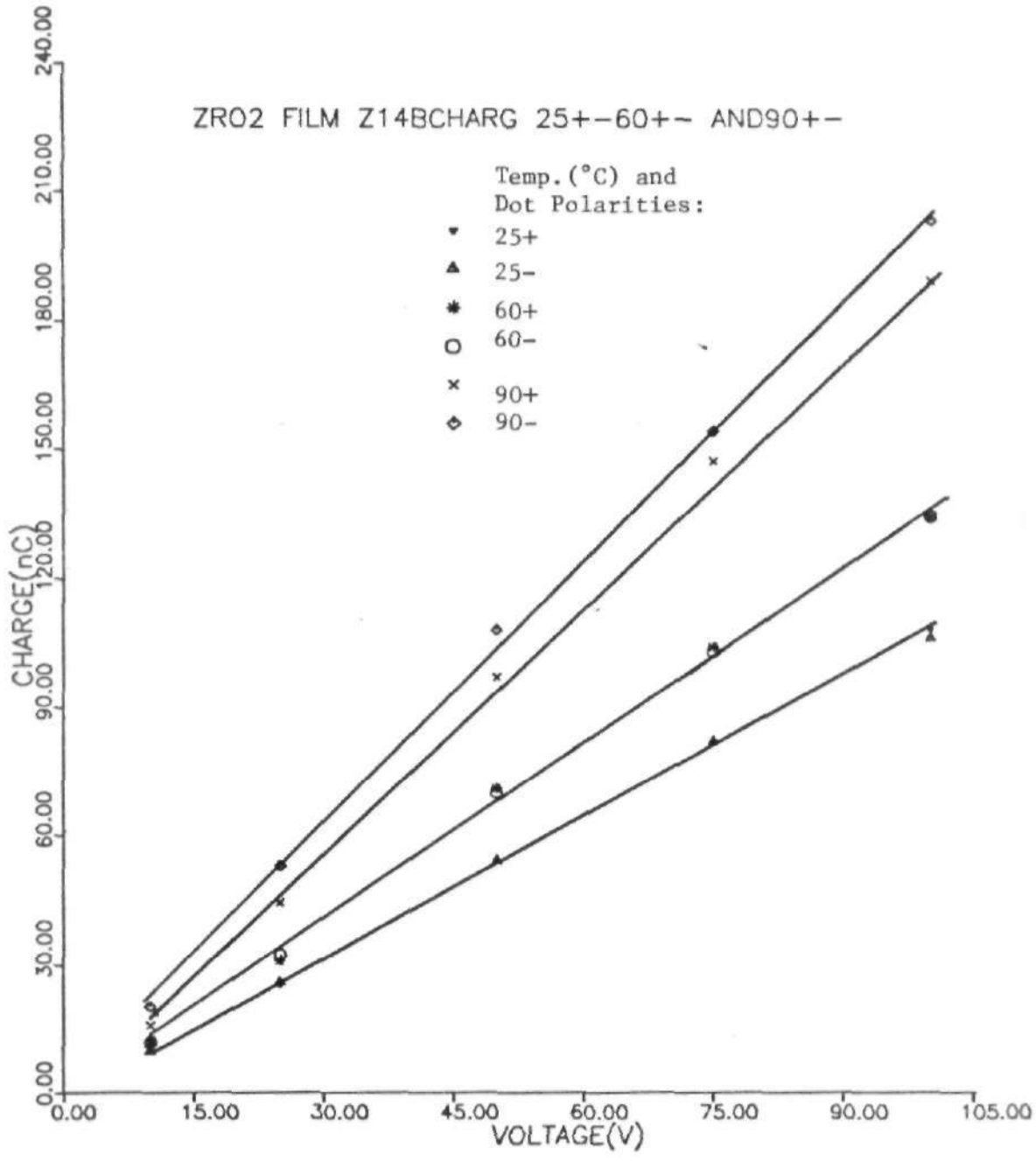


Fig. 52. Charge Storage for Evaporated Mo-ZrO_2-Mo Sample, Deposited at 300°C as a Function of Voltage for Three Temperatures, and Positive and Negative Polarities.

before the the dot negative for sample Z15 but the opposite (dot negative measured before dot positive) was done for sample Z14 at 90 °C. This suggested that the difference in charge storage for the two polaraities at 90 °C may be due to some remanence effect from the previous discharge. Note that if one polarity was consistently tested first, that polarity would show up with a consistently higher charge storage which may have been what Eisel [72] observed.

4.1.3 Impedance Spectroscopy

The admittance plots for all the samples deposited at temperatures above 350 °C, including that of a sample deposited at 450 °C in the absence of oxygen which was probably oxygen deficient, and the as-deposited oxide multilayer structures showed a single semicircle typica' of Figure 53. The semicircle is attributed to intragrain conduc"'on (bulk conduction), which is in agreement with similar conclu"'ons on the dc conduction of these samples. Since an interfacial polari-ation was considered operative in the ac conduction discussed above, the result here suggests that such interfacial polarization is due to bulk effect. Possible bulk effects are the grain boundaries and traps. The semicircle showed only a small spread of relaxation times, angle Θ_d was generally less than 10 °.

The admittance plot for Sample Z14B deposited at 300 °C was however, different, Figure 54. The plot seems to consist of a parallel capacitor-resistor effect dominating at low temperatures and frequencies that yields to a series capacitor-resistor bulk effect at higher temperatures and frequencies, Figure 55. The parallel capacitor-resistor effect seems to disappear with increasing temperature

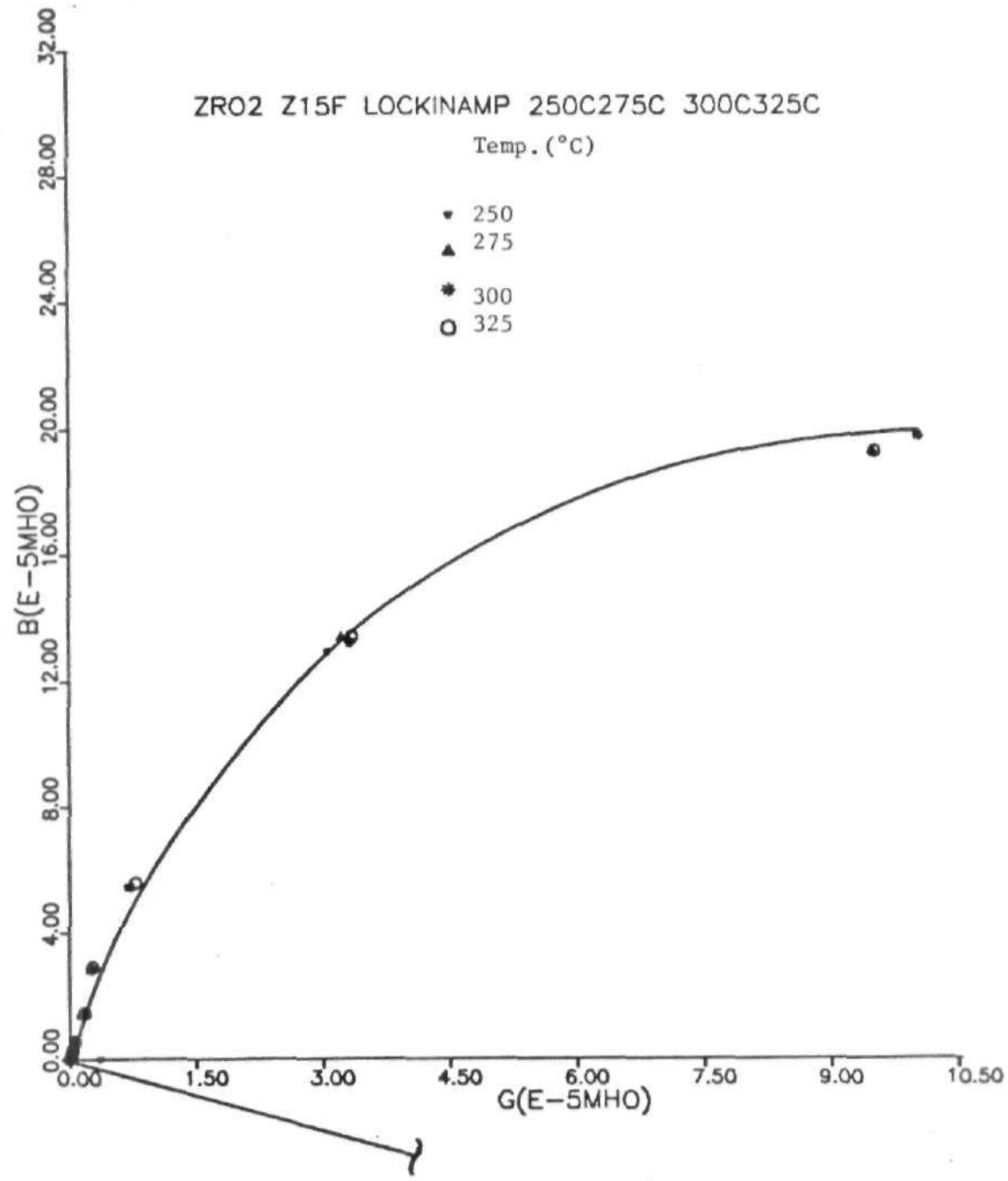


Fig. 53. Admittance Plots for Evaporated Mo-ZrO_2-Mo Sample, Deposited at 450°C, for Varying Temperatures.

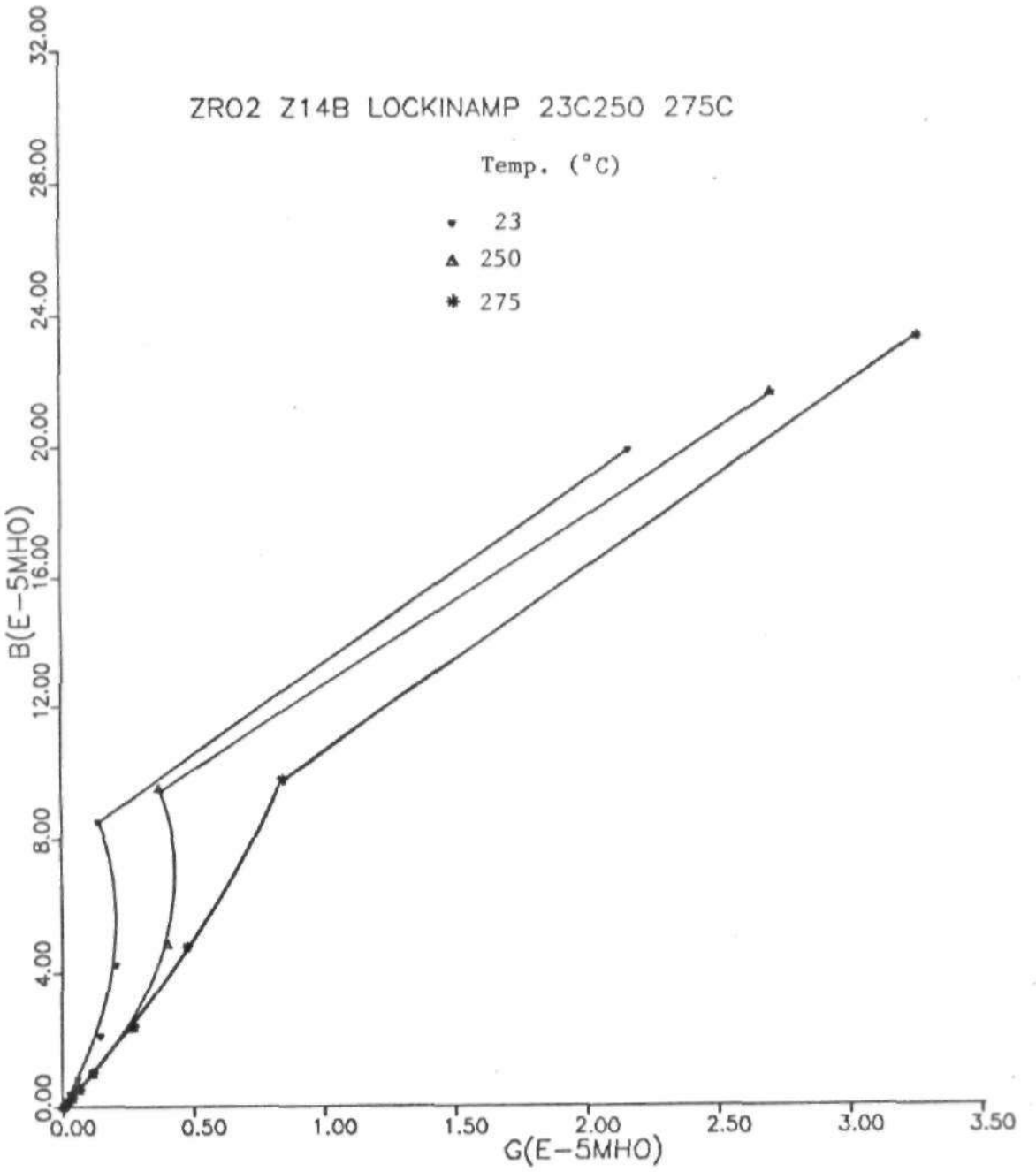


Fig. 54. Admittance Plots for Evaporated Mo-ZrO -Mo Sample, Deposited at 300°C for Varying Temperatures.

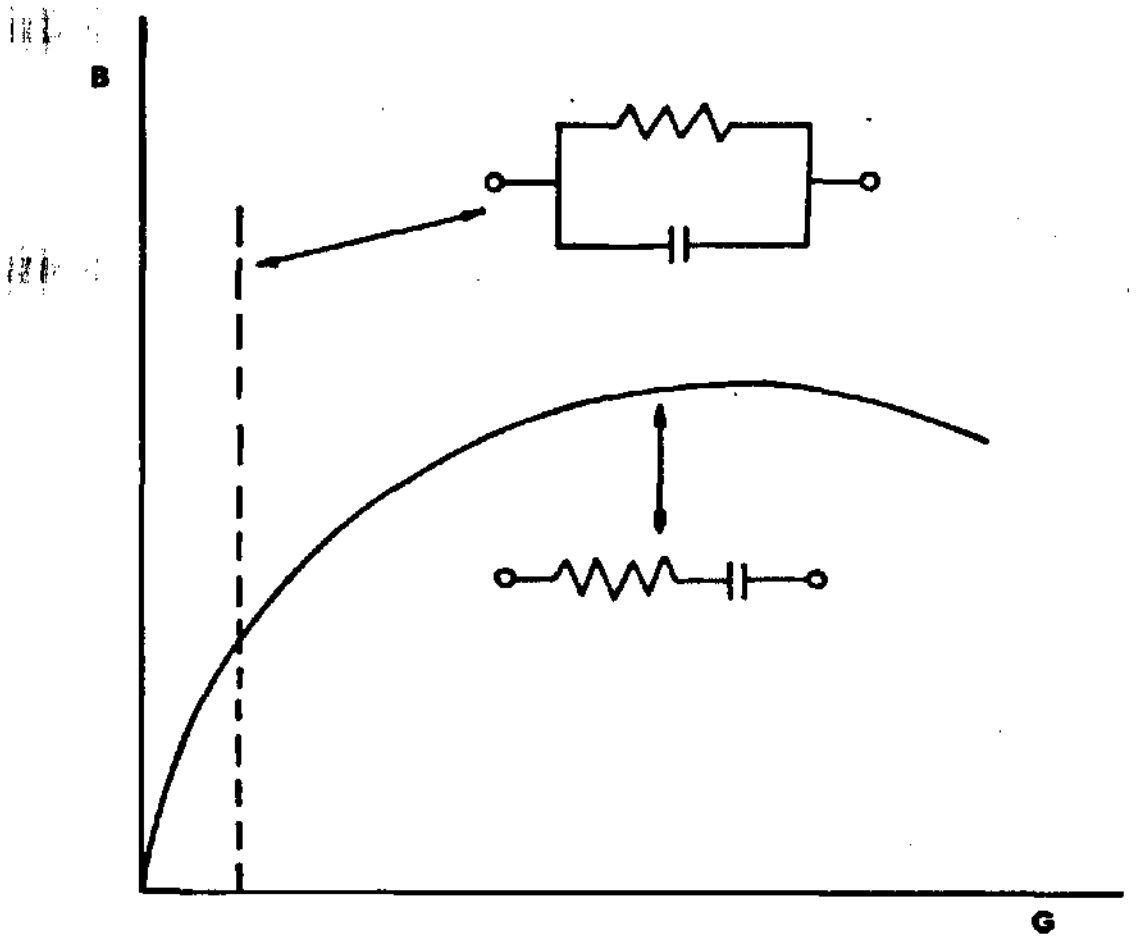


Fig. 55. Component Capacitor - Resistor Effects of the Admittance Plot of Mo-ZrO_2-Mo Sample, Vapor Deposited at 300°C (Schematic).

possibly due to the desorption of moisture with increasing temperature. This effect is similar to the stabilization of permittivity with heat treatment that was previously described in ac properties. However, in this case, it may be possible to actually study the effect directly by following changes in the parallel capacitor-resistor effect with temperature and other conditions. This has not been done here, however.

4.2 Y_2O_3,ZrO_2 Multilayer Structures

4.2.1 Crystal Structure

Crystalline phases present in the Pt/Rh-Y_2O_3,ZrO_2-Pt/Rh samples are indicated in the XRD patterns of Figure 56. Monoclinic ZrO_2 and cubic Y_2O_3 were the predominant components of the layers as-deposited at 490°C. Only a slight amount of the cubic or tetragonal ZrO_2 phase was present. Heat treating Pt/Rh-Y O ,ZrO_2-Pt/Rh samples at 800°C for five hours in air did not provide any phase change but nine hours at 1200°C converted the oxides to a yttrria-zirconia solid solution. The Y_2O_3 and monoclinic ZrO_2 peaks disappeared and strong cubic or mixture of cubic and tetragonal ZrO_2 peaks appeared. The yttria-zirconia phase diagram [66] indicates that the phases present should be cubic and either tetragonal or monoclinic ZrO_2 for the 10 mole percent Y_2O_3 in the film. As shown in Figure 57(a), the 1200°C Pt/Rh-Y_2O_3,ZrO_2-Pt/Rh structure had no (400) cubic ZrO_2 peak at all. However, it showed small (400) and (004) tetragonal peaks at 74.3 and 73.3° 2Θ respectively with intensities far below the expected 60 % and 40 % respectively for the randomly oriented tetragonal material. Hence, there was preferred orientation on this Pt/Rh-Y_2O_3,ZrO_2-Pt/Rh sample, since the cubic (400)

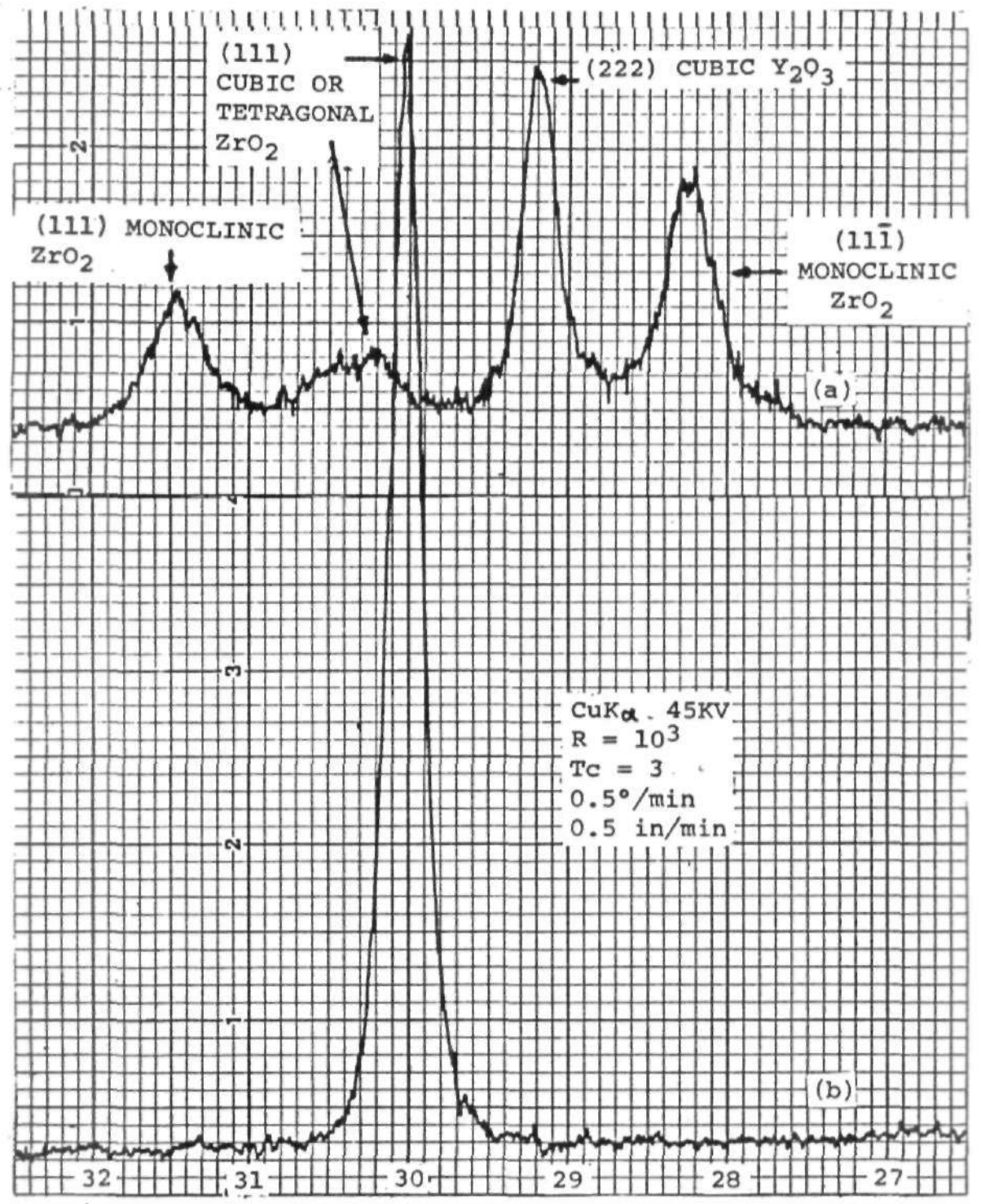


Fig. 56. XRD Patterns in the {111} Region for Y_2O_3-ZrO_2 Multilayer Film with Pt/Rh Electrodes (a) as Deposited, (b) Aged at 1200°C.

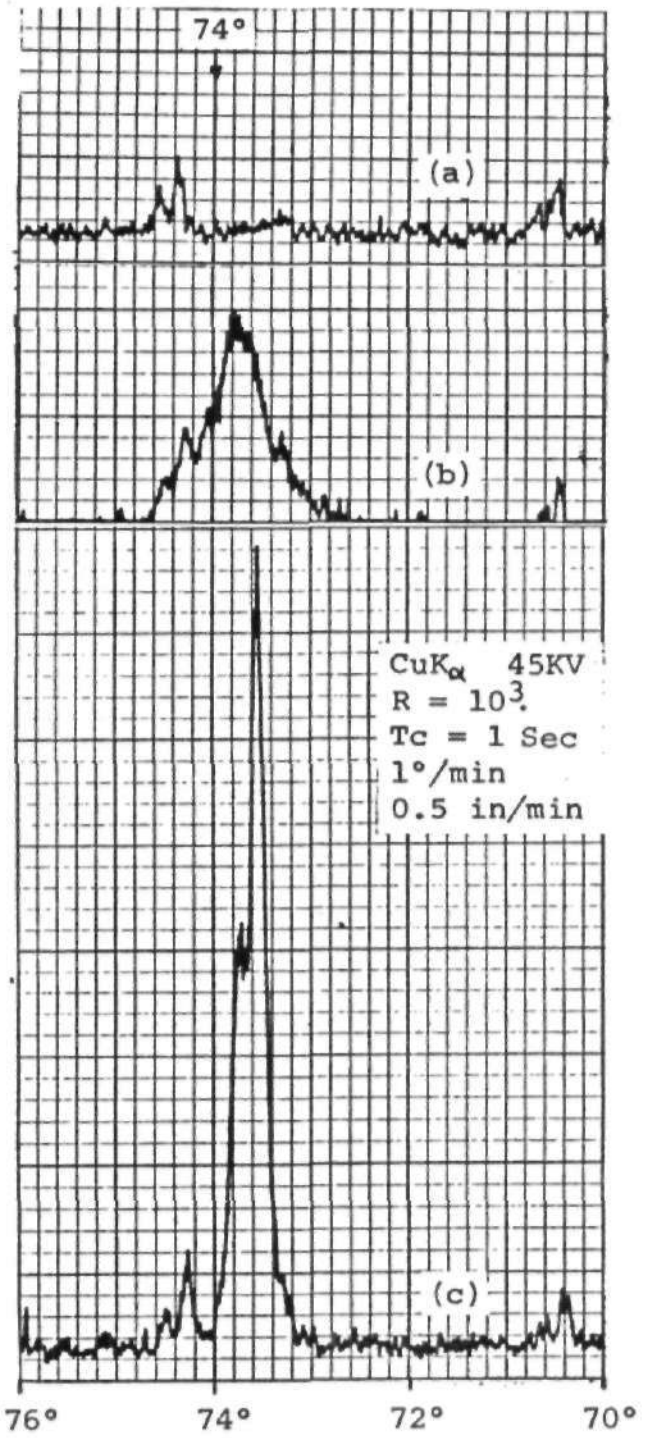


Fig. 57. XRD Patterns in the {400} Region for Y_2O_3-ZrO_2 Multilayer Film (a) with Pt/Rh Electrodes, Aged at 1200°C, and with Mo Electrodes (b) as Deposited, (c) Aged at 1200°C.

peak was absent when the phase was obviously present.

The Mo-ZrO_2-Mo sample on the other hand, had a significant amount of the cubic ZrO_2 besides the monoclinic ZrO_2 and cubic Y_2O_3 phases in the as-deposited state (Figure 58). The cubic ZrO_2 phase was confirmed by the (400) peak occuring at 73.8° 2Θ (Figure 56). The tetragonal (004) and (400) peaks were present but at small intensities compared to the (400) cubic peak. This strong development of the cubic ZrO_2 phase in Mo-ZrO_2-Mo structures could be due to more favorable epitaxial growth conditions on the cubic molybdenum electrode, as compared to the cubic Pt/Rh electrode. However, if the heat treated phase formed on Pt/Rh is not cubic but tetragonal, then it may be inferred that while cubic epitaxy is favored on molybdenum, tetragonal epitaxy is favored on Pt/Rh. The Mo-ZrO_2-Mo sample, on heating to 1200 °C for about seven hours in nitrogen produced a predominantly cubic structure. This is evident from a comparison of Figures 56(b) and 56(c). Note that the tetragonal (004) and (400) peaks did not increase in intensity during the heat treatment.

The results here prove that cubic YSZ films can be formed by multilayer deposition, probably aided by epitaxy on a suitable substrate such as molybdenum. Such epitaxial conditions in multilayer deposition could probably be easily realised on any substrate by depositing the cubic Y_2O_3 layer prior to subsequent oxide layers. Further work is needed to ascertain the exact influence of epitaxy in this method.

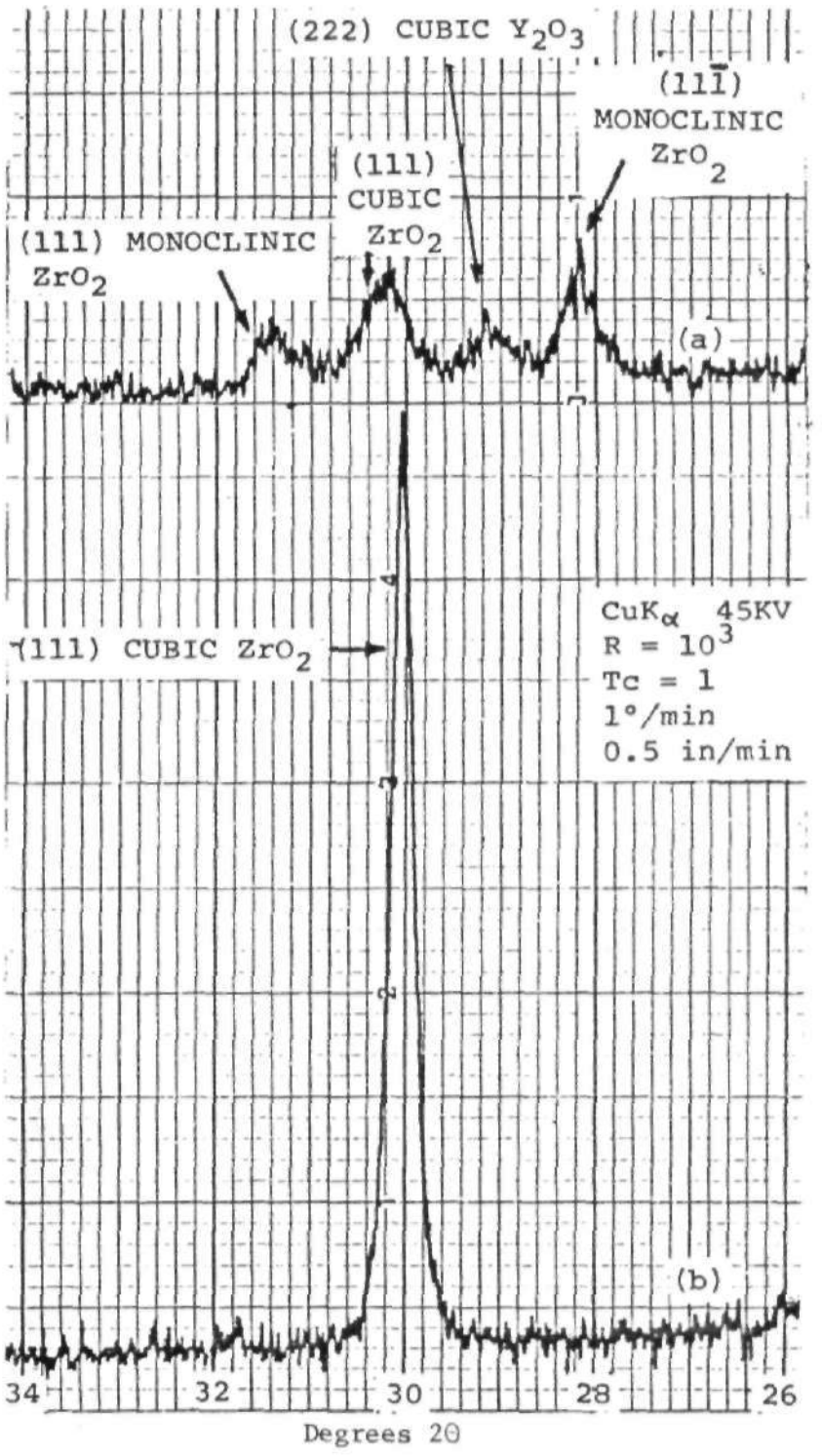


Fig. 58. XRD Patterns in the {111} Region for Y_2O_3-ZrO_2 Multilayer Film with Mo Electrodes (a) as Deposited, (b) Aged at 1200°C.

4.2.2 Dc Conduction

The Mo-Y_2O_3,ZrO_2-Mo sample heat treated at 1200 °C in nitrogen was found to be extremely conductive over the entire surface of the sample, and so no further measurements could be made on it. The best approach to study this sample is a four-probe technique and this should be done in the future. The high conductivity of the sample was due to reduction of the Y_2O_3,ZrO_2 film by either the molybdenum electrodes or by heat treatment in the nitrogen atmosphere.

The Au/Rd-Y_2O_3,ZrO_2-Pt/Rh structure however, was quite resistive after oxygen firing and so the temperature dependence and I-V characteristics were studied. An Arrhenius plot showed a single activation energy of 0.35 eV between room temperature and 429°C at 1.0 V (a field of 0.02 MV/cm), Figure 59. The I-V characteristics of the sample are presented in Figure 60. It shows two types of dependence, $I \propto V^{1.5}$ and $I \propto V^{3}$ in the voltage range of 1-64 V. This conduction may also be some form of SCLC effect. The production of holes by an oxygen interstitial mechanism (Equations 41 to 43), during the heat treatment in air (oxygen-rich) at 1200 °C may be responsible for this SCLC behavior. However, since the films were exposed to the ambient air before the Au/Pd electrode was sputtered, the conduction may be affected by trapped moisture or other contaminants. To see the effect of the sputtering on conduction, Au/Pd dots were sputtered on a Mo-ZrO_2-Mo sample deposited at 480 °C (Sample Z8) on portions where the top molybdenum electrodes were absent. The conduction of the molybdenum and Au/Pd dot capacitors were measured. It was found that most of the capacitors with sputtered electrodes were very conductive

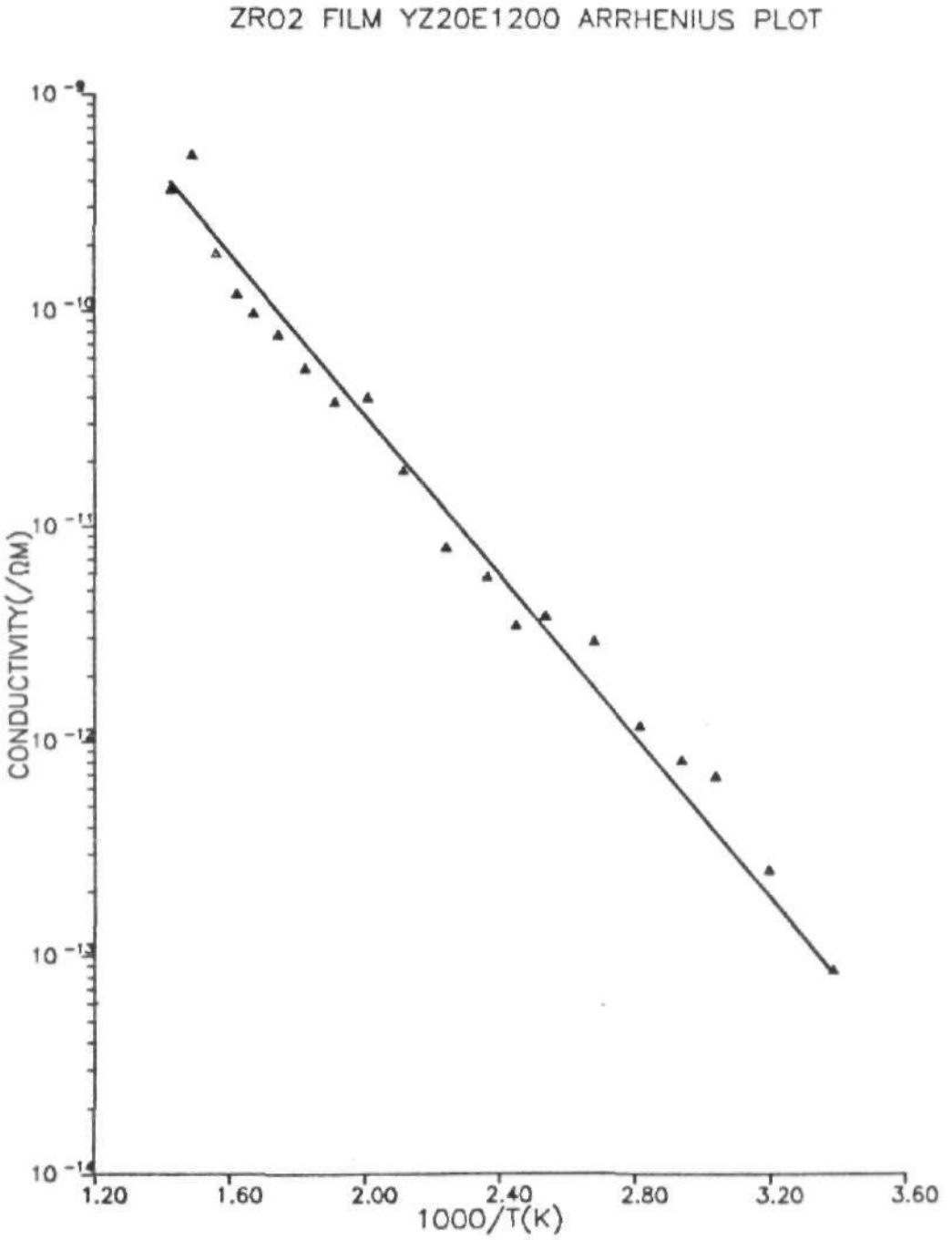


Fig. 59. Dc Conductivity of Au/Pd-Y_2O_3, ZrO_2-Pt/Rh Films as a Function of Reciprocal Temperature.

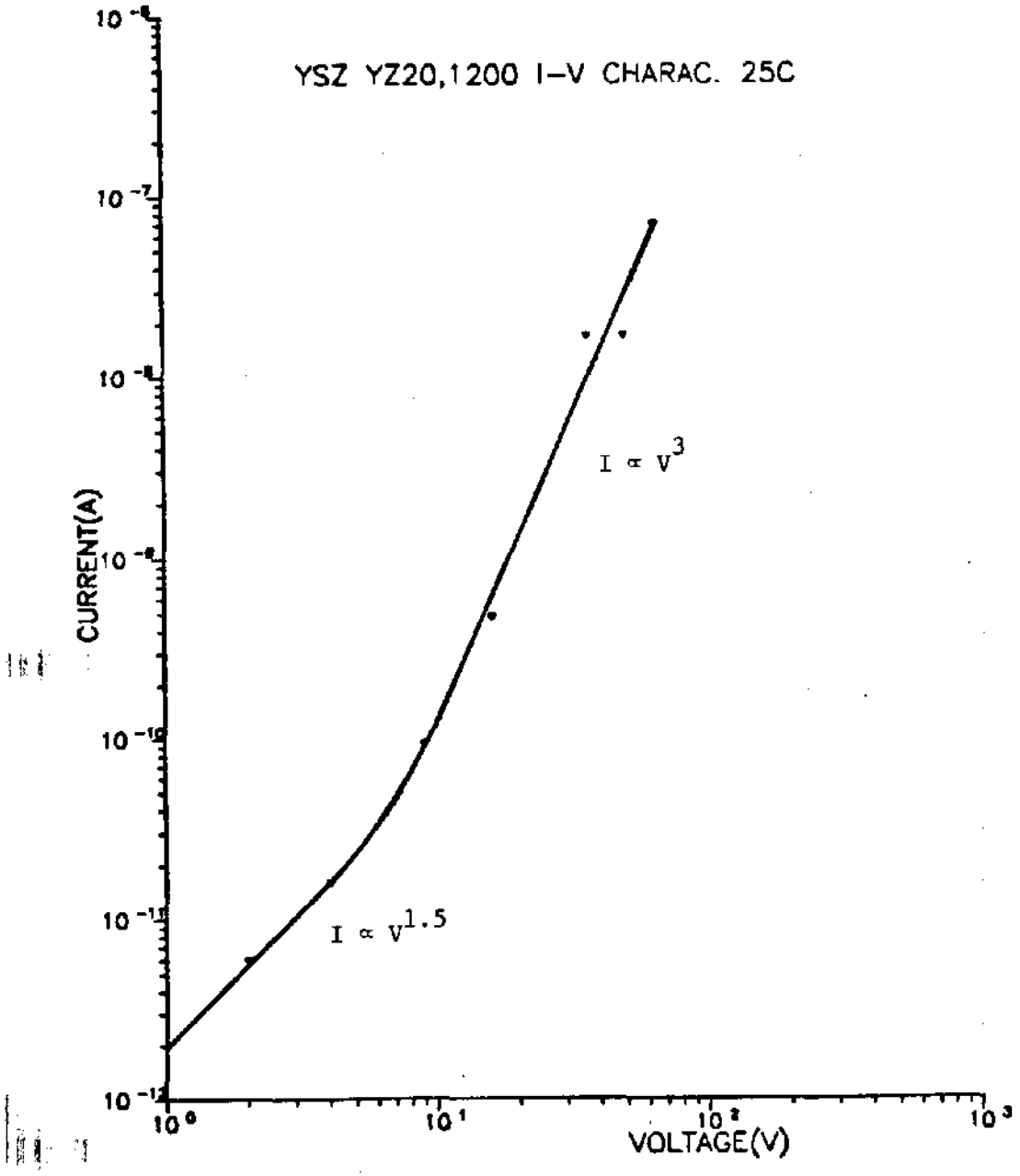


Fig. 60. I-V Characteristics of Au/Pd-Y_2O_3, ZrO_2- Pt/Rh Films at Room Temperature.

Whereas the molybdenum dot capacitors were unchanged in conduction characteristics. Hence, the sputtered electrode did indeed introduce new conduction characteristics on the ZrO_2 layers. The emf generated by the molybdenum dot and Au/Pd dot ZrO_2 capacitors were investigated and voltages were observed on the former at temperatures above 230 °C (e.g., 28 mV at 230 °C) but not on the latter, which supports the suggestion that the sputtering electrode introduced a predominantly electronic process in the Au/Pd dot Y_2O_3,ZrO_2 capacitors. The latter structures however, showed rather high emfs at temperatures above 200 °C (e.g., 112 mV at 360 °C), which may suggest that some ionic conduction may also be present in these Au/Rd-Y_2O_3,ZrO_2-Pt/Rh structures.

4.2.3 Impedance Spectroscopy

The admittance plot for the as-deposited Pt/Rh-Y_2O_3,ZrO_2-Pt/Rh sample is shown in Figure 61 having characteristics similar to all the ZrO_2 samples deposited at high temperatures with a bulk semicircle and a low semicircle depression. The heat treated Au/Rd-Y_2O_3,ZrO_2-Pt/Rh sample also shows a single bulk semicircle but with a large semicircle depression (Figure 62). This large semicircle depression indicates a large spread of relaxation times. The following are some effects that can produce such a spread of relaxation times: (1) The non-uniform diffusion of Y_2O_3 into the structure during heat treatment, thus, producing concentration gradients and inhomogeneity, (2) The mix of electronic, interstitial and vacancy ionic conduction proceses and (3) The effect of trapped moisture or other contaminants. More work would be required to determine the specific effects.

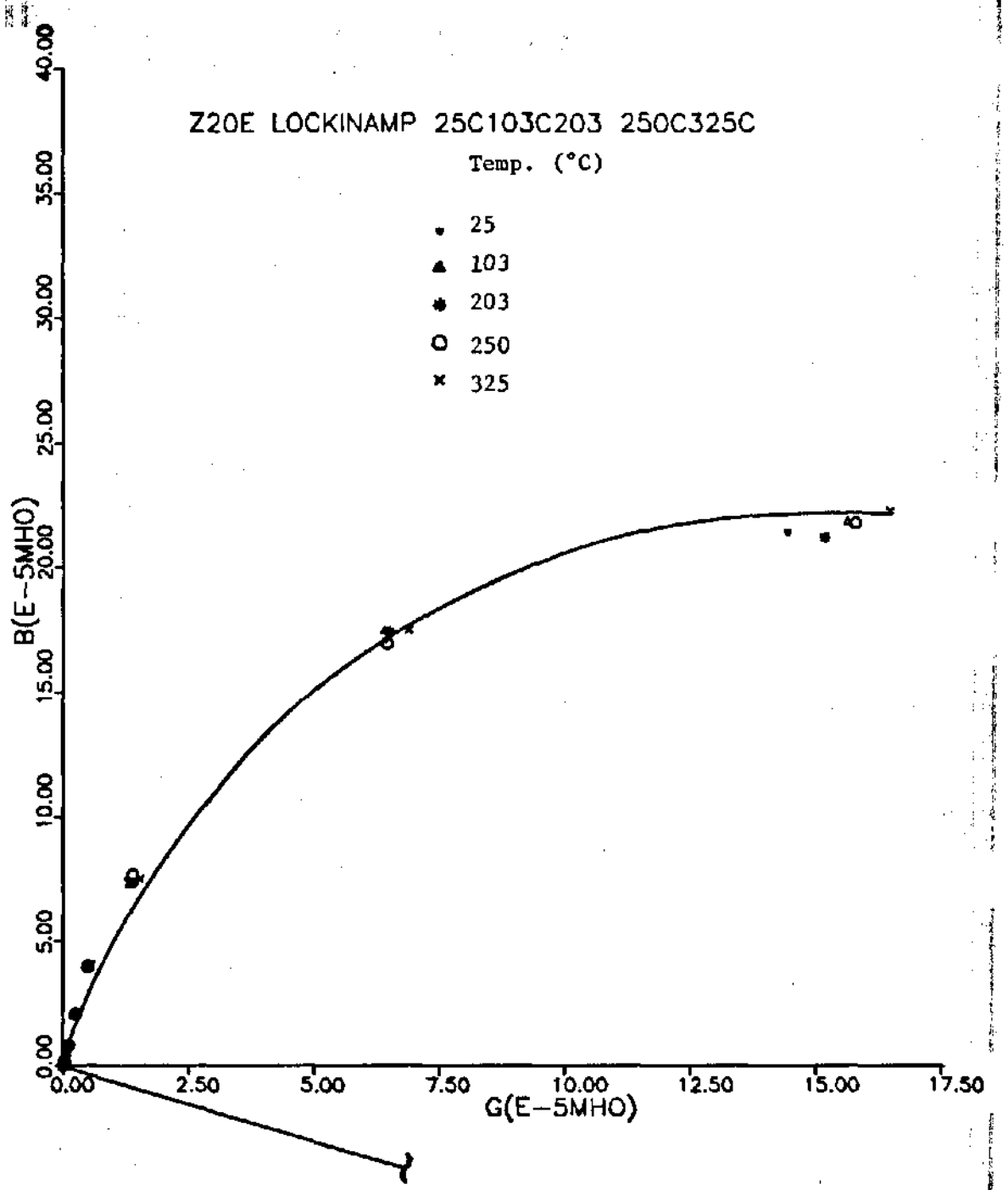


Fig. 61. Admittance Plots for Pt/Rh=Y_2O_3, ZrO_2-Pt/Rh Film, as Deposited for Varying Temperatures.

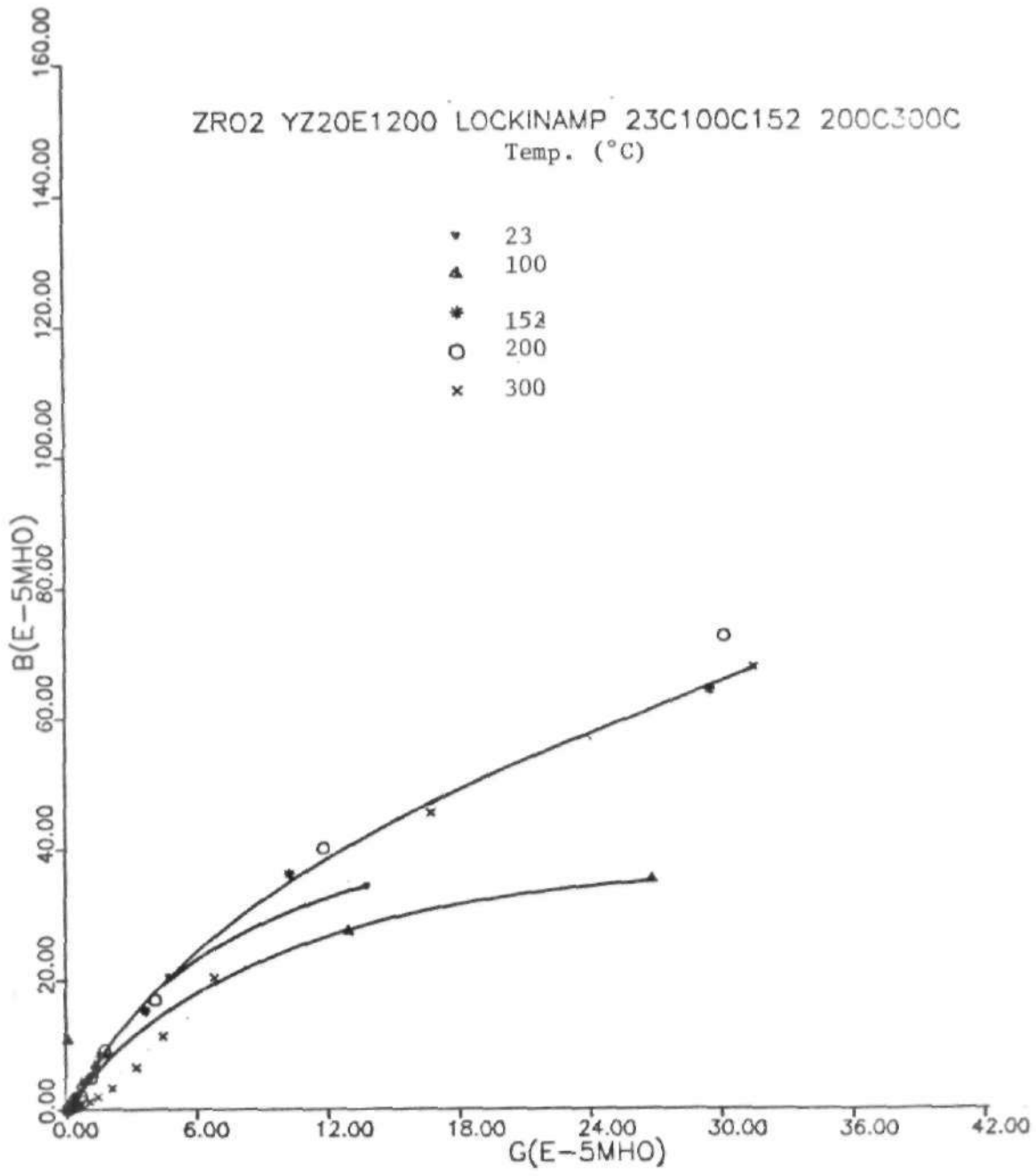


Fig. 62. Admittance Plots for Au/Pd-Y_2O_3, ZrO_2-Pt/Rh Films for Varying Temperatures.

CONCLUSIONS

Electron-beam deposition of ZrO_2 on molybdenum electrodes produced polycrystalline films. The monoclinic phase was the major phase detected in films deposited at temperatures between 300 °C and 600 °C. At lower deposition temperatures (190°-200 °C) however, the cubic phase was the major crystalline phase formed. The presence of amorphous material, especially in films deposited at the lower temperatures, was suspected but the amorphous content could not be quantified because of preferred orientation in the films.

Zirconia films deposited between 300 ° and 510 °C showed a double fiber texture, with the fiber axis approximately the $[11\bar{1}]$ and [111] directions. The fiber texture became more pronounced with increase in deposition temperature. For these films, average crystallite sizes increased from 118 to 484 Å for the $(11\bar{1})$ and 175 to 265 A for the (111) crystallites as deposition temperature increased from 200 ° to 600 °C. There was preferred crystallite growth in approximately the [111] direction.

Heating Mo-ZrO_2-Mo capacitors to 200 °C in vacuum prior to making electrical measurements reduced initially high permittivities and provided reproducible values for samples deposited above 350 °C. For ZrO_2 films deposited at lower temperatures, more extensive heat treatment was required to realise reproducibility. This was thought to be due to water adsorbed in films deposited at lower temperatures. Such adsorbed moisture might be limited to a shallow depth from the surface

or might be adsorbed in the entire bulk of the films. Moisture adsorbing porosity in the films could arise from poor film growth and/or poor adhesion of the electrodes, both of which become more prevalent at lower deposition temperatures.

Ac conduction in the Mo-ZrO_2-Mo structures at a low field of 0.05 MV/cm was dominated by electron hop at temperatures between 25°C and 150 C. A $\sigma_d \propto f^y$ dependence was observed where y was a temperature dependent parameter. At room temperature, a single dispersion region was obtained, with a y value of 1.0, which was independent of deposition temperature. This supported a single electron-hop mechanism. However, at 325°C, two dispersion regions were obtained, a low frequency region (60 -10 Hz) and a high frequency region (10 -10 Hz). The high frequency y values decreased from 0.8 to 0.63 whereas the low frequency values decreased from 0.6 to 0.31 as deposition temperature decreased from 450° to 300°C. High temperature behavior was attributed to an additional dissipation mechanism, such as interfacial polarization at the lower frequencies, and its remanance in the higher frequency region. Samples deposited at lower temperatures showed much greater interfacial polarization effects.

Admittance plots of Mo-ZrO_2-Mo samples deposited above 350°C showed a single semicircle with a low semicircle depression of 10 at temperatures between 25°and 325°C that was attributed to intragrain (bulk) conduction. However, the Mo-ZrO_2-Mo sample deposited at 300°C showed an anomalous low frequency effect which was probably due to adsorbed moisture.

The dc conduction behavior of Mo-ZrO_2-Mo samples were similar for

all deposition temperatures at fields below 0.25 MV/cm and at temperatures between 25° and 325°C. The conduction was ohmic and polarity independent, characterised by an activation energy decrease above 120°C and increase above 200°C. Activation energies were higher (0.6-1.0 eV) than those of ac conduction (0.05-0.4 eV). Effect of adsorbed moisture and a mix of electron hop and ionic conduction or a combination of all three were suggested as the possible mechanisms. A sample deposited at a high temperature of 450°C was ohmic up to breakdown but the one deposited at the low temperature of 300°C showed a space-charge-limited-currents (SCLC) effect at fields above 0.25 MV/cm and room temperature.

Charge storage by the Mo-ZrO_2-Mo samples increased linearly with voltage and increased with temperature. At any voltage and temperature, the sample deposited at 300°C had roughly double the charge storage of one deposited at 450°C. Charge storage was polarity independent at 25°C and 60°C but showed a polarity dependence at 90°C that was ascribed to the remanence of previous charging.

Cubic Y_2O_3 stabilized ZrO_2 films can be formed by multilayer depostion of Y_2O_3 and ZrO_2 on molybdenum electrode, followed by heat treatment in nitrogen at 1200°C for seven hours. Such multilayer deosition on Pt/Rh electrodes produced only a slight amount of a cubic or tetragonal phase, the exact structure of the phase could not be resolved, in the as-deposited form but also produced completely cubic and/or tetragonal phase on heat treating in air at 1200°C for nine hours. A more favorable epitaxial growth condition on the molybdenum might be responsible for the stronger development of the cubic structure

on it as compared to the Pt/Rh electrode.

Au/Pd-Y_2O_3,ZrO_2-Pt/Rh structures showed an SCLC behavior at 0.02 MV/cm and room temperature that is attributed to conduction by holes and/or effect of adsorbed moisture or other contaminants. The holes were suggested to be produced during the heat treatment in the oxygen-rich air by an interstitial mechanism and the moisture could have been trapped in the oxide layers before the sputtering of the Au/Pd electrode. However, the structures showed high emfs at temperatures above 200 °C (eg. 112 mV at 360 °C) which may suggest that some ionic conduction was also contributing.

The admittance plot of the Au/Pd-Y_2O_3,ZrO_2-Pt/Rd sample showed a large semicircle depression of about 45° that could be due to two possible effects: a mix of conduction processes, and structural inhomogeneity produced by non-uniform diffusion of Y_2O_3 into the structure.

RECOMMENDATIONS

Based on the results of this investigation, there are several recommendations for future work on electron-beam evaporated ZrO_2 and Y_2O_3,ZrO_2 multilayer films.

The uniformity of the conduction characteristics of the ZrO_2 films deposited above 400 °C in an oxygen atmosphere, probably due to their crystallinity, was remarkable and indicates that,though these films may be slightly less resistive than the alumina equivalents, they probably ought to be preferred in applications such as insulator layers for Low Voltage Field Emitter Arrays and other high field applications.

In the future, the bulk ZrO_2 oxygen ion electrolytes used for oxygen sensors, fuel cell, etc., will most likely be replaced by thin films of cubic stabilized ZrO_2, which provide several advantages over the bulk material. Methods for preparing such cubic ZrO_2 films need to be studied and perfected. Multilayer deposition used here is one of the evaporation alternatives in addition to co-evaporation. Both methods need to be studied in more detail to acertain their advantages and disadvantages. Such studies should include structural and electrical characterization of the as-deposited and heat treated films. The effect of epitaxy on the bottom electrode should also be investigated. It is further suggested that galvanic cells of the oxide multilayers be fabricated with a Ni-NiO standard oxygen partial pressure bottom electrode and a platinum paste electrode. This would provide needed information on ionic transference numbers for such materials.

Several features of the electrical conduction in the Mo-ZrO_2-Mo structures are yet to be resolved. The specific effect of adsorbed moisture and the extent of electron-hop and ionic conduction at high temperatures should be quantified. A study of the behavior of the activation energy decrease with repeated heating, combined with a study of the adsorbed species on the films would delineate the effect of moisture. As for the ionic and electronic conduction mix, the variation of conductivity with oxygen partial pressures should be studied to provide information on the defect chemistry of the films.

APPENDIX A

SYMBOLIC NOMENCLATURE AND PHYSICAL CONSTANTS

This section provides a summary of the symbolic nomenclature and physical constants used throughout this dissertation. The values of the physical constants are given in Table A-1, and the symbols and their meanings are listed in Table A-2.

Table A-1. Physical Constants.

Symbol	Definition	Value
e	Electron Charge	1.60210×10^{-19} coulomb
k	Boltzmann's Constant	1.30854×10^{-23} joule/K
ϵ_o	Permittivity of Free Space	8.84194×10^{-12} coul^2/N-m^2

Table A-2. Symbolic Nomenclature.

Symbol	Definition
A	Admittance
A_C	Area of a parallel plate capacitor
B	Susceptance
C	Capacitance
C_T	Total capacitance
C_e	Edge Capacitance
C_l	Lead capacitance
C_{lg}	Lead to ground capacitance
C_p	Parallel model capacitance
C_v	Vacuum capacitance
E	Activation energy
F	Field
F_i	Field at interface
f	Frequency
G	Conductance
I	Current
I_C	Capacitor current
I_F	XRD intensity of cubic ZrO_2 peak
I_R	Resistor current
I_T,	XRD intensity of tetragonal ZrO_2 peak
J	Current intensity

J_o	Pre-exponential factor
K_d	Constant
L	Separation of energy barriers
M_F	Moles of cubic ZrO_2
M_T'	Moles of tetragonal ZrC_2
M	Mass of a molecule
N_t	Trap density per unit volume and per unit energy
N	Constant
N_o	Equilibrium free carrier concentration
P_T	Total polarization
P_e	Electronic polarization
P_i	Ionic polarization
P_o	Orientational polarization
P_s	Space charge polarization
P_{sp}	Spontaneous polarization
P	Hydrostatic gas pressure
P*	Equilibrium vapor pressure
R_p	Parallel model capacitance
T	Absolute temperation
t	Thickness
V	Voltage
V_i	Sample supply voltage
V_C	Capacitor voltage
V_R	Resistor voltage
V_{ref}	Reference voltage

V_x	Real part of voltage
V_y	Imaginary part of voltage
X	Frequency dependence factor
Y	Temperature dependence parameter
Z	Impedance
Z_C	Capacitor impedance
Z_R	Resistor impedance
α	Parameter for Schottry effect
α_v	The ratio of evaporation rate in vacuum to the theoretically possible rate
β	Parameter for Poole-Frenkel effect
β'	Intrinsic broadening (°2θ)
γ	Parameter in exponential I-V characteristic
ε	Dielectric constant
ε'	Real part of dielectric constant
ε''	Imaginary part of dielectric constant
ε_s	Static dielectric constant
ε_∞	Infinite frequency dielectric constant
θ	Bragg angle (°2θ)
θ'	Ratio of free charge carries to free plus trapped charge
θ_d	Angle of depression
λ	X-ray wavelength
μ	Electron mobility
σ	Conductivity
σ_d	Dielectric conductivity
τ	Relaxation time

τ_a	Mean relaxation time
ϕ	Energy barrier
ϕ_m	Metal work function
ϕ_i	Insulator work function
Ψ	Richardon-Dushman constant ($\sim$120A Cm $Cm^{-20}K^{-2}$)
ω	Angular frequency (Radians S^{-2})

APPENDIX B

THIN FILM DEPOSITION PROGRAM

The thin film deposition programs used for preparing the molybdenum, zirconia, yttria and Pt/Rh films by E-beam evaporation are presented below.

Table B-1. Thin Film Deposition Programs

Material	Mo	ZrO_2	Pt/Rh	Y_2O_3
Setpoint				
Rise Time,min	8.0	15.0	8.0	15.0
Soak Time,min	2.0	3.0	2.0	3.0
Soak Power,%	54.0	55.0	54.0	55.0
Rate,A/sec	10	2.5	2.0	2.5
Fall Time,min	0.1	1.0	1.0	1.0
Idle Power,%	40	40	40	40
Maximun Power,%	80	75	66	65
Gain/Damping	7.3	9.1	7.3	9.1
Z Factor	0.257	0.493	0.239	2.69
Tooling Factor	184	92**	184	92
Density,gm/cc	10.2	5.6	21.45	5.03
Source/Xtal	1.1	1.1	1.1	1.1
Beam Position	3.75	Variable	3.75	Variable
Beam Sweep	Max	Min	Max	Min

** Reduction of Tooling Factor by 2 means that actual rate and thickness are twice the displayed values.

APPENDIX C

FORTRAN PROGRAM ACPROP

The FORTRAN computer code for ACPROP is provided below. The calculations performed by the program have been outlined in CHAPTER II and the linear regression procedure has been presented by Kolarik [67].

```
00100  PROGRAM AC(INPUT,OUTPUT,TAPE2,TAPE5=INPUT,TAPE6=OUTPUT)
C
C THIS PROGRAM CALCULATES, ANALYSES, AND PLOTS VARIOUS AC PROPERTIES FROM
C VALUES OF CAPACITANCE AND LOSS AS A FUNCTION OF FREQUENCY AND TEMPERAURE.
C TOTAL AND OPEN CIRCUIT CAPACITANCE AND LOSS TANGENT VALUES ARE INPUT
C IN TAPE2 ALONG WITH THE TEMPERATURES (IN   C) AND FREQUENCIES (HZ).
C THE PROGRAM PROVIDES THE FOLLOWING OPTIONS:
C (1) A LINEAR REGRESSION FOR DIEL. CONSTANT VS. FREQ. AND CONDUCTIVITY
C VS RECIPROCAL TEMP. AND VS. FREQ.
C (2) PRINT OUT OF SAMPLE CAPACITANCE, LOSS TANGENT REAL AND IMAGINARY
C PERMITTIVITIES AS A FUNCTION OF TEMPAERATURE AND FREQUENCY.
C (3) PLOTS OF
C REAL AND IMAGINARY PERMITTIVITY VS RECIPROCAL TEMPERATURE
C COLE-COLE PLOT
C REAL AND IMAGINARY DIELECTRIC CONSTANT VS RECIPROCAL TEMPERATURE
C DIELECTRIC CONDUCTIVITY VS RECIPROCAL TEMPERATURE AND FREQUENCY
C 1 KH DIELECTRIC CONDUCTIVITY VS RECIPROCAL TEMPERATURE
C
00110  DIMENSION IP(5),T(20),F(20),TC(20,20),TLT(20,20),OPENC(20),
00120 +OPENLT(20),ABST(20), C(20,20),ALT(20,20 ),
00130 +PREALI(20),PREAL(20,20),PREALD(20),PIMAGI(20),PIMAG(20,20),
00140 +PIMAGD(20),DC(20),DCRN(20),DCII(20),DCIN(20),ACCONN(20),
00150 +ACCON(20),IBUF(512),NSYMB(20)
00160  DATA(NSYMB(J),J=1,10)/21,2,11,17,4,5,10,19,3,20/
00170  READ (2,16) (IP(K),K=1,5)
00180  16 FORMAT(5A10)
00190  READ(2,*) M,(F(J),J=1,M),N,(T(I),I=1,N),((TC(I,J),J=1,M),I=1,N),
00200 +(OPENC(J),J=1,M),((TLT(I,J),J=1,M),I=1,N),(OPENLT(J),J=1,M)
00210 +,X,D,ADC
00220  CO=.06954*(D**2.)/(X*1.E-04)
00230  CE=3.1415*(D+X*1.E-04)*(ADC*.041-.077*ALOG10(X*1.E-04)+.045)
00240  CORCO=CE+CO
00250  CONST=8.854E-02/CORCO
00260  DO 17 I=1,N
00270  ABST(I)=1000./(T(I)+273.)
00280  17 CONTINUE
00290  DO 18 J=1,M
```

```
00300  DO 50  I=1,N
00310  C(I,J)=TC(I,J)-OPENC(J)
00320  ALT(I,J)=(TC(I,J)*TLT(I,J)-OPENC(J)*OPENLT(J))/C(I,J)
00330  PREAL(I,J)=CONST*C(I,J)
00340  PIMAG(I,J)=ALT(I,J)*PREAL(I,J)
00350  50 CONTINUE
00360  18 CONTINUE
 362 DO 900  I=1,N
 364 PIMAG1(I)=PIMAG(I,2)
 368 900 CONTINUE
00370  PRINT 227
00380  227 FORMAT(//1X,*DO YOU WANT LINEAR REGRESSION ANALYSIS?*//
00390 +*YES, TYPE 1, NO, TYPE 0*//)
00400  228 READ*,AND8
00410  IF(AND8.EQ.1)199,226
00420  199 PRINT 237,IP
00430  237 FORMAT(//1X,5A10//)
00440  PRINT 201
00450  201 FORMAT(1X,*FOR THE FOLLOWING PLOTS, IF YOU WANT REGRESSION*,
00460 +* ANALYSIS, TYPE 1, IF NOT, TYPE 0 AFTER QUESTION MARK*//
00470 +,*IF YOU TYPE 1, TYPE THE POSITION OF THE FIRST POINT AND THE # OF POINTS*
00480 +/* AFTER THE SECOND QUESTION MARK*,//*RESULTS ARE PRINTED OUT IN THE*,
00490 +* FOLLOWING ORDER*//*       SLOPE OR E(EV)              INTERCEPT
00500 +    *,*ST. ERROR           CORR. COEFF.*//)
00510  PRINT 202
00520  202 FORMAT(1X,*DIELECTRIC CONSTANT VS FREQ.-LOG-LOG.*//
00530 +*REAL AT LOWEST TEMP.*//)
00540  229 READ*,TEST
00550  IF(TEST.EQ.1)203,204
00560  203 CALL LINERG(F,PREAL,1,0)
00570  GO TO 229
00580  204 PRINT 206
00590  206 FORMAT(1X,*REAL AT HIGHEST TEMP.*//)
00600  230 READ*,TEST
00610  IF(TEST.EQ.1)207,208
00620  207 CALL LINERG(F,PREAL,N,0)
00630  GO TO 230
00640  208 PRINT 209
00650  209 FORMAT(1X,*IMAGINARY, AT LOWEST TEMP.*//)
00660  231 READ*,TEST
00670  IF(TEST.EQ.1)210,211
00680  210 CALL LINERG(F,PIMAG,1,0)
00690  GO TO 231
00700  211 PRINT 212
00710  212 FORMAT(1X,*IMAGINARY,AT HIGHEST TEMP.*//)
00720  234 READ*,TEST
00730  IF(TEST.EQ.1)213,214
00740  213 CALL LINERG(F,PIMAG,N,0)
00750  GO TO 234
00760  214 PRINT 215
00770  215 FORMAT(//1X,*AC COND. VS. FREQ., LOG-LOG*//
00780 +*LOWEST TEMP.*//)
```

```
00790  216 READ*,TEST
00800  IF(TEST.EQ.1)217,218
00810  217 CALL LINERG(F,PIMAG,1,1)
00820  GO TO 216
00830  218 PRINT 219
00840  219 FORMAT(//1X,*HIGHEST TEMP.*//)
00850  220 READ*,TEST
00860  IF(TEST.EQ.1)221,222
00870  221 CALL LINERG(F,PIMAG,N,1)
00880  GO TO 220
00890  222 PRINT 223
00900  223 FORMAT(//1X,*1KHZ AC COND. X TEMP. VS REC. TEMP.*//)
00910  224 READ*,TEST
00920CIF(TEST.EQ.1)225,226
00930  225 CALL LINERG(ABST,PIMAG,5,2)
00940  GO TO 224
00950  226 CALL PLOTS(IBUF,512,3,40)
00960  PRINT 100
00970  100 FORMAT(//1X,*TO HAVE THE FOLLOWING JOBS DONE FOR YOU,*,
00980+* TYPE 1, OTHERWISE, TYPE 0*)
00990  PRINT 102
01000  102 FORMAT(//1X,*CAPACITANCE, LOSS TAN. AND PERMITTIVITIES PRINT OUT*)
01010  READ*,AND1
01020  PRINT 104
01030  104 FORMAT(//1X,*REAL PERMITTIVITY-RECIPROCAL TEMP. PLOT*)
01040  READ*,AND2
01050  PRINT 106
01060  106 FORMAT(//1X,*IMAGINARY PERM.-RECIPROCAL TEMP. PLOT*)
01070  READ*,AND3
01080  PRINT 108
01090  108 FORMAT(//1X,*COLE-COLE PLOT*)
01100  READ*,AND4
01110  PRINT 110
01120  110 FORMAT(//1X,*REAL AND IMAGINARY DIELECTRIC CONST.-FREQ. *,
01130+* LOG-LOG PLOT*)
01140  READ*,AND5
01150  PRINT 112
01160  112 FORMAT(//1X,*AC CONDUCTIVITY-FREQ. LOG-LOG PLOT*)
01170  READ*,AND6
01180  PRINT 114
01190  114 FORMAT(//1X,*1KHZ AC COND.X TEMP.-RECIPROCAL TEMP. SEMI-LOG PLOT*)
01200  READ*,AND7
01210  IF(AND1.EQ.1)610,200
01220  610 PRINT 19
01230   19 FORMAT(///1X,*CAPACITANCE AND LOSS TANGENT AS A FUNCTION OF TEMP.
01240+AND FREQ. FOR*)
01250  PRINT 20,IP
01260  20 FORMAT(1X,5A10//)
01270  PRINT 21,(T(I),I=1,N)
01280  21 FORMAT(1X,*TEMP.(C)*,11F9.0)
01290  PRINT 22,(ABST(I),I=1,N)
01300  22 FORMAT(1X,*1000/T(K)*,11F9.3//)
```

```
01310 PRINT 23
01320 23 FORMAT(1X,*FREQ.(HZ)*,38X,*CAPACITANCE(PF)*/)
01330 PRINT 24,((F(J),(C(I,J),I=1,N)),J=1,M)
01340 24 FORMAT(1X,F8.0,1X,11F9.1/)
01350 PRINT 25
01360 25 FORMAT(//1X,*FREQ.(HZ)*,40X,*LOSS TANGENT*/)
01370 PRINT 26,((F(J),(ALT(I,J),I=1,N)),J=1,M)
01380 26 FORMAT(1X,F8.0,1X,11F9.4/)
01390 PRINT 27
01400 27 FORMAT(///1X,*REAL AND IMAGINARY PERMITTIVITY AS A FUNCTION *,
01410+*OF TEMP. AND FREQ FOR*)
01420 PRINT 20,IP
01430 PRINT 21,(T(I),I=1,N)
01440 PRINT 22,(ABST(I),I=1,N)
01450 PRINT 29
01460 29 FORMAT(1X,*FREQ.(HZ)*,32X,*REAL PERMITTIVITY(E-10F/M)*/)
01470 PRINT 26,((F(J),(PREAL(I,J),I=1,N)),J=1,M)
01480 PRINT 30
01490 30 FORMAT(//1X,*FREQ.(HZ)*,28X,*IMAGINARY PERMITTIVITY(E-10F/M)*/)
01500 PRINT 26,((F(J),(PIMAG(I,J),I=1,N)),J=1,M)
01510 200 CONTINUE
01520 PRINT 40,CORCO
01530 40 FORMAT(//1X,*CORRECTED VACUUM CAPACITANCE=*,F6.2,*PF*/)
01540 PRINT 31,CE
01550 31 FORMAT(1X,*VACUUM CAPACITANCE CORRECTION=*,F6.2,*PF*)
01560 IF(AND2.EQ.1)250,350
01570 250 CALL PLT(1.)
01580C
01590C REAL PERMITTIVITY-RECIPROCAL TEMP. PLOT
01600C
01610 CALL FACTOR(1.)
01620 CALL LIMIT(1.,1.,-3)
01630 PREAL1(N+1)=1.2
01640 PREAL1(N+2)=.2
01650 CALL SCALE (ABST,10.,N,1)
01660 CALL AXIS (0.,0., "REAL PERMITTIVITY(E-10F/M)",26,8.,90.,
01670+PREAL1(N+1),PREAL1(N+2))
01680 CALL AXIS(0.,0.,"1000/T(K)",-9,10.,0.,ABST(N+1),ABST(N+2))
01690 DO 500 J=1,M
01700 DO 510 I=1,N
01710 PREAL1(I)=PREAL(I,J)
01720 510 CONTINUE
01730 CALL LINE (ABST,PREAL1,N,1,1,NSYMB(J))
01740 CALL SYMBOL(4.,(6.5-.2*J),.1,NSYMB(J),0.,-1)
01750 CALL NUMBER(4.4,(6.5-.2*J),.1,F(J),0.,-1)
01760 500 CONTINUE
01770 CALL SYMBOL(4.4,6.6,.1,"FREQ.(HZ)",0.,9)
01780 CALL LMT(1.,8.5,IP)
01790 350 IF(AND3.EQ.1)360,450
01800 360 CALL PLT(1.)
01810C
01820C IMAGINARY PERMITTIVITY-REC. TEMP. PLOT
```

```
01830 C
01840  PIMAG1(N+1)=0.
01850  PIMAG1(N+2)=.2
01860  CALL SCALE(ABST,(50./7.),N,1)
01870  CALL AXIS(0.,0.,"IMAGINARY PERMITTIVITY(E-10F/M)",31,8.,90.,
01880 +PIMAG1(N+1),PIMAG1(N+2))
01890  CALL AXIS(0.,0.,"1000/T(K)",-9,(50./7.),0.,
01900 +ABST(N+1),ABST(N+2))
01910  DO 700 J=1,M
01920  DO 710 I=1,N
01930  PIMAG1(I)=PIMAG(I,J)
01940  710 CONTINUE
01950  CALL LINE(ABST,PIMAG1,N,1,1,NSYMB(J))
01960  CALL SYMBOL(4.,(4.5-.2*J),.1,NSYMB(J),0.,-1)
01970  CALL NUMBER(4.4,(4.5-.2*J),.1,F(J),0.,-1)
01980  700 CONTINUE
01990  CALL SYMBOL(4.4,4.7,.1,"FREQ.(HZ)",0.,9)
02000  CALL LMT(1.,8.5,IP)
02010 C
02020 CCOLE COLE PLOT
02030 C
02040  450 IF(AND4.EQ.1)460,550
02050  460 CALL PLT(1.)
02060  PIMAG1(N+1)=0.
02070  PREAL1(N+1)=.5
02080  PREAL1(N+2)=.2
02090  CALL AXIS(0.,0.,"IMAGINARY PERMITTIVITY(E-10F/M)",31,
02100 +8.,90.,PIMAG1(N+1),PIMAG1(N+2))
02110  CALL AXIS(0.,0.,"REAL PERMITTIVITY(E-10F/M)",-26,10.,
02120 +0.,PREAL1(N+1),PREAL1(N+2))
02130  DO 720 J=1,M
02140  DO 730 I=1,N
02150  PREAL1(I)=PREAL(I,J)
02160  PIMAG1(I)=PIMAG(I,J)
02170  730 CONTINUE
02180  CALL LINE(PREAL1,PIMAG1,N,1,-1,NSYMB(J))
02190  CALL SYMBOL(3.,(5.5-.2*J),.1,NSYMB(J),0.,-1)
02200  CALL NUMBER(3.4,(5.5-.2*J),.1,F(J),0.,-1)
02210  720 CONTINUE
02220  CALL SYMBOL(3.4,5.7,.1,"FREQ.(HZ)",0.,9)
02230  CALL LMT(1.,8.5,IP)
02240  550 IF(AND5.EQ.1)560,650
02250 C
02260 CPLOT REAL AND IMAGINARY DIEL. CONS. ON LOG-LOG. SCALE
02270 C
02280  560 CALL PLT(1.)
02290  CALL RESET2(DC,PREAL,1,M)
02300  CALL LGSCAL(F,5.,M,1)
02310  DC(M+1)=.1
02320  DC(M+2)=3./8.
02330  CALL LGAXIS(0.,0.,"DIELECTRIC CONSTANT",19,8.,90.,
02340 +DC(M+1),DC(M+2))
```

```
02350 CALL LGAXIS (0.,0.,"FREQ.(HZ)",-9,5.,0.,
02360+F(M+1),F(M+2))
02370 CALL LGLINE(F,DC,M,1,-1,2,0.)
02380 CALL RESET2(DC,PREAL,N,M)
02390 CALL LGLINE(F,DC,M,1,-1,5,0.)
02400 CALL RESET2(DC,PIMAG,1,M)
02410 CALL LGLINE(F,DC,M,1,-1,19,0.)
02420 CALL RESET2(DC,PIMAG,N,M)
02430 CALL LGLINE(F,DC,M,1,-1,17,0.)
02440 CALL LMT(1.,8.5,IP)
02450C
02460CPLOT AC CONDUCTIVITY VS FREQ.  LOG.-LOG.
02470C
02480 650 IF(AND6.EQ.1)660,800
02490 660 CALL RESET3(ACCON,PIMAG,1,M,F)
02500 CALL PLT(1.)
02510 CALL LGSCAL(ACCON,8.,M,1)
02520 CALL LGSCAL(F,5.,M,1)
02530 CALL LGAXIS(0.,0.,"AC CONDUCTIVITY(/#XM)",21,8.,90.,
02540+ACCON(M+1),ACCON(M+2))
02550 CALL LGAXIS(0.,0.,"FREQ.(HZ)",-9,5.,0.,
02560+F(M+1),F(M+2))
02570 CALL LGLINE(F,ACCON,M,1,-1,2,0.)
02580 CALL RESET3(ACCON,PIMAG,N,M,F)
02590 CALL LGLINE(F,ACCON,M,1,-1,5,0.)
02600 CALL LMT(1.,8.5,IP)
02610C
02620C1KHZ AC COND.*TEMP.-TEMP. PLOT SEMI-LOG
02630C
02640 800 IF(AND7.EQ.1)810,820
02650 810 CALL PLT(1.)
02660 DO 830 I=1,N
02670 ACCON(I)=6.28*F(5)*PIMAG(I,5)*1.E-10*1000./ABST(I)
02680 830 CONTINUE
02690 CALL LGSCAL(ACCON,8.,N,1)
02700 CALL SCALE(ABST,5.,N,1)
02710 CALL LGAXIS(0.,0.,"AC COND.*TEMP.(K/#XM)",21,8.,90.,
02720+ACCON(N+1),ACCON(N+2))
02730 CALL AXIS(0.,0.,"1000/T(K)",-9,5.,0.,
02740+ABST(N+1),ABST(N+2))
02750 CALL LGLINE(ABST,ACCON,N,1,-1,2,1)
02760 CALL LMT(1.,8.5,IP)
02770 820 CALL LIMIT(13.,0.,999)
02780 STOP
02790 END
02800C
02810CSUBROUTINES
02820C
02830 SUBROUTINE PLT(FAC)
02840 CALL FACTOR(FAC)
02850 CALL LIMIT(1.,0.,-3)
02860 RETURN
```

```
02870 END
02880C
02890 SUBROUTINE LMT(XX,YY,IP)
02900 DIMENSION IP(5)
02910 CALL SYMBOL(XX,YY,.14,IP,0.,50)
02920 CALL LIMIT(13.,0.,-3)
02930 RETURN
02940 END
02950C
02960 SUBROUTINE RESET1(Y1I,YIJ,N)
02970 DIMENSION Y1I(20),YIJ(20,20)
02980 DO 400 I=1,5
02990 Y1I(I)=YIJ(I,10)
03000 400 CONTINUE
03010 DO 402 I=6,N
03020 Y1I(I)=YIJ(I,1)
03030 402 CONTINUE
03040 RETURN
03050 END
03060C
03070 SUBROUTINE RESET2(DC,YIJ,I,M)
03080 DIMENSION DC(20),YIJ(20,20)
03090 DO 740 J=1,M
03100 DC(J)=YIJ(I,J)/.0885
03110 740 CONTINUE
03120 RETURN
03130 END
03140C
03150 SUBROUTINE RESET3(ACCON,YIJ,I,M,F)
03160 DIMENSION ACCON(20),YIJ(20,20),F(20)
03170 DO 750 J=1,M
03180 ACCON(J)=6.28*F(J)*YIJ(I,J)*1.E-10
03190 750 CONTINUE
03200 RETURN
03210 END
03220C
03230 SUBROUTINE LINERG(XARRAY,YARRAY,K,NTEST)
03240 DIMENSION XARRAY(20),YARRAY(20,20),DX(20),DY(20)
03250 READ*,IFIRST,NPOINT
03260 SUMX=0
03270 SUMY=0
03280 SUMXY=0
03290 SUMXS=0
03300 SUMYS=0
03310 ILAST=NPOINT+IFIRST-1
03320 IF(NTEST.EQ.0)301,302
03330 301 CONTINUE
03340 DO 303 I=IFIRST,ILAST
03350 DY(I)=ALOG(YARRAY(K,I)/.0885)
03360 303 DX(I)=ALOG(XARRAY(I))
03370 GO TO 308
03380 302 IF(NTEST.EQ.1)304,306
```

```
03390  304 CONTINUE
03400  DO 307 I=IFIRST,ILAST
03410  DY(I)=ALOG(YARRAY(K,I)*6.28E-10*XARRAY(I))
03420  307 DX(I)=ALOG(XARRAY(I))
03430  GO TO 308
03440  306 CONTINUE
03450  DO 305 I =IFIRST,ILAST
03460  DY(I)=ALOG(YARRAY(I,K)*6.28*1000.E-10*1000. /XARRAY(I))
03470  305 DX(I)=XARRAY(I)
03480  308 CONTINUE
03490  DO 309 I=IFIRST,ILAST
03500  SUMX=SUMX+DX(I)
03510  SUMY=SUMY+DY(I)
03520  SUMXY=SUMXY+DX(I)*DY(I)
03530  SUMXS=SUMXS+DX(I)**2.
03540  SUMYS=SUMYS+DY(I)**2.
03550  309 CONTINUE
03560  APOINT=NPOINT
03570  DENUM=SUMX**2.-APOINT*SUMXS
03580  TOP=SUMX*SUMY-APOINT*SUMXY
03590  SLOPE=TOP/DENUM
03600  CINTER=(SUMX*SUMXY-SUMXS*SUMY)/DENUM
03610  CCOEFF=-TOP/(((APOINT*SUMXS-SUMX**2.)*(APOINT*SUMYS-SUMY**2.))
03620 +**.5)
03630  SYX=((1./(APOINT-2))*(SUMYS-CINTER*SUMY-SLOPE*SUMXY))**.5
03640  IF(NTEST.EQ.2)315,314
03650  311 FORMAT(4F20.4)
03660  314 PRINT 311,SLOPE,CINTER,SYX,CCOEFF
03670  GO TO 316
03680  315 E=-SLOPE*.08614
03690  PRINT 311,E,CINTER,SYX,CCOEFF
03700  316 RETURN
03710  END
```

APPENDIX D

FORTRAN PROGRAM DC4

The computer code for FORTRAN program DC4 is listed below. The calculations performed by the program are outlined in CHAPTER II.

```
00100  PROGRAM DC(INPUT,OUTPUT,TAPE1,TAPE5=INPUT,TAPE6=OUTPUT)

C   THIS PROGRAM TREATS THE I = F(T) DATA BY READING AN INPUT DATA FILE
C CONTAINING, IN THE FIRST LINE, A SAMPLE DESCRIPTION. THE NUMBER OF
C VOLTAGES AND THE NUMBER OF TEMPERATURES APPEAR IN THE SECOND LINE.
C THE THIRD LINE CONTAINS THE SAMPLE THICKNESS IN MICRONS, DOT DIAMETER IN
C CM, AND THE APPROXIMATE DIELECTRIC CONSTANT. FINALLY, THE FOURTH LINE
C CONTAINS THE VOLTAGE. THE ACTUAL TEMPERATURE-CURRENT DATA THEN APPEARS
C IN A COLUMN OF TEMPERATURE (# F) AND CURRENT.
C     THE PROGRAM ALLOWS SELECTION OF POOLE-FRENKEL ANALYSIS OR ARRHENIUS
C OR CONDUCTIVITY X TEMPERATURE. THE PORTION OF THE LINE FOR ANALYSIS IS
C SELECTED. THE POOLE-FRENKEL ANALYSES OPTION OUTPUTS THE SLOPE, Y-INTERCEPT,
C STANDARD ERROR OF ESTIMATE, CORRELATION COEFFICIENT FOR THE REGRESSED
C LINE, AS WELL AS THE PHI, FIELD, C, AND BETA VALUES. THE ARRHENIUS AND
C CONDUCTIVITY X TEMPERATURE OUTPUT IS THE APPROXIMATE ACTIVATION ENERGY,
C Y-INTERCEPT, STANDARD ERROR OF ESTIMATE AND CORRELATION COEFFICIENTS
C OF THE SELECTED LINE. A PLOT OF THE SELECTED CONDUCTIVITY CAN THEN BE
C MADE USING THE CALCOMP PLOTTER.
C
00110  DIMENSION IP(5),V(4),T(50),TC(50),CURR(50,4),DCURR(50),
00120 +RABST(50),NSYMB(4),IFIRST(5,4),NPOINT(5,4),IBUF(512)
00130 +,CURRNA(50,4)
00140  COMMON TH,                DCONST,POOLE,AREA,D
00150  DATA (NSYMB(J),J=1,4)/2,3,11,17/
00160  READ(1,1) (IP(K),K=1,5)
00170  1 FORMAT(5A10)
00180  READ(1,*) M,N,TH,D,DCONST,(V(J),J=1,M),
00190 +((T(I),(CURRNA(I,J),J=1,M)),I=1,N)
00200  AREA=3.14*D**2./4.
00210  DO 3 J=1,M
00220  DO 4 I=1,N
00230  CURR(I,J)=CURRNA(I,J)*1.E-09
00240  4 CONTINUE
00250  3 CONTINUE
00260  DO 5 I=1,N
00270  TC(I)=(T(I)-32.)/1.8
```

```
00280  RABST(I)=1000./(TC(I)+273.)
00290  5 CONTINUE
00300  PRINT 10
00310  10 FORMAT(//1X,*REGRESSION ANALYSIS?, YES, TYPE 1; NO, TYPE 0*)
00320  READ*,AND
00330  IF (AND.EQ.1)15,20
00340  15 PRINT 21
00350  21 FORMAT(//1X,*POOLE FRENKEL? TYPE 1; COND.? TYPE 2*,
00360 +*;COND. X TEMP.?, TYPE 3*//)
00370  READ*,POOLE
00380  PRINT 25
00390  25 FORMAT(//1X,*FOR THE FOLLOWING PLOTS, TYPE DATA AS FOLLOWS*/
00400 +*# OF LINES, FIRST POINT, # OF POINTS, FIRST POINT, # OF POINTS *,
00410 +*ETC*///////)
00420  IF(POOLE.EQ.1)32,27
00430  27 IF (POOLE.EQ.2)28,29
00440  28 PRINT 17
00450  17 FORMAT(//1X,*ARRHENIUS-CONDUCTIVITY*//)
00460  GO TO 19
00470  29 PRINT 22
00480  22 FORMAT(//1X,*ARRHENIUS-COND. X TEMP.*//)
00490  19 PRINT 23,IP
00500  23 FORMAT(//1X,5A10///)
00510  PRINT 33
00520  33 FORMAT(//8X,*E(EV)*,12X,*INTERCEPT*,12X,*ST. ERROR*,
00530 +11X,*COR. COEF.*//)
00540  GO TO 34
00550  32 PRINT 43
00560  43 FORMAT(//1X,*POOLE FRENKEL ANALYSIS*//)
00570  PRINT 30,IP
00580  30 FORMAT(//1X,5A10///
00590 +*       SLOPE    INTERC   ST. ERROR  COR. CF.   PHI(V)  FIELD(MV/*
00600 +,*CM)  C(/ CM)          BETA*//)
00610  34 CONTINUE
00620  DO 35 J=1,M
00630  PRINT40,J
00640  40 FORMAT(//*PLOT NUMBER *,I1//)
00650  READ*,N1,((IFIRST(I,J),NPOINT(I,J)),I=1,N1)
00660  DO 45 I =1,N1
00670  CALL LINERG(RABST,CURR,IFIRST(I,J),NPOINT(I,J),J,V(J))
00680  45 CONTINUE
00690  35 CONTINUE
00700  20 PRINT 36
00710  36 FORMAT(//1X,*PLOT?, YES, TYPE 1; NO, TYPE 0*//)
00720  READ*, AND2
00730  IF(AND2.EQ.1)37,38
00740  37 PRINT 140
00750  140 FORMAT(1X,*ARRHENIUS PLOTS: COND., TYPE 2; COND. X TEMP.*,
00760 +*,TYPE 3*)
00770  READ*,TYPE
00780  CALL PLOTS(IBUF,512,3,40)
00790  CALL FACTOR(1.)
```

```
00800  CALL LIMIT(1.,0.,-3)
00810  CALL RESET(CURR,RABST,DCURR,TYPE,J,N,V(1))
00820  50 CONTINUE
00830  CALL LGSCAL(DCURR,8.,N,1)
00840  RABST(N+1)=1.2
00850  RABST(N+2)=.4
00860  XAXIS=6.
00870  IF(TYPE.EQ.2)160,170
00880  160 CONTINUE
00890  CALL LGAXIS(0.,0.,"CONDUCTIVITY(/#XM)",18,8.,90.,
00900 +DCURR(N+1),DCURR(N+2))
00910  GO TO 180
00920  170 CALL LGAXIS(0.,0.,"COND.*TEMP.(K/#XM)",18,8.,90.,
00930 +DCURR(N+1),DCURR(N+2))
00940  180 CONTINUE
00950  CALL AXIS(0.,0.,"1000/T(K)",-9,XAXIS,0.,
00960 +RABST(N+1),RABST(N+2))
00970  IF(M.EQ.1)120,100
00980  100 CONTINUE
00990  DO 55 J=1,M
01000  CALL RESET(CURR,RABST,DCURR,TYPE,J,N,V(J))
01010  CALL LGLINE(RABST,DCURR,N,1,-1,NSYMB(J),1)
01020  CALL SYMBOL(3.,(6.-.2*J),.1,NSYMB(J),0.,-1)
01030  55 CONTINUE
01040  GO TO 130
01050  120 CALL LGLINE(RABST,DCURR,N,1,-1,NSYMB(J),1)
01060  CALL SYMBOL(3.,(6.-.2*J),.1,NSYMB(J),0.,-1)
01070  130 CONTINUE
01080  CALL SYMBOL(1.,8.5,.14,IP,0.,50)
01090  CALL LIMIT(13.,0.,-3)
01100  CALL LIMIT(13.,0.,999)
01110  38 STOP
01120  END
01130C
01140  SUBROUTINE LINERG(XARRAY,YARRAY,IFIRST,NPOINT,J,V)
01150  DIMENSION XARRAY(50),YARRAY(50,4),DY(50),DX(50)
01160  COMMON TH,DCONST,POOLE,AREA,D
01170  ILAST=NPOINT+IFIRST-1
01180  SUMX=0.
01190  SUMY=0.
01200  SUMXY=0.
01210  SUMXS=0.
01220  SUMYS=0.
01230  IF(POOLE.EQ.2)52,53
01240  52 CONTINUE
01250  DO 67 I=IFIRST,ILAST
01260  DY(I)=ALOG(YARRAY(I,J)*TH*1.E-04/(AREA*V))
01270  67 CONTINUE
01280  GO TO 73
01290  53 CONTINUE
01300  DO 69 I=IFIRST,ILAST
01310  DY(I)=ALOG(YARRAY(I,J)*TH*1.E-01/(AREA*V*XARRAY(I)))
```

```
01320  69 CONTINUE
01330  73 CONTINUE
01340  DO 65 I=IFIRST,ILAST
01350  DX(I)=XARRAY(I)
01360  SUMX=SUMX+DX(I)
01370  SUMY=SUMY+DY(I)
01380  SUMXY=SUMXY+DX(I)*DY(I)
01390  SUMXS=SUMXS+DX(I)**2.
01400  SUMYS=SUMYS+DY(I)**2.
01410  65 CONTINUE
01420  APOINT=NPOINT
01430  DENUM=SUMX**2.-APOINT*SUMXS
01440  TOP=SUMX*SUMY-APOINT*SUMXY
01450  SLOPE=TOP/DENUM
01460  CINTER=(SUMX*SUMXY-SUMXS*SUMY)/DENUM
01470  CCOEFF =-TOP/(((APOINT*SUMXS-SUMX**2.)*(APOINT*SUMYS-SUMY**2.))
01480 +**.5)
01490  SYX=((1./(APOINT-2.))*(SUMYS-CINTER*SUMY-SLOPE*SUMXY))**.5
01500  IF(POOLE.EQ.1)85,80
01510  80 E=-SLOPE*.08614
01520  PRINT 90,E,CINTER,SYX,CCOEFF
01530  90 FORMAT(4F20.4)
01540  GO TO 95
01550  85 Q=1.602E-19
01560  BETA=SQRT(Q**3./(3.14*.0885E-16*TH*DCONST))
01570  FIELD=V/(TH*1.E-04)
01580  C=EXP(CINTER)/FIELD
01590  PHI=BETA*SQRT(V)/Q-.08614*SLOPE
01600  E=FIELD*1.E-06
01610  PRINT 70,IFIRST,NPOINT,SLOPE,CINTER,SYX,CCOEFF,PHI,E,C,BETA
01620  70 FORMAT(/1X,I1,*-*,I1,6F10.3,2E15.3)
01630  95 RETURN
01640  END
01650C
01660  SUBROUTINE RESET(CURR,RABST,COND,TYPE,J,N,V)
01670  DIMENSION CURR(50,4),RABST(50),COND(50)
01680  COMMON TH,AREA
01690  IF (TYPE.EQ.2)200,210
01700  200 CONTINUE
01710  DO 65 I=1,N
01720  COND(I)=100.*CURR(I,J)*TH*1.E-04/(AREA*V)
01730  65 CONTINUE
01740  GO TO 220
01750  210 CONTINUE
01760  DO 70 I=1,N
01770  COND(I)=100.*CURR(I,J)*TH*1.E-01/(AREA*V*RABST(I))
01780  70 CONTINUE
01790  220 RETURN
01800  END
```

APPENDIX E

FORTRAN PROGRAM ADMIT

The fortran computer code for ADMIT is listed below.

```
00100C  THIS PROGRAM CALCULATES THE REAL AND IMAGINARY PARTS
00110C OF THE ADMITTANCE OF A SAMPLE AND OUTPUTS THE RESULTS IN
00120C TAPE8. THE DATA ARE INPUT THROUGH TAPE7. THE PROGRAM
00130C WILL CALCULATE FOR UP TO 20 (M) SETS OF DATA, EACH WITH
00140C UP TO 20 (N) DIFFERENT FREQUENCIES.THE RAW LOCK-IN
00150C AMPLIFIER DATA ARE TO BE INPUT IN TAPE7 IN THE FOLLOWING
00160C MANNER.
00170C
00180C FIVE WORD TITLE
00190C M N
00200C FREQ(HZ) RESISTANCE(K OHMS) VX VY VRX VRY(MV)
00210C REPEAT N TIMES
00220C INPUT NEXT SET OF DATA M TIMES
00230C
00240C
00250  PROGRAM ADM(INPUT, OUTPUT,TAPE7,TAPE8,TAPE5=INPUT,TAPE6=OUTPUT)
00260  DIMENSION IP(5)
00270  DEG(X)=X*360./6.28
00280  READ(7,10) (IP(K),K=1,5)
00290  WRITE(8,10) (IP(K),K=1,5)
00300  10 FORMAT(5A10)
00310  READ(7,*) M,N
00320  INDEX=M*N
00330  DO 20 I=1,INDEX
00340  READ(7,*) FREQ,R,VX,VY,VRX,VRY
00350  R=R*1.E03
00360  VCX=VX-VRX
00370  VCY=VY-VRY
00380  VC=SQRT(VCX**2.+VCY**2.)
00390  VR=SQRT(VRX**2.+VRY**2.)
00400  A=VR/(VC*R)
00410  PHASE=DEG(ATAN(VRY/VRX))-DEG(ATAN(VCY/VCX))
00420  FACTOR=1.E05
00430  G=A*COSD(PHASE)*FACTOR
00440  B=A*SIND(PHASE)*FACTOR
00450  WRITE(8,*) FREQ,G,B
00460  20 CONTINUE
00470  WRITE(8,*) FACTOR
00480  STOP
00490  END
```

BIBLIOGRAPHY

1. R. J. Brook; PP. 272-285 in Advances in Ceramic, Vol. 3. Edited by A. H. Heuer and L. W. Hobbs, The American Ceramic Soc., Inc., Columbus, Ohio, 1981.

2. W. S. Chan and C. K. Loh,"Electrical Conduction of Zirconium Oxide Films",Thin Solid Films, (6) [2], 91-105)1970).

3. D. K. Dawson and R. H. Creamer,"The Electrical Conductivity of Zirconium Dioxide Films at Intermediate Temperatures", Brit. J. Appl. Phys., (16) 1643-47 (1965).

4. D. Husted, L. Gruss and T. Mackus,"Electrical Properties of Anodic Oxide Films of Tantalum, Niobium, Zirconium, Titanium, Tungsten and Vanadium Formed by the Ion-Cathode Method", J. Electrochem. Soc., (118) [12] 1989-92 (1971).

5. G. C. Wood and C. Pearson, "A.C. Resistivity of Anodic Oxide Films on Valve Metals," Nature 208 (5010), 547-9 (1965).

6. P. J. Harrop, and J. N. Wanklyn, "Dielectric Loss Spectra of Corrosion Films on Zirconium," J. Electrochem. Soc., (111) 1123-6 (1964).

7. R. D. Misch and F. H. Gunzel, Jr., "The Electrical Resistance of Oxide Films on Zirconium in Relation to Corrosion." J. Electrochem. Soc., (106) 15-20 (1958).

8. R. D. Misch, "Electrical Resistance Studies of Anodic and Corrosion Oxide Films Formed on Zirconium." U.S. At. Energy Comm. ANL-6259, 36 PP, (1961).

9. J. E. Greene, C. E. Wickersham, and J. L. Zilko, "Morphological and Electrical Properties of RF Sputtered Y203 Doped ZrO_2 Thin Films," J. Vac. Sci. Technol., (13) [1], (1976).

10. M.Croset, J. P. Schnell and G. Velasco, "Composition, Structure, and Ac Conductivity of Rf-Sputtered Calcia-Stabilized Zirconia Thin Films," J. App. Phys., 48 775-80 (1977).

11. R. N. Tauber, A.C. Dumbri and R. E. Caffrey, "Preparation of Properties of Pyrolytic Zirconium Dioxide Films," J. Electrochem. Soc. (118) [5] 747-54 (1971).

12. M. Balog, M. Schieber, M. Michman and S. Patai, "The Chemical Vapor Deposition and Characterization of ZrO_2 Films from Organometallic Compounds," Thin Solid Films, (47) [2] 109-20 (1977).

13. B. A. Mavchan, F. N. Tavadze, M. N. Okrosashvili, O. P. Shalamberidze and E. R. Kuteliya, "Study of Structures and Some Properties of ZrO_2 Condensates Produced by Electron-Beam Vaporization," Probl. Spets. Elektrometall. (9) 78-84 (1978) Russ.

14. G. S. Mikahailov, I. N. Akimovich and A. V. Stefanishina, "Formation of Thin Films of Oxide Electron Semiconductors by Vacuum Condensation with Heating of the Vaporizing Substance by Electron Bombardment", Simp. Protsessy Sin. Rosta Krist Plenok Poluprov. Mater., Tezisy Dokl., Novosibirk 22-5 (1965) Russ.

15. M. Croset, G. Velasco and J. P. Schnell, "Conductivity of Ion-Implanted Calcia-Stabilized Zirconia (C.S.Z.) Thin Films," Vide, Couches Minces, 201 746-9 (1980) (Suppl., Proc. Int. Vac. Congr., 8th V1).

16. D. H. Boone, S. S. Shen and J. W. Fairbanks, PP. 393-402 in Advanced Gas Turbine Coating for Minimally Processed Coal Derived Liquid Fuel. Pric. Conf. Adv. Mater. Alternative Fuel Capable Directly Fired Heat Engines, 1st (Conf-790749), Edited by J. W. Fairbanks and J. Stringer, NTIS: Springfield, Va., 1979.

17. J. A. Amick, "Deposition Techniques for Dielectric Films on Semiconductor Devices," J. Vac. Sci. Technol., (14) [5] 1053-63 (1977).

18. D. S. Campbell; PP. 5-1 to 5-26 in Handbook of Thin Film Technology, Edited by L. I. Maissel and R. Glang, Mcgraw-Hill Book Co., New York, 1970.

19. L. Maissel; PP. 4-1 to 4-44 in Handbook of Thin Film Technology, Edited by L. I. Maissel and R. Glang, McGraw-Hill Book Co., New York, 1970.

20. Z. M. Jarzebski, Oxide Semiconductors, 1st ed.; P. 46, Pergamon Press, New York, 1973.

21. R. Nahrowold, Ann. Physick, (31), 467 (1887).

22. D. S. Campbell; P. 5-23 in Handbook of Thin Film Technology, Edited by L. I. Maissel and R. Glang, McGraw-Hill Book Co., New York, 1970.

23. R. Glang, Ibid., PP. 1-3 to 1-30.

24. C. A. Neugebauer, Ibid., PP. 8-3 to 8-42.

25. C. A. Neugebauer, Ibid., P. 8-40.

26. D. Hoffman and D. Leibowitz, J. Val. Sci. Technol., (8) 326 (1972).

27. D. E. Meyer, Trans. Metall. Soc. AIME (245) 322 (1973).

28. F. L. Shuermeyer, W. R. Chase, and E. L. King, J. Appl. Phys. (42) 5856 (1976).

29. D. Epand and K. Liddane, Electronic Design (13) [6] 21 (1977).

30. J. C. Anderson, Dielectrics, P. 21. Reinhold Publishing Corporation, New York, 1964.

31. J. C. Anderson, Ibid., PP. 27-30.

32. J. L. Pentecost; PP. 345-87 in Radome Handbook. Edited by J. D. Walton, Engineering Experiment Station, Georgia Institute of Technology, Atlanta, 1966.

33. M. B. Stout, Basic Electrical Measurements, PP. 243-320. Prentice Hall Inc., Englewood Cliffs, NJ, 1950.

34. Ac Loss Characteristics and Dielectric Constant (Permittivity) of Solid Electrical Insulating Materials, ASTM Standard D 150-74.

35. W. D. Kingery, H. K. Bowen, and D. R. Uhlmann, Introduction to Ceramics, 2nd ed.; P. 918. John Wiley and Sons, New York, 1976.

36. L. H. VanViack, Material Science for Engineers, P. 249. Addison-Wesley Publishing Co., Reading, Massachusetts, 1970.

37. J. C. Anderson, Dielectrics, P. 67. Reinhold Publishing Corporation, New York, 1964.

38. K. S. Cole and R. H. Cole, J. Chem. Phys. (9) 341 (1941).

39. J. E. Baurle, "Study of Solid Electrolyte Polarization by a Complex Admittance Method," J. Phys. Chem. Solids (30) 2657-70 (1969).

40. N. M. Beekmans and L. Heyne, "Correlation Between Impedance Microstructure and Composition of Calcia-Stabilized Zirconia," Electrochimica Acta. (21) 303-10 (1975).

41. M. Kleitz, H. Bernard, E. Fernandez, and E. Schouler; PP. 310-336 in Advances in Ceramics, Vol. 3. Edited by A. H. Heueur and L. W. Hobbs, The American Ceramic Soc., Inc., Columbus, Ohio, 1981.

42. M. M. Narsrallah and D. L. Douglas, "Ionic and Electronic Conductivity in Y_2O_3-Doped Monoclinic ZrO_2," J. Electrochem. Soc. (121) [2] (1974).

43. M. A. Lampert, "Simplified Theory of Space-Charge-Limited Currents in an Insulator with Traps," Physical Review, (103) [6] 1648-56 (1956).

44. A. Rose, "Space-Charge-Limited Currents in Solids," Physical Review, (97) [6] 1538-44 (1955).

45. P. J. Harrop and D. S. Campbell; P. 1609 in Handbook of Thin Film Technology. Edited by L. I. Maissel and R. Glang, McGraw-Hill Book Co., New York, 1970.

46. C. A. Mead, "Electron Transport Mechanisms in Thin Insulating Films," Physical Review, (128) [5] 2088-93 (1962).

47. V. K. Gil'derman, V. I. Zemtsov, A. D. Neuimin, S. F. Pal'quev, D. S. Rutman, Yu. S. Toropov, and S. Yu Pliner, "Electrical Conductivity and Gas Permeability of Ceramic Coatings Produced by the Plasma Spraying of ZrO_2 Powder," Institute of Electrochemistry, Ural Science Center, Academy of Sciences of the USSR. Eastern Institute of Refractories. Translated from Ogneupory, [1], PP. 47-50, 1978.

48. A. Charlesby, "Ionic Currents in Thin Films of ZrO_2," Met. (1) 340-7 (1953).

49. D. A. Vermilyea, J. App. Phys. (3) [11] 3663-71 (1965).

50. T. W. Hickmott, J. App. Phys. 33, 2669-82 (1962).

51. A. I. Zudov and L. A. Zudova, Radiotekh. Elektron. (15) [6] 1327-8 (1970), Russ.

52. L. Young, Anodic Oxide Films, P. 262. Academic Press Inc., (1960).

53. P. J. Harrop and J. N. Wanklyn, Brit. J. App. Phys., (18) 739 (1967).

54. A. R. Morley, D. S. Campbell, and J. Anderson, J. Mats. Sci, (4) 259 (1969).

55. B. A. Mouchan, et. al., Chemical Abstracts 91: 26027t.

56. G. A. Muranova, and V. S. Terpugov, Izu Akad. Nauk USSR, Ser. Fiz., (45) [2] 392-5 (1981), Russ.

57. D. A. Vermilyea, J. Electrochem. Soc., (104) 427-33 (1957).

58. A. I. Zudov and L. A. Zudova, Izu. Vyssh. Ucheb. Zaved; Fiz. (10) [8] 15-19 (1967), Russ.

59. A. I. Zudov and L. A. Zudova, Ibid., (11) [12], 115-17 (1968), Russ.

60. A. Servini and A. K. Jonscher, Thin Solid Films, (3) 341 (1969).

61. L. A. Zudova and A. I. Zudov, and V. A. Sterkhov, Ibid., (18) [10] 155 (1975), Russ.

62. A. P. Belova, L. G. Gorskaya, and L. N. Zakgeim. Fiz. Tverd. Tela, (3) 1851-8 (1961).

63. V. A. Nicely and R. J. Davis, AEL Accession No. 23654, Rept. No. ORNL-TM-1435. (1965).

64. B. D. Cullity, Elements of X-ray Diffraction, 2nd ed.; P. 284, Addison-Wesley Publishing Co., Inc., Reading, 1976.

65. H. P. Klug and L. E. Alexander, X-ray Diffraction Procedures, P. 501. John Wiley and Sons, Inc., New York, 1954.

66. R. A. Miller, J. L. Smialek and R. G. Garlick, PP. 241-253 in Advances in Ceramics, Vol. 3. Edited by A. H. Heuer and L. W. Hobbs, The American Ceramic Society, Inc., Columbus, Ohio, 1981.

67. R. V. Kolarik II, "Electrical Properties of Amorphous Alumina Thin Films," Ph.D. Thesis, Georgia Institute of Technology, Atlanta, GA. 1981.

68. H. Birey, "Dielectric Properties of Aluminum Oxide Films," J. Appl. Phys. (49) [5] 2898-904 (1978).

69. F. Argall and A. K. Jonscher, "Dielectric Properties of Thin Films of Aluminum Oxide and Silicon Oxide," Thin Solid Films, (2) 185-210 1968.

70. W. D. Kingery, J. Pappis, M. E. Doty and D. C. Hill,"Oxygen Ion Mobility in Cubic ZrO_2. 85CaO. 1501. 85," J. Am. Ceram. Soc., (42) 393-8 (1959).

71. J. B. Peri and R. B. Hannon, J. Phys. Chem., (64) 1526 (1960).

72. K. M. Eisele, "Charge Storage and Storchiometry in Electron-Beam Evaporated Alumina, J. Electrochem. Soc., (122) [1] 148-52 (1975).

VITA

Paul Ben Onaji

August 4, 1951	Born in Owukpa, Benue State, Nigeria
1962-1963	Attended N. A. Primary School, Otobi, Nig.
1964-1968	Attended Govt. Sec. Sch., K/Ala, Nigeria
1969-1970	Attended Govt. High Sch., Keffi, Nigeria
June-Sept. 1973	Industrial training at Nig. Brewers Ltd. Kaduna
June 1974	B.Sc., (Hon) in Chemistry, A.B.U., Zaria, Nig.
1974-1975	National Youth Service Corps. Employed as Chemistry Teacher at St. Gregory's College, Obalende, Lagos, Nigeria.
August 1975	Joined the staff of Chemical Eng., Dept., A.B.Y., Zaria, Nigeria, as Graduate Assistant
November 1975	Left A.B.U., on Study Fellowship to T.H.T. Enshede, Holland
October 1976	Promoted to Assistant Lecturer
December 1977	B.Sc. and Ir. (M. Eng.) in Chemical Engineering Technological University of Twente, Enschede, Holland
1977-1979	Teaching and Research at A.B.U., Zaria, Nig.
October 1979	Promoted to Lecturer II (Assistant Professor)
1979-1982	Study Fellowship for a Ph.D. in Ceramic Eng., at the Georgia Institute of Technology, Atlanta Georgia, U.S.A. Employed as a Graduate Research and Teaching Assistant.
September 1982	Ph.D. in Ceramic Engineering at Georgia Institute of Technology, Atlanta, Georgia.

Publications and Presentations

1. "Solvents for Cellulose," B.Sc. Thesis, A.B.U., Zaria, Nigeria.

2. "An Investigation Towards A Model for the Carbon-Gas Reactions in an Agricultural and Forestry Waste Gasifier," Ir. Thesis, T.H.T., Holland.

3. P. B. Onaji, S. S. Adefila, and A. A. C. M. Beenackers, "Economic Feasibility of Gasification in Nigeria," Chemical Age of India, (31) [3] 194-197 (1980).

4. P. B. Onaji, S. S. Adefila and A. A. C. M. Beenackers; PP. 41-49 in Chemical Technology for Developing Countries. Edited by A. A. C. M. Beenackers, Nigerian Society of Chemical Engineers, Zaria, 1979.

5. P. B. Onaji and J. K. Cochran, "Structure and Ac Properties of Electron-Beam Evaporated ZrO_2 Thin Films," To Be Submitted for Publication to the Journal of American Ceramic Society.

6. P. B. Onaji and J. K. Cochran, "Dc Properties of Electron-Beam Evaporated ZrO_2 Thin Films." To be Submitted for Publication to the Journal of American Ceramic Society.

Fields of Study and Interest

Major: Ceramic Engineering and
Chemical Engineering

Minor: Electrical Engineering

Building and Structural Clay Products
Glass, Glazes and Enamels
Refractories
Electrical and Technical Ceramics
Energy Conversion
Process Control and Instruments